DIFFUSION OF POINT DEFECTS IN OXIDE-DISPERSION STRENGTHENED STEELS

MARKUS MOCK

Dissertation

19. Dezember 2018

DIFFUSION OF POINT DEFECTS IN OXIDE-DISPERSION STRENGTHENED STEELS

Zur Erlangung des akademischen Grades des Doktors der Naturwissenschaften (Dr. rer. nat.) genehmigte Dissertation vorgelegt von M.Sc. Markus Mock

Fachgebiet Materialmodellierung
Fachbereich Material- und Geowissenschaften
Technische Universität Darmstadt

Referent: Prof. Dr. Karsten Albe
Korreferent: Prof. Dr. Kai Nordlund
1. Prüfer: Prof. Dr. Martin Heilmaier
2. Prüfer: Prof. Dr. Karsten Durst

Tag der Einreichung: 19. Dezember 2018
Tag der Prüfung: 12. April 2019

Bitte zitieren Sie dieses Dokument als:
URN: urn:nbn:de:tuda-tuprints-88140
URL: https://tuprints.ulb.tu-darmstadt.de/id/eprint/8814

Dieses Dokument ist bereitgestellt von tuprint,
E-Publishing-Service der TU Darmstadt
http://tuprints.ulb.tu-darmstadt.de

ABSTRACT

Oxide-dispersion strengthened (ODS) steels are considered as promising materials for the next generation of fission reactors and future fusion reactors due to their outstanding combination of mechanical properties and resistance to radiation damage. The eponymous oxide precipitates are crucial for the properties of the material and the diffusion of yttrium is essential to their formation process.

In the first part of this thesis an interatomic potential for the iron-yttrium system is presented that enables large-scale atomistic simulations. The potential is used to investigate the interaction between substitutional yttrium atoms and edge dislocations and shows a significant attraction between yttrium atoms and the stress field of the dislocation. This leads to yttrium segregation and pinning of dislocation motion. Calculation of vacancy jumps within the core of edge dislocations reveals a significant reduction of migration barriers, which leads to the conclusion that pipe diffusion can be a relevant diffusion mechanism of yttrium in ODS steels.

The second part deals with the bulk diffusion of yttrium in bcc iron. Yttrium atoms and other oversized solutes show a high binding energy to vacancies and a considerable relaxation from their lattice site towards a neighboring vacancy. In the case of yttrium the relaxation is so prominent, that the resulting situation may also be considered as an interstitial atom sitting in between two vacancies. We calculate the yttrium-vacancy binding energy and the migration barriers of vacancy jumps in the vicinity of a yttrium atom by means of nudged-elastic band calculations using density functional theory (DFT) calculations. These barriers are used in a kinetic Monte Carlo code to calculate the diffusivity of yttrium and investigate the diffusion mechanism of yttrium in bcc iron with a focus on correlation effects.

The third part of this thesis deals with the impact of oxide precipitates on the radiation resistance of ODS steels. We address the question, if elastic strain fields around Y_2O_3 and $Y_2Ti_2O_7$ particles cause a long-ranged interaction between the precipitates and point defects. We use kinetic Monte Carlo simulations to simulate the diffusion of point defects in these strain fields and to determine the resulting steady state point defect concentrations. We show, that there is essentially no vacancy-strain interaction while the sink strength of precipitates for interstitials increases with misfit strain between precipitate and matrix. The total change of point defect concentration with misfit strain is, however, rather limited.

ZUSAMMENFASSUNG

ODS Stähle gelten aufgrund ihrer hervorragenden Kombination von mechanischen Eigenschaften und Beständigkeit gegen Strahlungsschäden als vielversprechende Werkstoffe für die nächste Generation von Atomreaktoren und zukünftigen Fusionsreaktoren. Die namensgebenden Oxidausscheidungen sind entscheidend für die Eigenschaften des Materials, und die Diffusion von Yttrium ist von entscheidender Wichtigkeit für die Ausscheidungsbildung.

Im ersten Teil dieser Arbeit wird ein interatomares Potential für das Eisen-Yttrium System vorgestellt, welches es ermöglicht, großskalige atomistische Simulationen durchzuführen. Das Potential wird verwendet, um die Wechselwirkung zwischen substitutionellen Yttriumatomen und Stufenversetzungen zu untersuchen und weist eine signifikante Anziehungskraft zwischen den Yttrium Atomen und dem Spannungsfeld der Versetzung nach. Dies führt zu einer Anreicherung von Yttrium an Versetzungen und behindert dadurch die Versetzungsbewegung. Die Simulation von Leerstellensprüngen innerhalb des Versetzungskerns von Stufenversetzungen zeigt eine signifikante Reduktion der Migrationsbarrieren, was zu dem Schluss führt, dass Pipediffusion ein relevanter Diffusionsmechanismus von Yttrium in ODS Stählen ist.

Der zweite Teil der Arbeit beschäftigt sich mit der Volumendiffusion von Yttrium in bcc Eisen. Yttrium und andere große Atome zeigen eine hohe Bindungsenergie an Leerstellen und eine deutliche Relaxation von ihrer Gitterposition hin zu einer benachbarten freien Stelle. Im Falle von Yttrium ist die Relaxation so stark ausgeprägt, dass die sich daraus ergebende Situation auch als ein Zwischengitteratom betrachtet werden kann, das in der Mitte zwischen zwei freien Gitterplätzen sitzt. Die Bindungsenergie zwischen Yttriumatomen und Leerstellen und die Migrationsbarrieren von Leerstellensprüngen in der Nähe eines Yttriumatoms wurde durch DFT-Rechnungen ermittelt. Diese Barrieren werden in einem kinetischen Monte-Carlo-Code verwendet, um die Diffusivität und den Diffusionsmechanismus von Yttrium in bcc-Eisen zu untersuchen.

Der dritte Teil dieser Arbeit beschäftigt sich mit dem Einfluss der Oxidausscheidungen auf die Strahlungsbeständigkeit von ODS Stählen. Dabei wird die Frage beantwortet, ob elastische Dehnungsfelder um die Y_2O_3 und $Y_2Ti_2O_7$ Partikel eine langreichweitige Wechselwirkung zwischen den Ausscheidungen und Punktdefek-

ten hervorrufen. Mit Hilfe von kinetischen Monte-Carlo Simulationen wurde die Diffusion von Punktdefekten in diesen Dehnungsfeldern simuliert und die resultierenden stationären Punktdefektkonzentrationen bestimmt. Dabei zeigt sich, dass es praktisch keine Wechselwirkung zwischen Leerstellen und Ausscheidungen gibt, während die Wirksamkeit der Ausscheidungen als Senken für Zwischengitteratome mit der Fehlanpassung zwischen Ausscheidung und Matrix ansteigt. Insgesamt ist der Einfluss der Dehnungsfelder auf die Punktdefektkonzentration jedoch eher begrenzt.

CONTENTS

GLOSSARY

SYMBOLS

a	lattice constant
c	lattice constant
m	mass
$\mathbf{r}$	position vector
t	time
δt	time interval
$\mathbf{F}$	Force vector
E	total energy
U	potential energy
E^{mig}	migration barrier
E^{b}	binding energy
E^{c}	cohesive energy
B	bulk modulus

ACRONYMS

MD	molecular dynamics
DFT	density functional theory
KMC	Kinetic Monte Carlo
bcc	body-centered cubic
fcc	face-centered cubic
hcp	hexagonal close-packed
MSD	mean-squared displacement
ODS	oxide-dispersion strengthened
MA	mechanical alloying
APT	atom probe tomography
TEM	transmission electron microscopy

XRD	X-ray diffraction
SANS	small-angle neutron scattering
XPS	X-ray photoelectron spectra
ITER	international thermonulear experimental reactor
RAFM	reduced activation ferritic martensitic
SIA	self-interstitial atom
dpa	displacements per atom
ABOP	atomic bond-order potential
EAM	embedded-atom method
MEAM	modified embedded-atom method
VASP	Vienna Ab initio Simulation Package
LAMMPS	Large-scale Atomic/Molecular Massively Parallel Simulator
DISC	Diffusion Simulation Code
FEM	finite element method
CI-NEB	climbing-image nudged elastic band
DOF	degree of freedom

Part I

INTRODUCTION AND METHODOLOGY

1 MOTIVATION AND EXISTING KNOWLEDGE

1.1 FUSION POWER

The globally growing energy consumption and the rising thread of global warming requires new solutions to satisfy the energy demands of the future. One part of a fossil-fuel free power mixture could be fusion energy.[1] Currently, the international thermonulear experimental reactor (ITER) is under construction in Saint-Paul-lès-Durance (France). It is the worlds largest magnetic confinement plasma physics experiment and will lead the way to a peaceful usage of fusion energy. Thirty-five nations contribute to this cooperative scientific megaproject. One of the problems that needs to be solved in order to step from starting a fusion reaction to safe, efficient and reliable production of electric energy is finding materials that can endure the hostile conditions close to the plasma for an extended time. In a fusion reaction two lighter atomic nuclei fuse to form a heavier nucleus. In ITER and its proposed successor DEMO, the fusion reaction between deuterium and tritium to helium will generated the energy as shown in Figure 1.1. The majority of the resulting energy is freed in form of the kinetic energy of a neutron.

Neutrons are not affected by the magnetic field containing the plasma and will hit the walls of the plasma chamber, displacing lattice atoms and converting their kinetic energy into thermal energy. New high-performance structural materials are

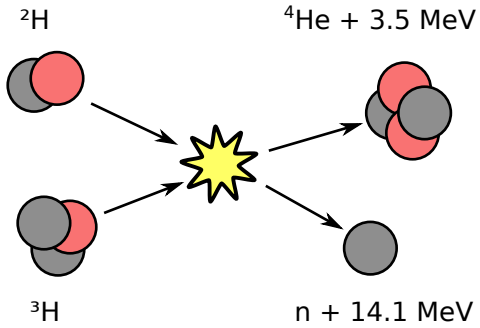

Figure 1.1: Fusion of deuterium and tritium creates helium and a neutron. The neutron carries the majority of the resulting energy in the form of kinetic energy.

necessary to withstand the harsh conditions in a fusion reactor. The constant bombardment with high energy neutrons causes microstructural changes and forms high concentrations of interstitials and vacancies. Absorption of neutrons can turn the structural materials radioactive in a process called neutron activation. The following radioactive decay often releases α-radiation which introduces helium into the material.[2] Management of the He accumulation is an additional important challenge.[3]

A review by Zinkle *et al.*[4] summarizes the conditions materials need to endure in a fusion reactor and outlines fundamental options to design radiation resistant materials. They conclude that reduced activation ferritic martensitic (RAFM) (potentially oxide-dispersion strengthened) and silicon carbide ceramic composites are promising candidates for structural materials. Stork *et al.*[5] also analyzed the technological readiness of structural, plasma facing and high heat flux materials for future fusion reactors and defined a set of already applicable baseline materials. These include RAFM steels for blanket structural applications, tungsten for plasma-facing components and tungsten and copper alloys for high-heat flux materials. An additional set of materials has been identified where additional development is necessary, but which promise even better performance. These materials include ODS steels for the structure and composite tungsten and copper materials for the plasma-facing and high-heat flux materials. The present work focuses on ODS steels, which are introduced in the following section.

1.2 OXIDE-DISPERSION STRENGTHENED STEELS

RAFM are a primary candidate for serving as structural materials in fusion power plants due to their resistance to high neutron doses. The utilization of RAFM steels is, however, limited to around 600 °C due to their inferior tensile and creep strength at elevated temperatures. To achieve higher plant operation temperature, the high-temperature properties can be improved by adding thermally stable oxide particle dispersions. The resulting ODS steels are the most promising class of materials for high-temperature resistant structural materials in a severe neutron exposure environment.[6] Reviews on the development status of ODS steels can be found in the works of Lindau *et al.*[7] and Klueh *et al.*.[8]

1.2.1 *Processing of ODS steels*

ODS steels are typically produced by high energy ball milling of gas atomized Fe-Cr-Ti-W powders together with small amounts of Y_2O_3 powder.[9,10] Figure 1.2 shows a schematic of the ODS precessing steps. The state of the yttria particles after ball milling is disputed. Zhao *et al.*[11] observed only changes in the morphology of the nanoparticles during mechanical alloying (MA), but no complete dissolution. Dai *et al.*[12] also observed fracturing and reduction of yttria particle size, but X-ray photoelectron spectra (XPS) measurements lead them to the conclusion, that no dissolution of yttrium and oxygen atoms in the matrix occurs. On the other hand Couvrat *et al.*[13] observed no nano-clusters after MA but rapid nucleation during the pre-heating step before extrusion. Laurent-Brocq *et al.*[14] showed that MA leads to the formation of an oversaturated solid solution, followed by nucleation of precipitates. The same result has been recorded by Ailinger *et al.*[15,16] in their X-ray diffraction (XRD) and small-angle neutron scattering (SANS) investigation of the as milled powder. They concluded that the thermally insoluble yttrium atoms and oxygen dissolve in the alloy particles due to MA. The final result depends on various parameters like the milling conditions, but the general consensus is that yttrium, titanium and oxygen atoms dissolve in the matrix during MA.[9,10,14]

The milled powders are canned, degassed and consolidated by hot extrusion or hot isostatic pressing. Yttrium, titanium and oxygen precipitate during hot consolidation and form oxide precipitates. Additional recrystallization and cold- or warm-working heat treatments are used to shape the final products. Typical compositions are 0.2 to 0.5 wt % Y_2O_3, 0.2 to 1.0 wt % Ti and 1 to 3 wt % W. Resistance to corrosion is improved by adding Cr while W introduces solid solution strengthening.[3]

The resulting microstructure exhibits high dislocation densities from 0.5×10^{15} to $2 \times 10^{15}\,\mathrm{m}^{-2}$.[17] The grain size distribution is typically bimodal with small submicron sized grains and few large grains with sizes of more than 10 µm. The abnormal grain growth of some grains is not related to the distribution of precipitates, but is caused by differences in dislocation densities in the milled powders.[18,19] Extruded samples typically show a $\langle 110 \rangle$-fibre texture with grain aspect ratios of 2 to 10.[17,20,21] This leads to inferior properties like creep strength, ductility or fracture toughness in some orientations. Specifically designed thermomechanical treatment sequences are necessary to produce products with more isotropic microstructures.[3]

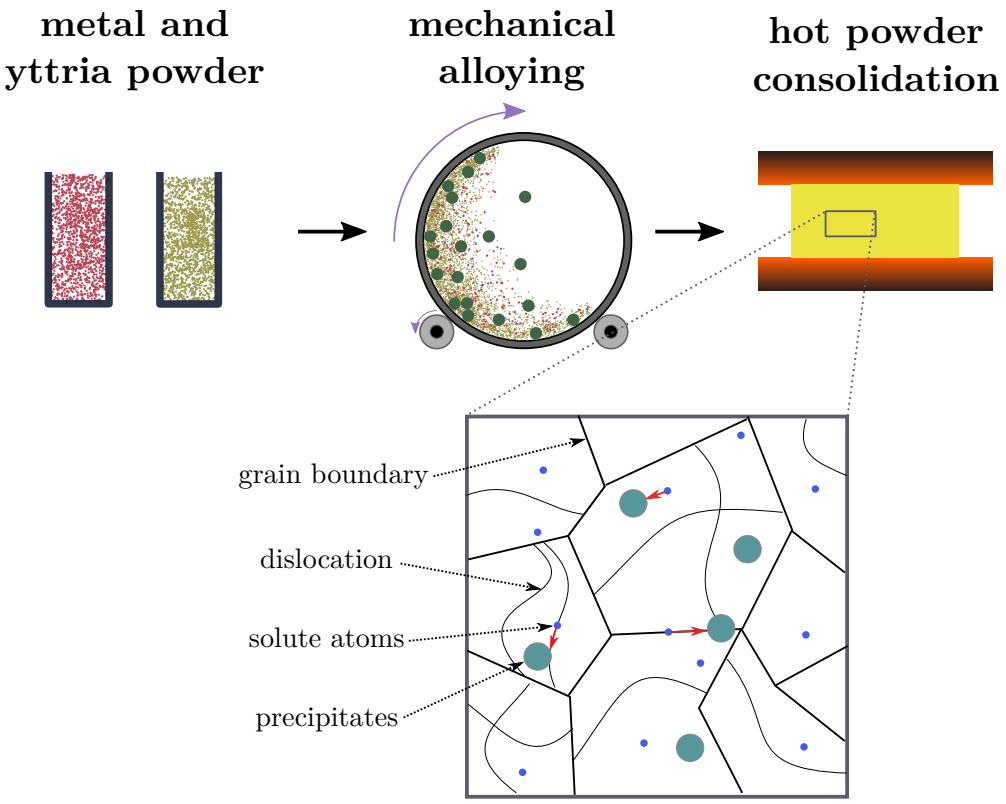

Figure 1.2: Schematic of the processing sequence for ODS steels. The mixture of alloy and yttria powder is processed by MA which crushes the Y_2O_3 and (partially) dissolves it in the alloy particles. During heat treatment the oxide precipitates are formed.

1.2.2 *Oxide precipitates*

The structure and composition of the oxide precipitates has been a disputed point for some time and depends significantly on the powder composition. Klimiankou *et al.*[22,23] have produced ODS steels by MA and hot isostatic pressing. Transmission electron microscopy (TEM) investigation have shown that the resulting precipitates consist of Y_2O_3 with an $[110]_{Ox}||[111]_{Fe}$ and $(1\bar{1}\bar{1})_{Ox}||(1\bar{1}0)_{Fe}$ orientation relationship with the Fe matrix. Ukai *et al.*[24] recognized that the addition of Ti significantly improves the high temperature strength by forming uniformly distributed ultrafine oxide particles. As a result a large part of experimental studies deals with ODS steels containing Ti.

Initial atom probe tomography (APT) measurements of these steels showed high Ti/Y ratios, low O/(Ti + Y) ratios and enrichment of Fe in the precipitates.[25] In the meantime it is accepted that these results were affected by APT artifacts and the Y/Ti ratio is a lot closer to unity.[26] TEM investigations by Hirata *et al.*[27,28] identified the crystal structure as a defective NaCl structure, while Brandes *et al.*[29] concluded that the precipitates are amorphous. The majority of TEM and XRD studies, however, have found precipitates in the cubic $Y_2Ti_2O_7$ structure.[23,28,30–36] Larger precipitates may also crystallize in the Y_2TiO_5 structure.[31,36]

The orientation relationship between matrix and $Y_2Ti_2O_7$ precipitates is of considerable interest as it affects the interaction with point defects, helium and dislocations. It is most frequently found to be a cube-on-cube $\{100\}_{Ox}||\{100\}_{Fe}$, $\langle 110\rangle_{Ox}||\langle 110\rangle_{Fe}$ or a cube-on-edge $\{110\}_{Ox}||\{100\}_{Fe}$, $\langle 110\rangle_{Ox}||\langle 110\rangle_{Fe}$ relationship.[31,33–35] Ribis *et al.*[34] also investigated the shape of the precipitates and the coherency with the matrix by analyzing Moiré fringes. They determined that small precipitates are spherical and coherent with the matrix and become more cuboidal and incoherent with increasing size.

1.2.3 *Precipitate formation*

Understanding the formation process of oxide precipitates is crucial for the optimization of ODS steels and is the focus of various studies which approach the problem from different directions. *Ab initio* calculations were used to investigate the initial stages of cluster formation.[37–43] Barnard *et al.*[38] calculated cluster formation energies of Y-Ti-O clusters with cations restricted to the Fe lattice sites as well as with structures matched to known stable oxide structures. They concluded that clusters that resemble the stable oxide structures are more stable, which is in

agreement to the experimental observation that precipitates are formed as Y_2O_3 or $Y_2Ti_2O_7$. Claisse *et al.*[39] calculated binding energies of clusters of yttrium, titanium, oxygen and vacancies. They observed that the slight repulsion between Y and Ti atoms can be overcome by the addition of O or vacancies in order to form clusters. Y solutes and vacancies form a particularly strong bond that might be connected to a low diffusivity of yttrium.

Posselt *et al.*[37] used DFT to determine interaction parameters in clusters of Y, Ti, O, Cr atoms and vacancies for use in Kinetic Monte Carlo (KMC) calculations. Clusters without vacancies showed a planar structure while the presence of vacancies lead to three-dimensional configurations. In the absence of Ti these 3D nanoclusters showed a Cr shell which has also been observed experimentally. Hin *et al.*[44] investigated the formation of Y_2O_3 precipitates using a KMC model. The model was based on DFT calculated and experimental parameters. They observed an initial formation of Fe_2O_3 followed by the nucleation of Y_2O_3 in the Fe_2O_3 particles.

The early stages of the nucleation were also investigated experimentally. He *et al.*[45] used slow positron beam Doppler-broadening measurements to investigate the interaction between Y and vacancies. They observed the formation of vacancy clusters, which could be explained by Y-V complexes or by precipitate formation. Couvrat *et al*[13] report a rapid nucleation of dissolved yttrium, titanium and oxygen to oxide precipitates during the pre-heating step before extrusion. Ailinger *et al.*[15,16] also reported a rapid precipitation at temperatures between 850 to 1150 °C with decreasing numbers and increasing precipitate size at higher temperatures. Ratti *et al.*[46] and Ukai *et al.*[6] investigated the influence of titanium on the precipitate formation and showed that titanium leads to a fine distribution of smaller precipitates. Sakasegawa *et al.*[47] also investigated the precipitate formation in the presence of titanium. They saw an initial formation of non-stoichiometric precipitates that became stoichiometric with increasing size. They also identified the diffusion of yttrium as crucial for the evolution of the precipitates.

The nucleation and growth of precipitates has also been tackled using classical nucleation-growth-coarsening models. Hin *et al.*[48] fitted their model to experimental SANS results of Y_2O_3 precipitate size distributions in a mechanically alloyed and consolidated Fe-Cr-Y-O ferritic alloy. Control of the temperature profile allowed an influence on the size and distribution of the precipitates. Key parameters are the solubility and diffusion coefficient of yttrium. Boulnat *et al.*[18,19] also applied a thermomechanical nucleation, growth and coarsening model to experimental results. They observed a rapid nucleation of both, Y_2O_3 and $Y_2Ti_2O_7$, during the heating stage followed by limited growth and coarsening during further annealing at higher

temperature. A crucial parameter for their model is the coefficient of yttrium diffusion as Y is the slowest diffusing constituent of the precipitates. Cunningham *et al.*[49] derived a coarsening model from previously reported long-time and high-temperature aging data. They found out that the best fit to the experimental data occurs when pipe diffusion of yttrium is taken into account. Due to the low solubility and slow diffusion of Y the precipitates remain stable up to 900 °C. Barnard *et al.*[50] created a semi-empirical model for the oxide precipitation using DFT as well as experimental results as input parameters. They predict little coarsening of the precipitates over timescales of 50 to 80 years at operation temperatures. According to their model the refining benefit of Ti additions is caused by the increased probability and driving force for nucleation of Y-Ti oxides over Y_2O_3. Pipe diffusion of yttrium atoms is also important for an accurate fit of the model to experimental results.

1.2.4 *Yttrium diffusion*

As the review of the modelling results in the previous section has shown, the diffusion of yttrium is a crucial process for the formation and growth of the oxide precipitates. Due to the lack of experimental values, the diffusivity was treated as a fit parameter by Hin *et al.* and Boulnat *et al.*, which lead to a very low diffusivity. Murali *et al.*[51] used DFT to calculate migration barriers and Le Claire's nine frequency model to determine the effective diffusivity from these barriers. The resulting diffusion coefficient at 1000 K is three orders of magnitude higher than the value obtained by Hin *et al.*.[48] Gao *et al.*[52] did a similar study but included the dependency of the activation energy of diffusion on the magnetization in the ferromagnetic state. They also investigated the attraction between substitutional yttrium atoms and vacancies and concluded that the high binding energy is mainly caused by the distortion of the lattice due to the size of yttrium atoms.

Bocquet *et al.*[53] also used DFT to calculate the migration barriers for yttrium diffusion, but derived a new model that is supposed to incorporate correlation effects better. This was considered necessary, as there is a very high binding energy between Y atoms and vacancies which significantly affects the different vacancy jumps in the vicinity of the yttrium atom. The attraction between vacancy and yttrium atom not only causes a high binding energy but also a relaxation of the yttrium atom towards the vacancy. Figure 1.3 shows this relaxation. For the nearest-neighbor configuration of yttrium and a vacancy the relaxation is so significant, that the yttrium atom could also be viewed as occupying an interstitial position

between two lattice sites. All three investigations are based on calculated migration barriers and lead to a diffusion coefficient far higher than the values determined from nucleation, growth and coarsening models.

1.2.5 *Irradiation*

The application of ODS steels in fusion reactors depends on their resistance to neutron radiation caused by the fusion reactions. Neutron radiation damage can be separated into two main damage types:

1. Displacement of lattice atoms in collision cascades
2. Transmutation reactions caused by neutron activation of atoms

The following sections explain these damage types and present the research connected to them. Access to neutron sources is generally limited. Therefore many research groups simulated fusion-reactor conditions using different types of heavy-ion radiation.

1.2.5.1 *Displacement damage*

High energy neutrons induce cascades of recoiling atoms that are displaced from their lattice sites. This creates a high local concentration of self-interstitial atoms (SIAs) and vacancies.[2] Many of these primary defects recombine, but some undergo long-range diffusion and cause microstructural changes. These may include the formation of voids and dislocation loops, dislocation climb and overall changes to the dislocation structure, radiation enhanced diffusion, radiation enhanced or induced precipitation or radiation induced solute segregation. The number and production rate of primary defects depends on the neutron flux and energy as well as the irradiation time and the irradiation temperature.[3]

Radiation damage is measured in displacements per atom (dpa), measuring how often each atom is moved away from its lattice site. Materials in a fusion reactor need to withstand hundreds of dpa in their lifetime.[54] Nanostructured materials like ODS steels promise an increased resistance to radiation damage due to self-healing mechanisms. Atomistic simulations by Bai *et al.*[55] have shown that grain boundaries can act as sinks for interstitials. The grain boundaries then subsequently act as sources for interstitials, emitting them for recombination with vacancies in the bulk which enhances the annihilation of point defects. Precipitates are, besides

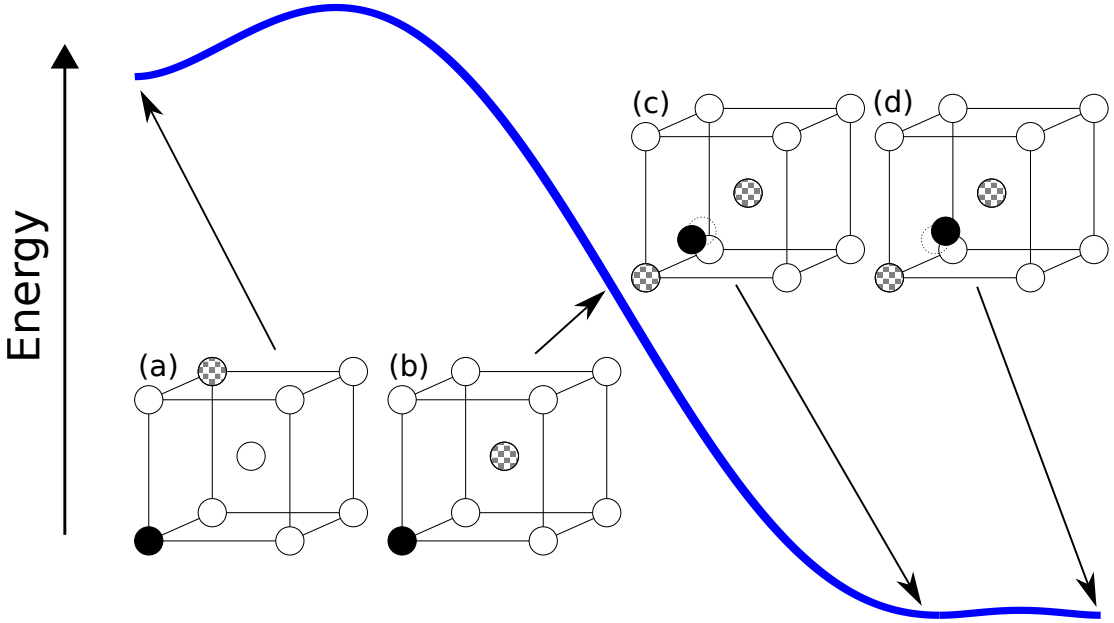

Figure 1.3: Different configurations of yttrium (black circle) and vacancy (checkerboard circle) positions on a bcc-Fe (white circles) lattice and the corresponding energy landscape for transitions between these configurations. Configuration (a) shows yttrium and vacancy in third-nearest neighbor positions. Configuration (b) shows yttrium and vacancy in the nearest neighbor position. This configuration is not stable and relaxes towards configuration (c). Configuration (d) is the equivalent nearest-neighbor position resulting from relaxing configuration (b) with swapped yttrium and vacancy positions. There is only a negligible migration barrier between configurations (c) and (d), so the yttrium atom might also be considered as occupying an interstitial position.

stabilizing the microstructure at elevated temperatures, expected to increase the radiation resistance in a similar fashion.[3]

A recent work by Duan *et al.*[56] analyzed the microstructure of ODS and non-ODS steels prior to and after irradiation and measured the change in hardness. They concluded, that the oxide precipitates in ODS steels are in fact the most important sink for point defects and cause of their unique radiation resistance. The resistance of the precipitates to irradiation damage has been investigated by Certain *et al.*[57] by applying proton, heavy ion and neutron radiation and analyzing the resulting evolution of the precipitate population by TEM and APT measurements. They demonstrated that precipitates in the investigated ODS steel are stable in the temperature and dose rate regime they would experience in application.

1.2.5.2 *Transmutation reactions and He management*

In addition to the radiation damage caused by the displacement of lattice atoms, transmutation reactions can result from neutron activation of atoms. In (n-α) reactions metal nuclei capture the fast neutrons created by fusion reactions and decay by ejecting α-particles.[58] This leads to an accumulation of helium inside of the irradiated material which can lead to significant embrittlement and swelling of the material.[10]

Parish *et al.*[59] irradiated ODS and a castable nanostructured alloy with He and Fe ions, simulating fusion-reactor conditions, and analyzed the resulting distribution of He bubbles. They concluded that He bubbles in the ODS steels are smaller and less concentrated at grain boundaries compared to the reference nanostructured alloy. Simulations can help to explain the causes for these results. Yang *et al.*[60,61] investigated the trapping of helium and vacancies in $Y_2Ti_2O_7$, in the Fe matrix and in the $Y_2Ti_2O_7$/Fe interface and the structure of the interface using DFT calculations. They discovered, that helium preferably accumulates in the oxide precipitates and the interface between precipitate and matrix before forming helium bubbles at the interface.

1.2.5.3 *Reasons for the radiation resistance of ODS steels*

The results mentioned before are only a fraction of the vast research that has been conducted with respect to the effect of radiation on ODS steels. Odette *et al.* authored a series of review articles, that give a detailed overview over the research in this area.[3,9,10,62] In conclusion there are multiple reasons for the unique irradiation resistance of ODS steels:

1. The high density of precipitates provides sinks for vacancies and SIA and enhances recombination.
2. Oxide precipitates trap He generated by (n-α) reactions in nm-sized bubbles.
3. Grain boundaries and dislocations are stabilized by the precipitates and provide additional sinks for diffusing point defects.

The strength of different sinks can depend on various factors, including radiation dose, type of defects and the elastic field that surrounds the sink. Vattre *et al.*[63] investigated the influence of interface strain fields of semicoherent interfaces on the sink strength of Ag-Ag and Ag-Cu interfaces using KMC calculations. They showed that the sink strength of interfaces is highly sensitive to the character of the interfacial stresses. Sivak *et al.*[64,65] used KMC simulations to determine the influence of the elastic fields of dislocations on the diffusion of point defects. They showed that the elastic fields influence the diffusion of vacancies and SIA and that dislocations are more attractive sinks for SIA. A similar mechanism can lead to a strain dependent sink strength of precipitates.

1.3 OPEN QUESTIONS

The previous chapter raised several questions that have determined the direction of the research presented in this thesis, namely:

- **What is the diffusion mechanism of substitutional yttrium atoms?** There is a significant attraction between substitutional yttrium atoms and vacancies. This leads to a relaxation of the yttrium to an interstitial position if it is in a nearest neighbor position to a vacancy.[39] A separation of the resulting yttrium-vacancy pair requires a significant amount of energy and it is unknown if the separation is necessary for the diffusion mechanism.
- **What is the diffusion coefficient of yttrium in iron?** There are no experimental measurements of yttrium diffusion and calculations using Le Claire's nine frequency[51,52] model lead to a significantly faster yttrium diffusion than results from fitting precipitation growth models.[48] The reason for this is difference is unknown and could be related to an unusual diffusion mechanism of yttrium.
- **Is pipe diffusion of yttrium faster than bulk diffusion?** The precipitation and growth models of Barnard *et al.* and Cunningham *et al.* predict that yt-

trium is actually mobile due to pipe diffusion.[49,50] There are, however, neither experimental nor theoretical investigations of yttrium pipe diffusion and the resulting diffusivity is unknown.

- **Are there long ranged interactions between precipitates and point defects that influence the sink strength of the precipitates?** Elastic fields surrounding precipitates could influence the diffusion of vacancies and interstitials. This could lead to a long range attraction or repulsion which would influence the efficiency of the precipitates as sinks for these point defects. A similar effect has been shown to influence the sink strength of semicoherent interfaces[63] and dislocations.[64,65]

2

MULTISCALE MODELLING METHODS

The length and timescale of the problems investigated in this work far exceed the reach of a single simulation technique. Thus, various techniques were combined in a multiscale approach. In the following sections, the different methods used throughout this thesis are introduced.

2.1 DENSITY FUNCTIONAL THEORY

DFT is a computational method that solves the electronic many-body problem to calculate the total energy of an atomic system. In principle this requires solving Schrödinger's equation,

$$\hat{H}\Psi = E\Psi, \tag{2.1}$$

where $\hat{H}$ is the Hamiltonian of the system, Ψ is the wave function and E is the total energy. With an increasing number of electrons N, this task becomes impossible. Hohenberg and Kohn[66] showed that all properties of a quantum mechanical system are completely determined by the ground-state density of the electrons. In particular the energy of the system is a functional of the electron density, $E = E[n]$, and the ground state electron density can be obtained by minimizing that functional.

According to Kohn and Sham[67] the many-body system can be replaced with an auxiliary system of independent particles that can be solved more easily. The total density $n(\mathbf{r})$ of the auxiliary system is expressed as a sum of partial densities generated by the Kohn-Sham wave functions ψ_i:

$$n(\mathbf{r}) = \sum_i n_i = \sum_i \psi_i^*(\mathbf{r})\psi_i(\mathbf{r}) \tag{2.2}$$

Minimizing the energy functional under the constraint of orthonormality of the Kohn-Sham wave functions ψ_i leads to the Kohn-Sham equations:

$$\left[-\frac{\hbar^2}{2m}\nabla^2 + V_{\text{ext}}(\mathbf{r}) + V_H(\mathbf{r}) + V_{XC}(\mathbf{r})\right]\psi_i(\mathbf{r}) = \epsilon_i\psi_i(\mathbf{r}) \tag{2.3}$$

The external potential $V_{\text{ext}}(\mathbf{r})$ defines the interaction between the electron and the atomic nuclei. The Hartree potential $V_H(\mathbf{r})$ defines the mean-field Coulomb repulsion between the electron and the total electron density in the system. These contributions are well defined and can be calculated analytically. All the remaining many-body interactions are put in the exchange-correlation potential $V_{XC}(\mathbf{r})$. The true form of $V_{XC}(\mathbf{r})$ is not known for almost all cases, but the contribution to the total energy is limited and simple approximations have proven to be sufficiently accurate. One of the frequently used approximations is the local density approximation[68] (LDA). Here, $V_{XC}(\mathbf{r})$ is assumed to be the exchange-correlation potential of a particle in an uniform electron gas. The exchange energy can then be derived analytically and the correlation energy was computed numerically by Monte Carlo simulations.[69] Another type of exchange-correlation potentials includes the local gradient in the electron density. This is called the generalized gradient approximation (GGA). A widely used GGA potential is the Perdew-Burke-Ernzerhof[70] potential (PBE). The DFT calculations presented in this work were done using the Vienna Ab initio Simulation Package (VASP).[71–74]

2.2 INTERATOMIC POTENTIALS

As an alternative to expensive *ab initio* calculations, interatomic potentials can be used to calculate the energies and forces of atoms in atomistic simulations. In this case the interaction between atoms is described by an analytic formula, which is computationally a lot cheaper than calculations based on quantum mechanics. This allows to investigate systems containing millions of atoms compared to the hundreds of atoms accessible in DFT calculations.

Depending on the nature of the interaction between atoms and on the required accuracy, different potential types are used for different materials. Pair potentials, like the Lennard-Jones potential,[75] only depend on interatomic distances and are used to describe densely-packed structures. They offer a high computational performance at the cost of a less accurate description of the material. More sophisticated potential types also include three-body or many-body terms, which allow to include the influence of the environment. Metals are often modeled using embedded-atom method (EAM) potentials.[76] This type of potential consists of a two-body term and a multi-body interaction where the influence of the electron charge density is considered using an embedding function.

Potentials for modelling covalently bonded materials need to include the influence of bond angles. Tersoff potentials[77] include this influence using a bond-order

term that depends on the environment of the atoms. Atomic bond-order potentials (ABOPs)[78,79] are another example of such a type of potential. This potential type is very flexible and has been used successfully to describe covalent, metallic as well as ionic systems. Examples include the Pt-C,[78] Ga-As,[79] Si-C,[80] Zn-O[81] and the Fe-Cr-C system.[82] The work presented in this thesis includes the development of an ABOP for the Y-Y interaction and for the Fe-Y interaction.

2.2.1 *Atomic bond-order potentials*

In the ABOP scheme, the potential energy U is written as a sum over individual bond energies,

$$U = \sum_{i<j} f_{ij}^{c}(r_{ij}) \left[V_{ij}^{R}(r_{ij}) - \frac{b_{ij} + b_{ji}}{2} V_{ij}^{A}(r_{ij}) \right], \tag{2.4}$$

with pairwise attractive and repulsive contributions given by

$$V^{R}(r) = \frac{D_0}{S-1} \exp\left(-\beta\sqrt{2S}(r - r_0)\right) \tag{2.5}$$

and

$$V^{A}(r) = \frac{SD_0}{S-1} \exp\left(-\beta\sqrt{2/S}(r - r_0)\right), \tag{2.6}$$

where D_0 and r_0 are the dimer energy and bond length. The parameter β can be determined from the ground state oscillation frequency of the dimer,[79] while S defines the slope of the Pauling plot.[78,79] The cutoff function

$$f^{c}(r) = \begin{cases} 1 & r < R - D \\ \frac{1}{2} - \frac{1}{2}\sin\left(\frac{\pi}{2}\frac{r-R}{D}\right) & |R - r| \leq D \\ 0 & r > R + D \end{cases} \tag{2.7}$$

restricts the interaction range, typically to the first or second next neighbor shell. The parameters R and D specify the position and the width of the cutoff region. Three-body interactions are included via the bond order term

$$b_{ij} = (1 + \chi_{ij})^{-1/2} \tag{2.8}$$

with

$$\chi_{ij} = \sum_{k(\neq i,j)} f_{ik}^{c}(r_{ik}) g_{ik}(\Theta_{ijk}) \exp\left(2\mu_{ik}(r_{ij} - r_{ik})\right) \tag{2.9}$$

and the angular dependence

$$g(\Theta) = \gamma \left(1 + \frac{c^2}{d^2} - \frac{c^2}{d^2 + (h + \cos\Theta)^2}\right). \tag{2.10}$$

The three-body interactions are determined by the parameters 2μ, γ, c, d and h.

2.3 MOLECULAR DYNAMICS

Molecular dynamics (MD) is a computational method that is used for studying the movement of atoms over time. The trajectories of atoms are calculated by numerically integrating the equations of motion:[83]

$$m_i \cdot \frac{d^2\mathbf{r}_i}{dt^2} = \mathbf{F}_i = -\boldsymbol{\Delta} U \tag{2.11}$$

Here m_i and $\mathbf{r}_i$ are the mass and position of the atom i, t is the time and $\mathbf{F}_i$ is the force acting on the atom. The forces acting on the atoms can either be calculated using *ab inito* methods like DFT or can result from evaluation interatomic potentials. In this work, molecular dynamics simulations were done using LAMMPS,[84] which allows the simulation of millions of atoms for time scales of nano- or even microseconds.

In LAMMPS the equations of motion are by default integrated using the velocity Verlet algorithm.[85] The time is divided into discrete time steps δt and the atom positions and velocities are updated after every step:

$$\mathbf{r}_i(t + \delta t) = \mathbf{r}_i(t) + \mathbf{v}_i(t)\delta t + \frac{1}{2}\frac{\mathbf{F}_i(t)}{m_i}\delta t^2 \tag{2.12}$$

$$\mathbf{v}_i(t + \delta t) = \mathbf{v}_i(t) + \frac{1}{2}\frac{\mathbf{F}_i(t) + \mathbf{F}_i(t + \delta t)}{m_i}\delta t \tag{2.13}$$

After each step the time is increased by δt until the total number of steps is reached. LAMMPS allows simulations in various thermodynamic ensembles like the micro-canonical (NVE), canonical (NVT) or isothermal-isobaric (NPT) ensemble. Temperature control is achieved by applying a Nosé-Hoover[86,87] thermostat. The thermostat couples the system to a heat reservoir and regulates the energy flow between the system and the heat reservoir by adding an artificial damping factor to the equations of motion. The pressure is controled by a barostat that controls the volume of the system.[88]

2.4 KINETIC MONTE CARLO

The KMC method is often used to simulate the time evolution of a system, especially if long time scales need to be considered as it is the case in the simulation of diffusion processes. The system evolves due to a series of events with known transition rates. Occurring events are chosen using the *n-fold way* or Bortz-Kalos-Lebowitz (BKL) algorithm:[89]

1. Initialize system and set $t = 0$
2. Create list with all possible events and their respective rate r_i
3. Calculate the cumulative list of rates $R_i = \sum_{n=1}^{i} r_n$ and the total rate $Q = \sum_i r_i$
4. Get a uniform random number $u \in (0, 1]$.
5. Carry out event i for which $R_{i-1} < uQ \leq R_i$
6. Get a new uniform random number $u' \in (0, 1]$.
7. Update the time with $t = t + \Delta t$, where $\Delta t = Q^{-1} \ln(1/u')$.
8. Return to step 2.

An accurate time evolution of the system requires knowledge of all possible events and their respective rates. Assuming that the events are Poisson processes and not correlated, the *n-fold way* algorithm gives the correct time scale for the evolution of the simulated system. If the rates also follow detailed balance, KMC can be used to simulate thermodynamic equilibrium. Arthur F. Voter has written a detailed introduction into the KMC method.[90] The KMC simulations presented in this thesis were done using DISC, a code optimized for the simulation of diffusion events. DISC was developed specifically for the simulations presented in this thesis and is introduced in Chapter 6. Transition rates were determined on the basis of migration barriers calculated from DFT.

3

INTERATOMIC POTENTIALS

Large scale atomistic simulations of ODS steels require an interatomic potential that defines the interaction of the atom types. Ideally, this would include all interactions between iron, yttrium, oxygen and titanium atoms. Hammond *et al.*[91] developed a simple Buckingham potential for this system, which reproduces the mechanical and thermodynamic properties of the pure metals to a certain degree. The simple pair potential approach, however, severely limits the transferability of the potential, which shows in the poor reproduction of melting points and point defect energies.

Yashiro *et al.*[92] developed an even simpler pair potential to investigate the interaction of dislocations with precipitates. They approximated Y_2O_3 precipitates by not distinguishing yttrium and oxygen atoms, but treating them as one atom type. This approach allows for a straightforward fit to DFT results, but roughly simplifies the interface formation and the interaction between interface and dislocation. This shows that there is a significant demand for a potential that allows large scale MD simulations in the context of ODS steels, but is still sufficiently accurate to deal with complex situations like interfaces and defects. There is no potential for the whole Fe-Y-Ti-O system, but some components can already be found in literature.

Iron is a material of considerable technological importance, therefore several interatomic potentials for the iron-iron interaction exist.[93–97] Müller *et al.*[97] created an ABOP potential that mimics the influence of the magnetic degrees of freedoms implicitly by a fit to the Gibbs free energies of the corresponding solid phases. This allows for an accurate description of the phase transition sequence from α-iron to γ-iron and δ-iron. It also reproduces a large variety of surface, bulk and defect properties, properly. The publication also includes a comparison to four other potentials for iron. The potential has been extended by Henriksson *et al.*[82] to include Cr and C.

The yttrium-yttrium interaction has also been modeled using interatomic potentials. Fan *et al.*[98] have created an ABOP parameter set which has, however, severe deficits in reproducing the bcc phase of yttrium and a huge cut-off range which makes it unsuitable for iron-yttrium compounds. The yttrium-yttrium interaction has also been modeled using the EAM formalism[99] and modified embedded-atom method (MEAM) formalism,[100,101] but these formalisms are not directly compatible

to the ABOP formalism. For these reasons, we developed a new parameterization for the yttrium-yttrium interaction. To the best of our knowledge, there is no parameterization for the iron-yttrium interaction in literature. Therefore the parameterization for this interaction is also developed in Chapter 5 of this work.

4

ATOMICREX

This chapter is a shortened version of Ref. [102], with a focus on points that were relevant in the context of this thesis.

4.1 INTRODUCTION

The development of interatomic potentials requires a tool that is flexible and efficient enough to fit the potential to a large database of diverse properties. While various potential development tools have been developed for internal use by research groups, relatively few have been made widely available including e.g., POTFIT,[103] GARFFIELD,[104] MEAMFIT,[105] the "EAM Alloy Potential Generator",[106] and the aenet package for artificial neural network (ANN) potentials.[107] Several of these codes target specific potential types and/or functional forms. They can be difficult to extend and/or integrate with other processing pipelines, in particular the popular Python scripting language. The potential development in this thesis was done using ATOMICREX, an open-source code that was developed in part concurrently with the Fe-Y potential described in Chapter 5. The main features of ATOMICREX are:

- support for a variety of interatomic potential forms,
- the possibility for the user to define arbitrary functional forms via a built-in math expression parser,
- very high computational efficiency enabling large training and validation sets,
- a range of predefined properties that can be combined to generate more complex properties, in particular energy differences, defect energies, etc., which can be included in both training and validation stages,
- an interface to the popular Python programming language, which enables interfacing with various third-party libraries, and
- an object-oriented code framework that readily allows addition of new potential models, structures, and properties.

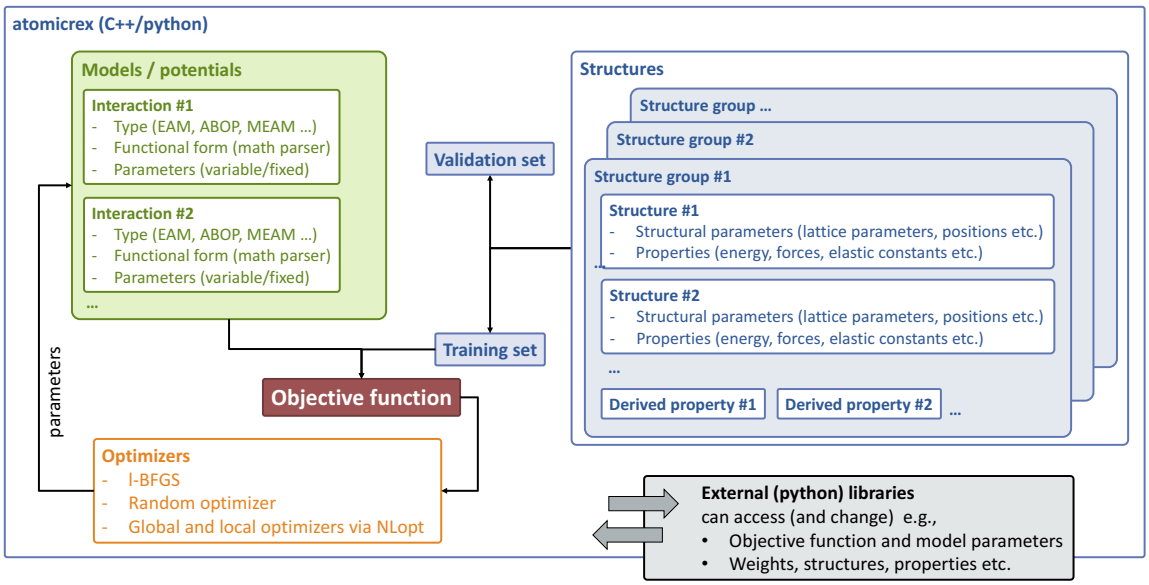

Figure 4.1: Schematic overview of the different objects handled by ATOMICREX and their connections.

The potentials created using ATOMIREX can be used in simulation codes such as LAMMPS or ATOMISTICA,[108] but can also be made available to the scientific community e.g., via the Knowledgebase for Interatomic Potentials.[109,110]

ATOMICREX is available under the GNU General Public License and is hosted in a public Git repository on GitLab, where its source code is available for download and which can be accessed via `http://atomicrex.org`. Most of the code base is written in C++, with Python bindings enabling integration with third-party libraries and custom model fitting schemes. An extensive user guide that contains a comprehensive description of features, input file parameters, and the Python interface along with various examples is available online. A separate documentation of the C++ and Python application programming interfaces (APIs) are available as well.

4.2 WORKFLOW

From a technical point of view, ATOMICREX processes a user-supplied input file in the extended markup language (XML) format that describes the job to be performed. The specific format of this file and an extensive user guide is available

online. A general overview of the objects and entities that play a role in the architecture of ATOMICREX is provided in Figure 4.1. Generally, a job can be divided into two parts, the training phase and the output phase. During the training phase selected degrees of freedom (DOFs) (parameters) of the model (usually an interatomic potential) are varied such that the predicted properties (energies, forces, elastic constants, etc., see Section 4.5) most closely match the target data.

The training phase is followed by the validation phase. Here, additional properties of interest can be calculated that were not included in the fitting. This allows a convenient separation of the available data into training and validation sets, where the latter serve to assess the predictive capability of a model. Once the training process has been completed, the resulting model can be exported in various forms adequate for the use with popular atomistic simulation codes such as LAMMPS.

4.3 POTENTIALS

A potential consists of a parameter set and a specific routine that calculates the total energy and the forces for a given atomic structure. ATOMICREX supports a number of different potential types that at present include e.g,

- the EAM,[76]
- the MEAM,[111]
- Tersoff-Abell style potentials,[112,113]
- ABOPs in the generalized Brenner format,[78,80,81,114,115]
- the concentration dependent embedded-atom method (CD-EAM) format,[116–118]
- the angular dependent potential (ADP) format,[119] and
- Stillinger-Weber style potentials,[120]

where the latter two can be constructed from user defined functionals using the MUPARSER math parsing library.[121] All the potential types can be combined to develop potentials for complex multi-component systems that cannot be described by a single model.

4.4 STRUCTURES

Structures are one of the basic constituents of the fitting procedure of ATOMICREX. They can be sorted into groups, which simplifies handling big collections and rating the relative importance of different structures. Every structure has a set of properties, like the atomic energy or the bulk modulus, that can be included in the training or solely in the validation phase of the potential. ATOMICREX contains a large database of predefined crystal structures as well as some non-periodic structures. Lattice constants, axial ratios or atom positions of these predefined structures can be relaxed and used as properties for fitting purposes. Fitting to point defect energies is simplified by the predefined *defect structure* type that can be used to construct arbitrary orientations and compositions of defects and defect complexes.

In addition to these predefined structures, custom structures can be defined in the XML input file or imported from external files. Structure databases can be kept in separate files to reference and re-use them for more than one fitting job. The cells as well as the atomic positions of these custom structures can also be relaxed prior to the calculation of properties, but cell dimensions can not be used as properties in these cases. The internal DOFs (atom positions, lattice parameters etc.) of a structure that are activated for relaxation, are optimized before the properties are calculated.

4.5 PROPERTIES AND THE OBJECTIVE FUNCTION

Properties depend on one or multiple structures and the potential used to calculate the energies and forces. Most properties are simple scalars such as the total energy of the structure, but vector properties such as the forces acting on the atoms of the structure are also possible. By default most properties are only calculated when explicitly activated, either for the training and/or the validation phase.

In addition to the properties that are directly connected to one structure, there is an additional type of properties that can depend on multiple structures. These derived properties are specified by providing a user defined formula, which may reference the values of properties of several other structures. For example, it is possible for the user to define a defect formation energy by subtracting the reference energy, computed from an ideal unit cell, from the total energy of a supercell containing the defect. ATOMICREX takes care of computing all input properties that enter into the user-defined formula for the derived property, making it possible to fit a potential to defect formation energies, energy differences between phases,

surface energies, or specific phonon frequencies. This feature was key for fitting the potential to the defect formation and binding energies in Chapter 5.

All properties that are active in the training phase contribute to the objective function and require a target value, that should be matched by the potential. The objective function is the main quantity computed by ATOMICREX and is minimized in order to optimize the potential. The value of every property is calculated using the current parameter set and compared to the target value in order to calculate the residual. The objective function is the weighted sum of all residuals. Weights can be assigned on the level of structure groups, structures or individual properties, providing fine-grained control over the importance of different targets during the fitting process.

4.6 OPTIMIZER

Optimization algorithms are used in two sections of the workflow of ATOMICREX. The potential parameters are optimized with respect to the objective function, while the internal DOFs of every structure are optimized during each evaluation of the objective function. Optimization of the model parameters is often a high-dimensional and very noisy problem. A gradient-based optimization algorithm will often lead to inadequate temporary parameters during the optimization. This results in a difficult relaxation of the internal DOFs of the structures which slows down the fitting process. Local gradient-free or global algorithms are often a better choice for the optimization of the parameter set. The relaxation of structures on the other hand is done more efficiently using a gradient-based algorithm as L-BFGS-B. At present ATOMICREX *directly* supports the following local and global optimization algorithms, which are selected in the input file:

- the limited-memory Broyden-Fletcher-Goldfarb-Shanno (L-BFGS-B) minimizer, which is a popular quasi-Newton method with support for bound constraints,
- the "simply poking around" (SPA) minimizer, which randomly samples the parameter space, and
- all algorithms provided by the NLOPT library,[122] which includes methods for global optimization, local derivative-free optimization, and local gradient-based methods.

In addition an even larger number of optimization algorithms are accessible via the Python interface in combination with third-party libraries such as SCIPY[123] and SCIKIT-LEARN.[124]

4.7 CONCLUSIONS AND OUTLOOK

In this chapter, we have described the ATOMICREX code, which provides a flexible, extensible, and efficient framework for the construction of atomic scale models suitable for e.g., molecular dynamics and Monte Carlo simulations. ATOMICREX supports a variety of interatomic potential types, and their functional form can be freely determined by the user via a built-in math parser. The code has been optimized for computational efficiency, enabling larger training and validation sets. While it already includes an extensive database of predefined structures and properties, it also allows the inclusion of custom structures and the definition of complex *derived properties* that are based on the combination of several individual properties and/or structures. Finally, ATOMICREX provides an interface to the Python scripting environment for integration with many advanced scientific libraries available in the Python ecosystem. The code is provided under an open-source license and available via `http://atomicrex.org`. We also provide an extensive user guide with many examples and a comprehensive description of features.

ATOMICREX continues to be developed with an emphasis on code extensibility and speed. In fact, while it already provides an excellent platform not only for the development of potentials using "classic" functional forms (EAM, ABOP, MEAM etc.), it can be extended to include e.g., artificial neural network (ANN) potentials,[107,125,126] tight binding models,[127] or Gaussian approximation potentials.[128] In this context, we provide a full documentation of the application programming interface (available as part of the Git repository) to enable other researchers to contribute to the development e.g., via new models (potentials) or optimization schemes.

The Python interface allows easy and seamless integration with various existing libraries for scientific computing and machine learning like SCIPY,[123] SCIKIT-LEARN,[124] or TENSORFLOW.[129] This opens up the possibility to employ variable training and validation sets for e.g., Bayesian error estimation (see e.g.,[130]), or manipulate the parameter vector using genetic algorithms. Finally, via its ASE interface, ATOMICREX can be readily integrated in a dynamic workflow that spans from the generation of reference data using first-principles codes via training and validation of an atomistic model all the way to deployment of the model in molecular dynamics or Monte Carlo simulations. Hence, it can be employed in, for example,

on-the-fly scale-bridging simulations.[131] In Chapter 5 ATOMICREX is used to create an ABOP for the iron-yttrium system.

Part II

POTENTIAL DEVELOPMENT

5

A POTENTIAL FOR THE IRON-YTTRIUM SYSTEM

Results in this section were first published in Ref. [132].

Large scale atomistic simulations of ODS steel require a fast and accurate way of modelling the atomic interactions. An interatomic potential enables MD simulations of important features like precipitates, dislocations and their interactions. This allows to investigate the mechanical properties, radiation effects or countless other phenomena in ODS steels. A review of existing interatomic potentials was already presented in Chapter 3. In this chapter, we develop an ABOP for the Fe-Y interaction. The Fe-Fe interaction is taken from the work of Müller *et al.*,[97] the Y-Y interaction is developed in Section 5.2 and the Y-Fe interaction in Section 5.3.

The new potential is used to investigate the interaction between substitutional yttrium atoms and dislocations in bcc iron. Due to the MA used during the fabrication, the dislocation density of ODS steels is significant and dislocation strengthening is a significant part of the mechanical properties.[133,134] APT measurements have shown an enrichment of solute atoms, including Y, in the vicinity of dislocations.[25] Since modelling the core structure of screw dislocations in bcc Fe is a delicate issue,[135–137] we focus on the interaction between point defects and edge dislocations due to the simpler core structure of edge dislocations. Furthermore, the stress field of an edge dislocation includes hydrostatic components which will increase the interaction with the stress field of point defects.[138] The segregation of yttrium atoms at edge dislocations and the pinning of the dislocations by the substitutional yttrium atoms is investigated in Section 5.4.

5.1 TOTAL-ENERGY CALCULATIONS

The transferability of the potential depends on fitting to an extended reference database of differently coordinated structures. Experimental data is only available for a limited number of structures. Thus, data from DFT calculations were also used to fill the fitting database. These calculations were carried out with VASP using a plane wave basis set with pseudopotentials from the VASP library based on the projector augmented-wave (PAW) method[139,140] and within the generalized-gradient approximation (GGA) in the Perdew-Burke-Ernzerhof (PBE) parameterization.[70]

The plane wave energy cut-off was set to 500 eV and relaxation of the electronic degrees of freedom was stopped once the total (free) energy change and the band structure energy change between two steps are both smaller than 1×10^{-6} eV. The convergence criterion for the relaxations was achieved when all forces were less than 1 meV Å^{-1}. The point defect and climbing-image nudged elastic band (CI-NEB)[141] calculations were done with 4x4x4 supercells, where the Brillouin zone sampling was done on a 3x3x3 k-point grid.

Table 5.1 shows the results of the DFT calculations for yttrium structures. Lattice and elastic constants of hcp-Y show good agreement to experimental results. Additional to the ground-state hcp structure the properties of yttrium in body-centered cubic (bcc), face-centered cubic (fcc), diamond (dia) and simple cubic (sc) structure were investigated. Experimental data on FeY structures is very scarce. Here, DFT calculations were essential for constructing the fitting database for the Fe-Y interaction. Investigated structures included α-Y_2Fe_{17}, β-Y_2Fe_{17}, Y_6Fe_{23}, YFe_2, YFe_3 and YFe_5. Results of these calculations in comparison to the potential can be found in Table 5.4. Another big part of the fitting database for the Fe-Y interaction were the formation energy of substitutional yttrium and the binding energy to a vacancy.

Table 5.5 shows the formation energy of a substitutional yttrium atom in a bcc-Fe lattice and the binding energies between a substitutional yttrium atom and vacancies. The substitutional energy E_s^f was calculated by

$$E_s^f = E_d - n\mu_{Fe} - \mu_Y, \tag{5.1}$$

where E_d is the energy of the supercell including the defect, n the number of Fe atoms in the supercell, μ_{Fe} the chemical potential of Fe in bcc-Fe and μ_Y the chemical potential of yttrium in hcp-Y. The binding energy E_i^b between yttrium atom and vacancy in distance i was calculated according to

$$E_i^b = [E_Y + E_V] - [E_i + E_{super}], \tag{5.2}$$

where E_Y is the energy of a supercell including a single substitutional yttrium atom, E_V is the energy of a supercell including an isolated vacancy, E_i is the energy of the supercell with yttrium atom and vacancy in distance i and E_{super} is the energy of the supercell without any defects. NEB calculations of vacancy jumps in the vicinity of yttrium atoms were carried out to determine the minimum energy paths. The resulting migration barriers are shown in Table 5.6 and were part of the testing database of the potential.

5.2 YTTRIUM-YTTRIUM INTERACTION

Yttrium is a soft, silver-metallic transition metal. It is chemically similar to the lanthanides and has often been classified as a rare-earth element. At temperatures below 1478 °C it crystallizes in the hexagonal closed-packed crystal structure. At higher temperatures the body-centered cubic crystal structure (bcc) is stable in a narrow temperature window up to the melting point at 1522 °C.[142] The experimental properties of the stable hcp phase can be found in literature, while properties for other crystal structures were calculated by DFT.

Table 5.1 compares the bulk properties of yttrium according to the potential to experimental and DFT data. The agreement with respect to lattice constants and elastic properties is reasonable. Considerable attention was placed on the correct representation of the energy difference between the hcp and the fcc phase of yttrium. This energy difference is connected to the stacking fault energy which is important for the proper description of mechanical properties.

Point defect formation energies are presented in Table 5.2. The vacancy formation energy shows very good agreement with the experimental value. The interstitial formation energies E_i^f are significantly influenced by the range of the cut-off function. During the fitting process it became obvious that large cut-off values improved the interstitial formation energies, but led to problems during the development of the yttrium-iron potential in Section 5.3. The yttrium-yttrium distances in the yttrium-iron structures vary widely and may even be lower than the yttrium-yttrium distance in hcp or bcc yttrium. Therefore, it was not possible to fix the cut-off to a value that includes only first and second nearest neighbors as it was done for the Fe-Fe interaction. As a solution the cut-off was treated as an adjustable parameter in order to find values for the cut-off distances R and the width of the cut-off region D (table 5.3) that give a largely accurate order of the formation energies without inhibiting the fitting of the yttrium-iron potential.

The thermal properties shown in Table 5.1 are part of the testing database and were calculated in order to validate the transferability of the potential. The measured thermal expansion from 0.1 ns MD calculations is fully in line with experimental values. The melting point was determined by running molecular-dynamics simulations of a solid-liquid interface as shown in Figure 5.1a. The system consisted of 8000 atoms with half of the atoms in the solid and half of the atoms in the liquid phase. The system size in x and y direction was fixed according to the lattice constant of the crystalline phase at the respective temperature while the barostat adjusted the z dimension to keep the pressure at 0 bar. For different temperatures

Table 5.1: Structural and cohesive properties of yttrium in various phases.

		Literature		
	DFT	Experiment	Theory	ABOP
Dimer				
E^b (eV)		1.62[a]	2.56[b], 2.44[c]	1.75
r_b (Å)			3.03[b], 3.03[c]	2.97
Hexagonal close-packed ($P6_3/mmc$)				
a (Å)	3.658	3.647[d], 3.6482[e]	3.637[f]	3.64
c (Å)	5.677	5.731[d], 5.7318[e]	5.674[f]	5.70
E^c (eV)		-4.37[g]	-4.31[f]	-4.37
B (GPa)	41.2	41.3[h], 41.2[e]	41.6[f]	42.3
c_{11} (GPa)	68.2	77.9[h], 77.9[e]	76.9[f]	70.5
c_{12} (GPa)	33.4	29.2[h], 28.5[e]	24.6[f]	28.9
c_{13} (GPa)	22.2	20.0[h], 21.0[e]	22.9[f]	27.1
c_{33} (GPa)	80.4	76.9[h], 76.9[e]	79.6[f]	73.5
c_{44} (GPa)	25.3	24.3[h], 24.31[e]	25.5[f]	37.1
α_a ($\mu m\,m^{-1}\,K^{-1}$)		6.0[e]		8.1
α_c ($\mu m\,m^{-1}\,K^{-1}$)		19.7[e]		18.1
T_m (K)		1795[h]		1727
Body-centered cubic ($Im\bar{3}m$)				
a (Å)	4.041	4.1[e]		4.05
ΔE (eV)	0.12		0.127[f]	0.01
B (GPa)	39.1			43.3
Face-centered cubic ($Fm\bar{3}m$)				
a (Å)	5.062			5.08
ΔE (eV)	0.03		0.022[f]	0.03
B (GPa)	38.21			42.0
Diamond ($Fd\bar{3}m$)				
a (Å)	7.041			7.21
ΔE (eV)	1.98		1.939[f]	1.55
Simple cubic ($Pm\bar{3}m$)				
a (Å)	3.285			3.34
ΔE (eV)	0.78		0.772[f]	1.26

[a] Ref. [143] [b] Ref. [144] [c] Ref. [145] [d] Ref. [146] [e] Ref. [147] [f] Ref. [98]
[g] Ref. [148] [h] Ref. [149]

Table 5.2: The vacancy formation energy E^f_{vac} and the interstitial formation energies E^f_i in eV. The different interstitial configurations are explained in Ref. [98].

	Literature		
	Experiment	Theory	ABOP
E^f_{vac}	1.25[a]	1.30[b], 1.69[c]	1.25
$E^f_i(T)$		2.90[c]	3.21
$E^f_i(O)$		2.48[c]	4.09
$E^f_i(C)$		2.76[c]	3.02
$E^f_i(S)$		2.86[c]	3.33
$E^f_i(BT)$		2.96[c]	3.96
$E^f_i(BO)$		2.12[c]	2.80
$E^f_i(BC)$		2.12[c]	2.75
$E^f_i(BS)$		2.61[c]	3.17

[a] Ref. [150] [b] Ref. [151] [c] Ref. [98]

Table 5.3: Parameter set for describing Fe-Fe, Y-Y and Fe-Y interactions. Fe-Fe parameters according to Müller *et al.*[97]

	Fe-Fe	Y-Y	YFe-A	YFe-B
r_0 (Å)	2.29	2.970 826 486	2.343 393 342	2.668 740 276
D_0 (eV)	1.5	1.746 503 433	2.418 820 239	1.238 647 739
β (Å^{-1})	1.4	0.831 119 246	0.823 609 633 6	0.769 757 881
S	2.0693109	1.445 930 960	1.956 621 216	1.704 183 914
γ	0.0115751	$3.162\,169\,8 \times 10^{-6}$	0.156 003 050 1	0.057 166 523
c	1.2898716	97.073 112 50	53.673 583 61	18.907 934 44
d	0.3413219	0.484 474 929	10.097 550 41	50.451 783 59
h	-0.26	0.705 506 699	−0.877 542 060 6	−0.892 747 19
2μ (Å^{-1})	0.0	0.248 603 584	0.066 131 369 93	0.167 582 119
R (Å)	3.15	4.312 903 829	4.203 940 055	4.070 238 849
D (Å)	0.2	0.100 340 985	0.159 405 86	0.357 539 962

around the melting point the change in total energy as a function of time dE/dt was recorded as shown in Figure 5.1b. At the melting point the solid-liquid interface is stationary which corresponds to $dE/dt = 0$. The resulting melting point is at (1727 ± 8) K, which is in good agreement with the experimental melting point of 1795 K.

5.3 IRON-YTTRIUM INTERACTION

The yttrium-iron phase diagram contains the crystal structures α-Y_2Fe_{17}, β-Y_2Fe_{17}, Y_6Fe_{23}, YFe_3 and YFe_2. Due to the lack of technological relevance, the mechanical properties of these intermetallic compounds are not reported in literature. Experimental data on the thermodynamics and crystal structures have been collected by Zhang *et al.*.[142] Modeling of yttrium-iron system has been done by Coehoorn *et al.*[152] and Kardellass *et al.*.[153]

Most of the iron-yttrium phases have rather complicated crystal structures with big unit cells, which leads to different challenges in the fitting process. For the intended purpose - simulations in the context of ODS steels - the interaction of point defects in iron are more important than the intermetallic compounds. Therefore, we created two different yttrium-iron parameter sets. YFe-A was fitted primarily with point defect interactions in mind while the fitting process of YFe-B put more weight on the iron-yttrium phases.

Table 5.4 compares the properties of yttrium-iron compounds with the results of the potential. The elastic properties are adequately reproduced by both potentials, but the lattice constants are slightly inflated. The cohesive energies are accurate for the iron rich phases but deviate slightly for the yttrium rich phases. This effect is more pronounced for YFe-A than for YFe-B.

The energies of yttrium point defects in bcc-Iron are shown in Table 5.5. Both potentials reproduce the formation energies of substitutional yttrium atoms E_s^f, although YFe-A is more accurate in that respect. The difference is even more pronounced when considering the defect formation volume V_s^f, which is nearly perfectly reproduced by YFe-A while YFe-B shows severe differences to the DFT results.

Due to the significant size difference between yttrium and iron atoms there is a strong binding energy between substitutional yttrium atoms and vacancies. This is in particular true for the nearest neighbor configuration, where the yttrium atom leaves its lattice position and relaxes towards the vacancy[39] leading to a configuration that can also be seen as an interstitial yttrium atom between two vacancies.

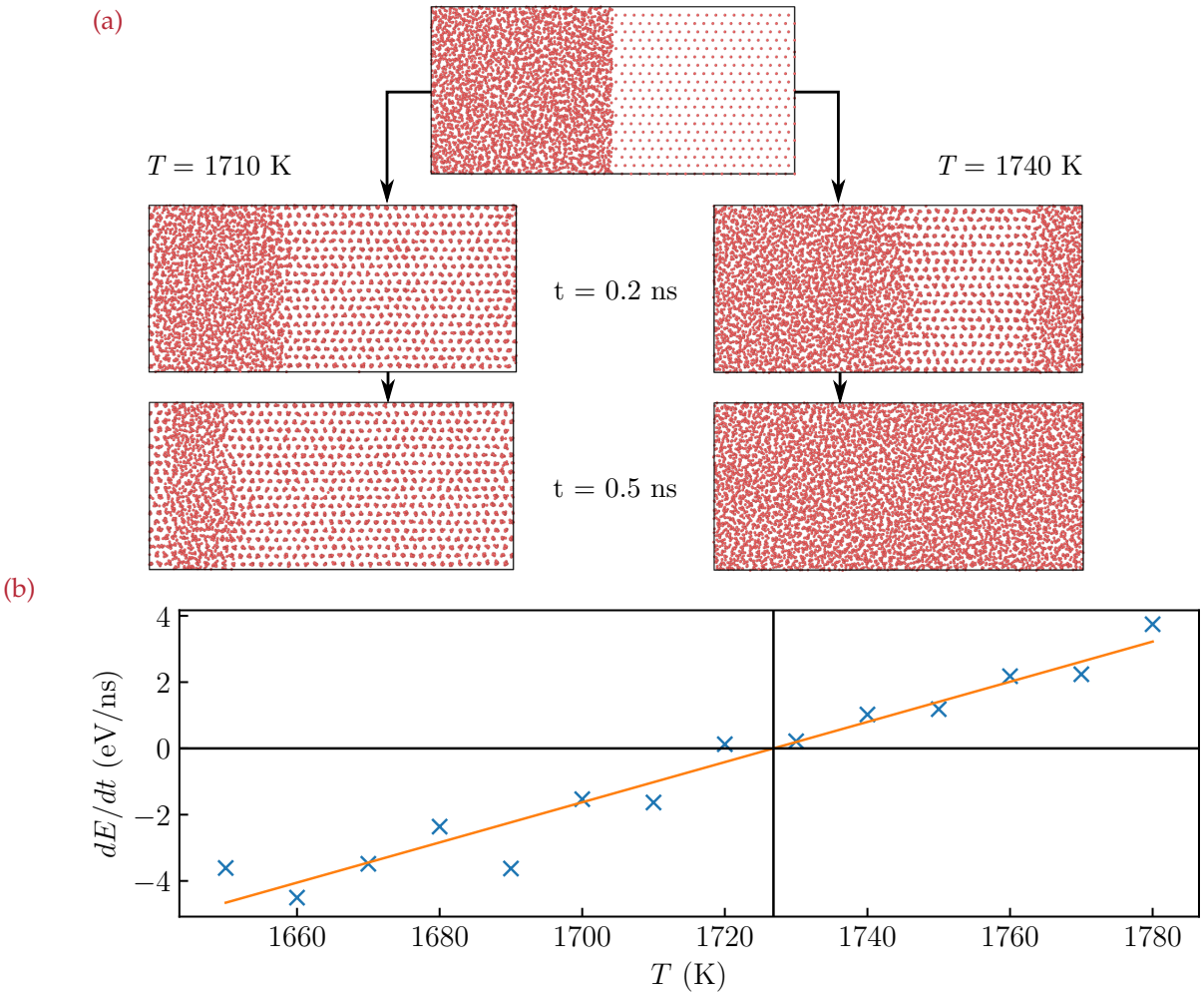

Figure 5.1: (a) Solid-liquid interface at 1710 K (left column) and 1740 K (right column). At the start of the simulation 50 % of the atoms are in the hcp phase and 50 % are in the liquid phase. Below the melting point (left column) the crystalline phase grows with time while at temperatures above the melting point (right column) the amount of liquid phase increases. (b) Slope of the total energy curve with time $\frac{dE}{dt}$ calculated from solid-liquid interface simulations at different temperatures. At a slope of zero, the interface is not moving anymore and the solid and liquid are in equilibrium.

Table 5.4: Comparison of structural and cohesive properties of different YFe phases. Lattice constants a and c in Å, binding energy E^c in eV and bulk modulus B in GPa.

		Literature			
	DFT	Experiment	Theory	YFe-A	YFe-B
α-Y_2Fe_{17} ($P6_3/mmc$)					
a	8.30	8.46[b]		8.60	8.62
c	8.22	8.28[b]		8.42	8.33
E^c	-4.24			-4.27	-4.25
B	124			116	117
β-Y_2Fe_{17} ($R\bar{3}m$)					
a	8.30	8.46[b]		8.60	8.63
c	12.33	12.41[b]		12.66	12.48
E^c	-4.24			-4.27	-4.26
B	99		160[a]	115	117
Y_6Fe_{23} ($Fm\bar{3}m$)					
a	11.87	12.08[b]		12.31	12.21
E^c	-4.29			-4.26	-4.23
B	117			109	109
YFe_2 ($Fd\bar{3}m$)					
a	7.28	7.36[b]		7.73	7.56
E^c	-4.37			-3.99	-4.20
B	85			64	67
YFe_3 ($R\bar{3}m$)					
a	5.11	5.14[b]		5.21	5.21
c	24.29	24.61[b]		26.27	25.30
E^c	-4.37			-4.16	-4.22
B	85		130[a]	90	89
YFe_5 ($P6/mmm$)					
a	5.03			5.06	5.10
c	3.93			4.25	4.08
E^c	-4.34			-4.27	-4.24
B	104			94	106

[a] Ref. [152] [b] Ref. [142]

Table 5.5 shows the yttrium-vacancy binding energies from the nearest neighbor to the fifth nearest neighbor position calculated by DFT and by our potentials. YFe-A shows a reasonable agreement between the DFT calculated reference values and resulting values. YFe-B was created with more focus on the intermetallic compounds and shows some deficits with respect to the yttrium-vacancy binding energies. Especially the repulsive interaction between yttrium and vacancy at third, fourth and fifth nearest neighbor distance does not agree with the DFT results.

Table 5.5 also shows the energies of point defects in fcc iron. Getting reference values from DFT is more complicated for the fcc phase as, while it is experimentally known to be paramagnetic, *ab inito* calculations at 0 K predict it to be paramagnetic, antiferromagnetic, ferromagnetic or magnetically unstable depending on the lattice constant and structural distortion.[156] Gopejenko *et al.*[40] calculated point defect energies in a non magnetic matrix as they were concerned with the precipitate formation that occurs at elevated temperatures. Hepburn *et al.*[155] tried to include magnetic effects by using the face-centered tetragonal, antiferromagnetic double layer collinear-magnetic state of Fe as the matrix. The resulting formation energy of a substitutional yttrium atom varies widely depending on the magnetic state of the matrix with the values calculated using YFe-A and YFe-B somewhere in between the DFT results.

The migration barriers for vacancy jumps in the vicinity of a substitutional yttrium atom in bcc iron are shown in Table 5.6. The label E_{12}^{mig} means that the vacancy moves from the nearest neighbor position to the second nearest neighbor position, E_{51}^{mig} is a vacancy jump from the fifth nearest neighbor position to the nearest neighbor position and so forth. The vacancy jumps in the vicinity of an yttrium atom are discussed at length in Section 7.1. Migration barriers are part of the testing database. The migration barriers calculated using YFe-A are basically identical with the DFT calculated reference values. Especially, the E_{13}^{mig} has basically the same energy in the YFe-A potential as in the DFT calculations. This is important as this is the relevant jump for the diffusion of yttrium in iron.[157]

The Fe-Y phase diagram[153] predicts a decrease of the melting temperature of iron with increasing yttrium concentration in the liquid phase and a decrease of the melting temperature of yttrium with increasing iron concentration in the liquid phase. This was investigated with the same setup that was used to determine the melting point in Section 5.2, but a fraction of the atoms in the liquid phase were replaced by atoms of the respective other type. Figure 5.2a shows the melting point of iron as a function of yttrium content in the melt. Both potentials predict the

Table 5.5: Point defect energies calculated with the potentials. The formation energy of a substitutional yttrium atom E_s^f is giving in eV, the formation volume of a substitutional yttrium atom in $Å^3$ and the yttrium-vacancy binding energy in the x nearest neighbor distance E_{xNN}^b is in eV.

	DFT (eV)	Literature (eV)	YFe-A	YFe-B
bcc-Fe ($Im\bar{3}m$)				
E_s^f	2.06	2.03[a], 2.01[c], 2.02[f], 1.86[e]	2.09	2.26
V_s^f	14.8		14.0	6.7
E_{1NN}^b	1.22	1.45[b], 1.27[c], 0.69[d]	1.20	1.42
E_{2NN}^b	0.23	0.26[b], 0.20[c]	0.14	0.00
E_{3NN}^b	0.13	0.24[b], 0.13[c]	0.10	-0.09
E_{4NN}^b	0.04	0.15[b], 0.04[c]	0.05	-0.08
E_{5NN}^b	0.18	0.25[b], 0.20[c]	0.17	-0.04
fcc-Fe ($Fm\bar{3}m$)				
E_s^f		0.48[g], 1.99[h]	0.94	1.81
E_{1NN}^b		1.67[g], 1.15-1.39[h]	0.52	1.75
E_{2NN}^b		-0.21[g]	0.07	-0.12
E_{3NN}^b		0.30[g]	0.09	0.04
E_{4NN}^b		0.40[g]	0.04	0.02

[a] Ref. [154] [b] Ref. [51] [c] Ref. [39]
[d] Ref. [52] [e] Ref. [42] [f] Ref. [43]
[g] Ref. [40] (non-magnetic fcc) [h] Ref. [155], (antiferromagnetic double layer collinear-magnetic face-centered tetragonal)

Table 5.6: Diffusion barriers of vacancy jumps in the vicinity of a substitutional yttrium atom. E_V^{mig} refers to a vacancy jump in bulk bcc Fe whild E_{ij}^{mig} is a jump from the i'th nearest neighbor position to the j'th nearest neighbor position. Values calculated using DFT are compared to values calculated using YFe-A.

jump	DFT (eV)	Lit (eV)	YFe-A	jump	DFT (eV)	Lit (eV)	YFe-A
E_V^{mig}	0.68	0.65[a]	0.89	E_{11}^{mig}	0.01	0.03[a], 0.09[b]	-
E_{12}^{mig}	1.94	2.05[a], 1.81[b]	1.96	E_{21}^{mig}	0.95	0.92[a], 0.91[b]	0.87
E_{13}^{mig}	1.24	1.33[a], 0.93[b]	1.29	E_{31}^{mig}	0.15	0.18[a], 0.04[b]	<0.01
E_{15}^{mig}	1.05	1.15[a], 0.86[b]	1.19	E_{51}^{mig}	0.01	0.02[a], 0.12[b]	<0.01
E_{24}^{mig}	0.72	0.75[a], 0.69[b]	0.84	E_{42}^{mig}	0.53	0.66[a], 0.69[b]	0.75

[a] Ref. [51] [b] Ref. [52]

same reduction of the melting point with increasing yttrium content, which is in qualitative agreement with the phase diagram.

The melting point of yttrium as a function of the composition is shown in Figure 5.2b. Results for YFe-B show a decrease in melting point with increasing iron content in the melt as predicted by the phase diagram. In simulations done using YFe-A the melting point is essentially constant. This difference is caused by the tendency of the iron atoms in the yttrium melt to cluster. With YFe-A the iron atoms cluster together and form a second phase of liquid iron as shown in Figure 5.3a. This phenomenon does not happen if the YFe-B parameter set is used. Here, the iron atoms stay uniformly distributed in a single phase liquid which is in agreement with the Y-Fe phase diagram. The differences between the two parameter sets are a result of the different fitting priorities. While fitting YFe-B, more weight was placed on reproducing the properties of the YFe lattice structures, while YFe-A was fitted with more weight on reproducing yttrium point defects in an iron matrix. This has led to a superior performance of YFe-A in iron dominated situations while YFe-B shows more transferability to situations with a higher amount of yttrium.

5.4 DISLOCATION INTERACTIONS

In the following section, the parameter set YFe-A was used to investigate the interactions of substitutional yttrium and vacancies with dislocations. Section 5.4.1 deals with the segregation of yttrium atom to a dislocation, Section 5.4.2 with the

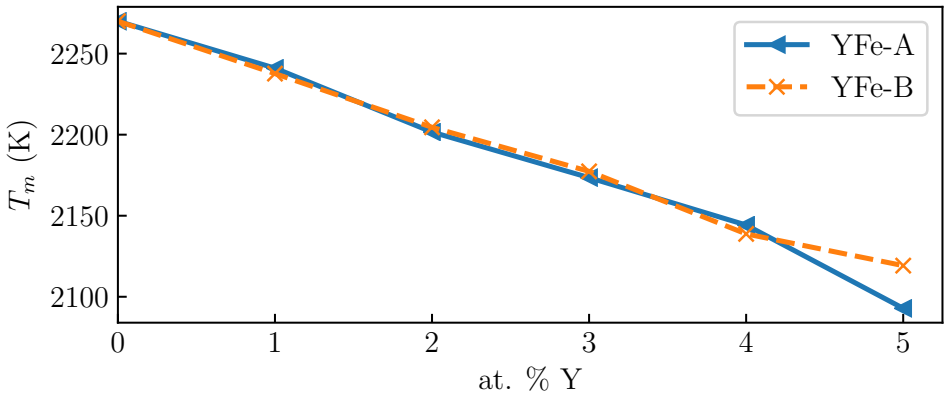

(a) Iron melting

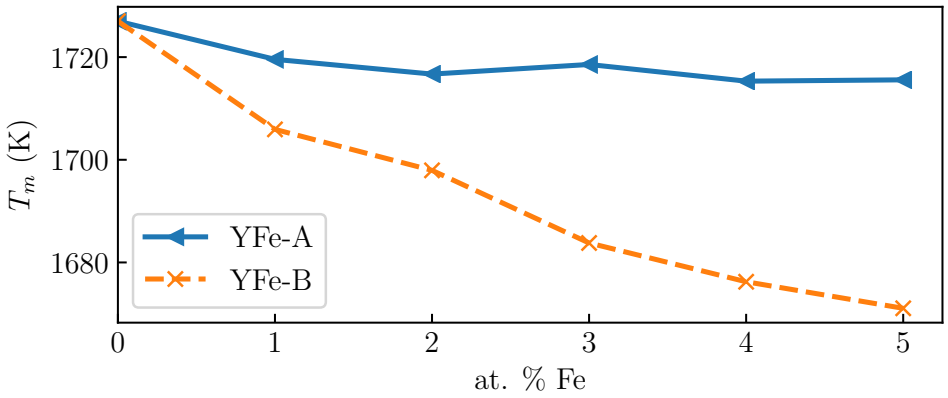

(b) Yttrium melting

Figure 5.2: Melting temperature of iron (a) and yttrium (b) as a function of melt composition for the potentials YFe-A and YFe-B.

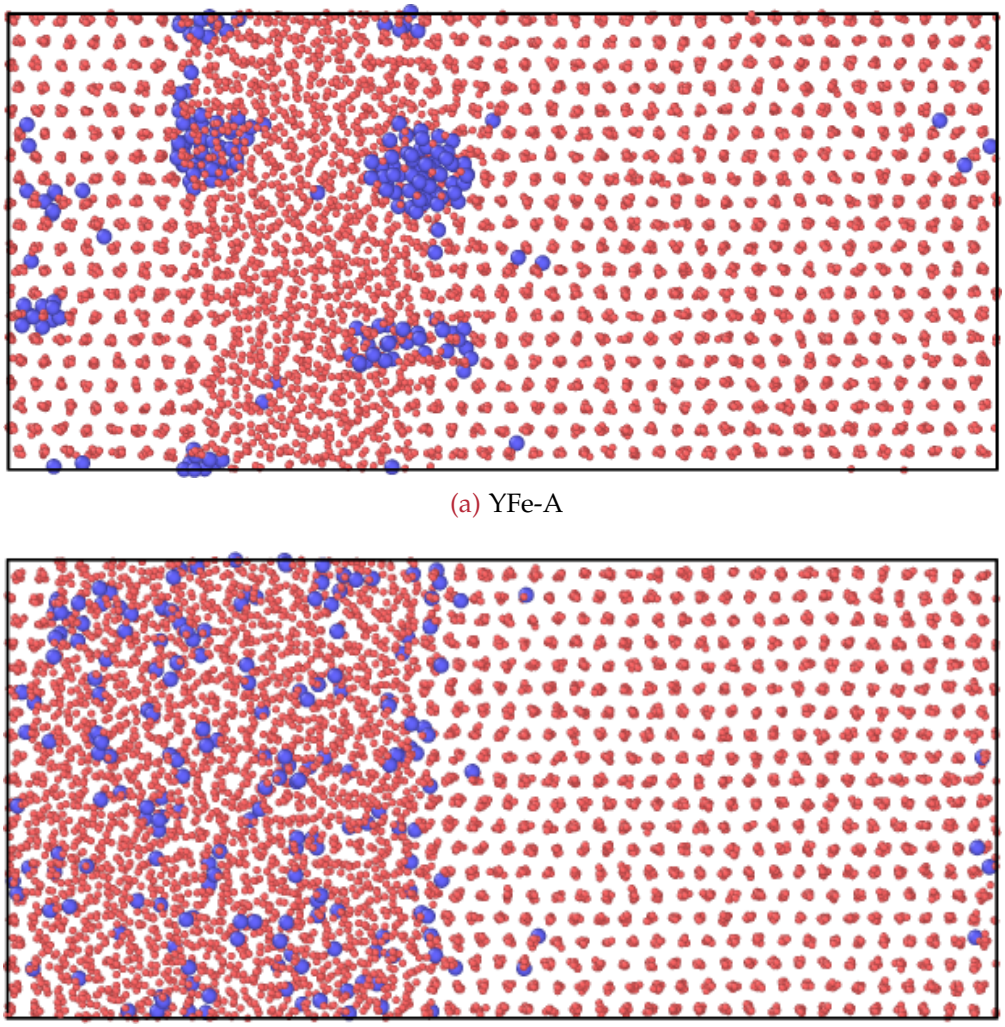

(a) YFe-A

(b) YFe-B

Figure 5.3: Crystallization of yttrium with 5 % iron in the yttrium melt after 1 ns at 1650 K. While the parameter set YFe-A leads to phase separation in iron and yttrium melt, using YFe-B results in a single liquid phase.

pinning of dislocations to yttrium atoms and in Section 7.2 the diffusion of yttrium inside of a dislocation is investigated.

5.4.1 *Segregation of substitutional yttrium*

A dipole consisting of two [111](110) edge dislocations in bcc-Fe was constructed using ASAP[158] and ASE.[159] The 3D periodic cell had dimensions of 248x142x21 Å and contained 63000 atoms. LAMMPS[84] was used to relax the cell and atom positions. Afterwards, an iron atom was replaced by a yttrium atom and the final energy E_i for position i was calculated as the energy after relaxing all atom positions. The binding energy E_b of the solute atom to the dislocation was calculated using

$$E_b = [E_{dis} + E_y] - [E_i + E_{super}], \tag{5.3}$$

Where E_{dis} is the energy of the dislocation dipole without the yttrium atom, E_y is the energy of the cell without dislocations but with one substitutional yttrium atom and E_{super} is the energy of the lattice without any defects. Figure 5.4a shows the binding energy as a function of position with respect to the dislocation core.

As a comparison the binding energy was also calculated using linear elasticity. The elastic constants of YFe-A are $c_{11} = 225\,\text{GPa}$, $c_{12} = 142\,\text{GPa}$ and $c_{44} = 126\,\text{GPa}$.[97] The stress field of an edge dislocation is described by[160]

$$\sigma_{ij} = \begin{bmatrix} \sigma_{xx} & \tau_{xy} & 0 \\ \tau_{xy} & \sigma_{yy} & 0 \\ 0 & 0 & \sigma_{zz} \end{bmatrix}, \tag{5.4}$$

with

$$\sigma_{xx} = -\frac{Gb}{2\pi(1-\nu)} \frac{y(3x^2+y^2)}{(x^2+y^2)^2} \tag{5.5}$$

$$\sigma_{yy} = \frac{Gb}{2\pi(1-\nu)} \frac{y(x^2-y^2)}{(x^2+y^2)^2} \tag{5.6}$$

$$\sigma_{zz} = \nu(\sigma_{xx} + \sigma_{yy}) \tag{5.7}$$

$$\tau_{xy} = \frac{Gb}{2\pi(1-\nu)} \frac{x(x^2-y^2)}{(x^2+y^2)^2} \tag{5.8}$$

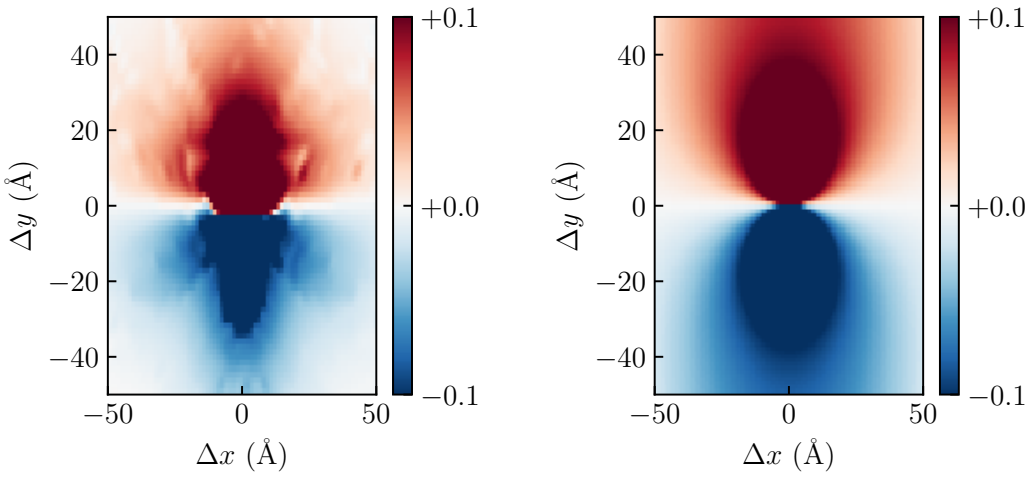

(a) Atomistic calculation

(b) Analytic calculation

Figure 5.4: Binding energy E^b (in eV) of a substitutional yttrium atom in the vicinity of an edge dislocation.

For isotropic materials Hooke's law can be used to calculate the resulting strain. The binding energy E_b of the point defect caused by the interaction between the strain field ϵ_{ij} can be calculated using:

$$E_b = -G_{ij}\epsilon_{ij}(x, y, z) \tag{5.9}$$

where G_{ij} are the components of the elastic dipole tensor which describes the elastic fields created by the point defect. The dipole tensor was calculated by inserting a yttrium atom in a perfect, stress-free crystal and calculating the stresses after relaxing the atom positions while keeping the simulation cell fixed. The induced stresses σ_{ij} are related to the elastic dipole tensor through

$$G_{ij} = V\sigma_{ij} \tag{5.10}$$

where V is the simulation cell volume. The elastic dipole tensor of a substitutional yttrium atom in bcc calculated using YFe-A is

$$G_{ij} = \begin{bmatrix} 14.9 & 0 & 0 \\ 0 & 14.9 & 0 \\ 0 & 0 & 14.9 \end{bmatrix} \text{eV}. \tag{5.11}$$

DFT calculations result in values of $G_{ii} = 17.4\,\text{eV}$. Figure 5.4b shows the analytically calculated binding energy using the elastic constants and dipole tensor of YFe-A. Both plots in Figure 5.4 show the same general features. The yttrium atom is bigger than the regular lattice atoms and therefore prefers to sit in the dilated region below the dislocation core. The binding energy close to the dislocation core shows significant differences. This is expected as the analytical solution is based on continuum mechanical assumptions that are not valid in the dislocation core due to the huge deformations. The atomistic calculation is not as symmetric as the analytic solution and shows a variation of the binding energy in some directions. This is caused by the anisotropy of the bcc lattice. The anisotropy ratio A is defined for cubic materials as

$$A = \frac{2c_{44}}{c_{11} - c_{12}} \tag{5.12}$$

and results in a value of $A = 3.04$ using the elastic constants of the potential. A perfectly isotropic material would have $A = 1$. The stress field of a dislocation and the stress strain conversion using Hooke's law used in the calculation of the analytic solution are only valid for isotropic materials which account for the differences between the analytic and the atomistic solution. Besides these differences, there is a significant agreement between the analytic solution and the atomistic calculation, which underlines the predictive power of the potential.

A closeup comparison of the analytic and the atomistic calculation is shown in Figure 5.5a, where the binding energies at a distance Δy of 10 Å above the dislocation core are plotted. Elasticity theory can not be used to calculate the binding energy between yttrium atom and dislocation in the dislocation core. Figure 5.5b shows the binding energy at different sites in the dislocation core. The potential predicts a maximum binding energy of 1.57 eV. Barnard *et al.*[50] calculated a value of 2.54 eV using DFT, but they used a [100](010) edge dislocation for its structural simplicity. Using the potential we can simulate far bigger systems which allows us to investigate [111](110) edge dislocations which are part of the predominant slip system of bcc-Fe. The calculations done here predict a segregation tendency of yttrium atoms towards edge dislocations and other regions of dilative stress.

5.4.2 *Pinning of dislocations by yttrium atoms*

The binding energy between solute yttrium atoms and an edge dislocation gives rise to a pinning effect on the mobility of dislocations. A 150x140x160 Å cell containing 290400 atoms and one edge dislocation was set up to investigate this effect.

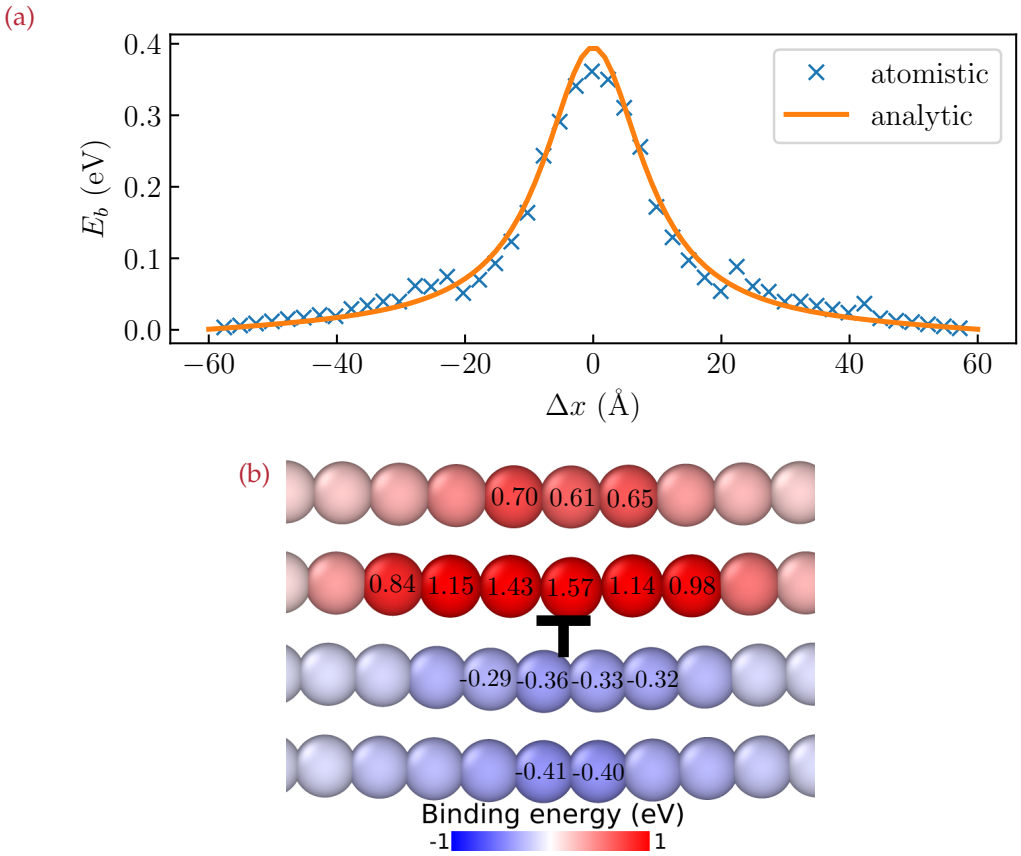

Figure 5.5: (a) Binding energy between an edge dislocation and a substitutional yttrium atom in a distance of $\Delta y = 10\,\text{Å}$ calculated using LAMMPS and elastic theory. (b) Closeup of yttrium-dislocation binding energies at different sites in the dislocation core.

The Burgers vector b of the dislocation was in $\frac{1}{2}\langle 111\rangle$ direction parallel to the x axis of the cell and dislocation direction was $\langle 1\bar{1}0\rangle$ parallel to the y axis of the cell. Cell boundaries were periodic in x and y direction and two yttrium atoms were placed in the glide plane of the dislocation. Atoms in two slabs with heights of 5 Å on the bottom and the top of the cell were fixed and the atoms in the top slab were shifted in steps of 0.05 Å in x direction.

The resulting shear stress and the movement of the dislocation line is shown in Figure 5.6. The constant Peierls stress of 0.282 GPa necessary for the movement of the dislocation in bulk Fe has been subtracted from the stress in the figure. Once the dislocation encounters the yttrium atoms the resulting stress decreases as the dislocation is attracted by the yttrium atoms. When the yttrium atoms are in the dislocation core, a significant increase in stress happens until the dislocation breaks free. The contribution of solid solution strengthening due to solute yttrium is probably still limited as the bulk of yttrium is bound in the precipitates once the precipitates are formed. Previous works on the strengthening mechanisms in ODS steels have neglected the solid solution strengthening due to yttrium atoms.[133,134]

5.5 CONCLUSION

We have derived a new bond-order potential for the iron-yttrium system, which allows for large scale atomistic simulations and is a step towards a potential for the complete ODS system. The potential has been fitted to pure yttrium phases, iron-yttrium mixed phases and point defects. The iron-iron interaction has been taken from literature. The yttrium-yttrium parameterization provides an accurate description of the elastic and thermal properties of yttrium and the correct vacancy formation energy in hcp yttrium. The formation energy of various interstitials is not perfect as this would require a bigger cut-off range which would lead to difficulties when fitting the yttrium-iron interaction. The ordering of the formation energies is, however, mostly correct which is sufficient for most applications. Two different version of the iron-yttrium parameterization were created in order to provide a satisfying representation of the iron-yttrium mixed phases as well as of the yttrium point defects in iron. YFe-A shows a complete representation of the point defect energies and interactions, including migration barriers, in the bcc-Fe matrix while YFe-B provides an accurate representation of iron-yttrium mixed phases.

The newly derived potential was used to investigate the interactions of point defects with edge dislocations in bcc-Fe. Calculation of the binding energy of substitutional yttrium to the dislocation shows a clear tendency of segregation to the

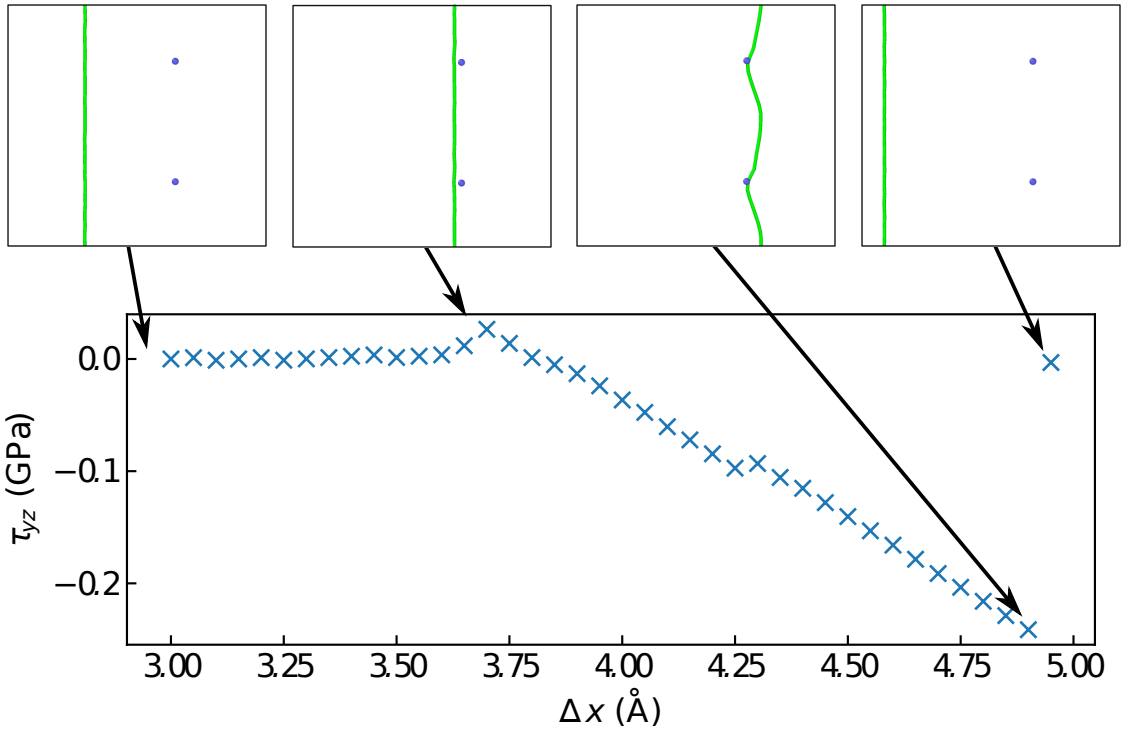

Figure 5.6: Pinning of an edge dislocation by two yttrium atoms in the glide plane. The dislocation is moved by shifting a slab of atoms at the top of the cell in 0.05 Å steps and the resulting shear stress is plotted against the displacement in the central diagram. A visualization of the dislocation movement is shown on the top. The dislocation in the top right image appears to be on the left of the yttrium atoms due to periodic boundary conditions.

tensile stress region of the dislocation. Comparison of the atomistic results to linear elasticity shows a qualitative agreement, but also the influence of the anisotropy of the iron lattice, which linear elasticity can not reproduce. Yttrium atoms in the elastic field of a dislocation lead to pinning of the dislocation. The solubility of yttrium atoms in iron is quite limited and most of the yttrium atoms are bound in the precipitates. Nevertheless, the effect of solid solution strengthening due to yttrium atoms on the mechanical properties of ODS steels should be further investigated.

Part III

YTTRIUM DIFFUSION

6 DISC - THE DIFFUSION SIMULATION CODE

Simulation of point defect migration in ODS steels requires long time scales due to the low jump rates involved. Within this work we developed DISC, a KMC code for diffusion simulations, which allows running simulations over billions of steps. The code has been published on GITLAB[161] and is introduced in this Chapter. Section 6.1 explains the structure and workflow of the program and Section 6.2 introduces the different analyzers used to extract data from the simulations throughout this thesis. In Chapter 7.1 DISC is used to investigate the diffusion of yttrium in bulk bcc Fe and in Chapter 8 for the diffusion of point defects in the presence of precipitates and their strain fields.

6.1 PROGRAM ARCHITECTURE

The architecture of DISC is designed to be modular and extensible, so it can be easily adapted to investigate different phenomena. Figure 6.1 shows an overview of the structure and workflow of the program. The heart of the program is the model class, which parses an input script and runs the simulation defined by the input script. The model creates the lattice, populates the lattice with defects, manages the analyzers and ties everything together.

Implemented lattice types are bcc and fcc, but the extension to other lattice types is easy due to the modular nature of the program. Every lattice consists of an array of sites and has periodic boundary conditions. These sites store an array of pointers to their neighbors, which avoids the necessity of determining the neighbors every time possible point defect jumps are collected. Events are primarily managed by the objects that are affected by the events. This means a vacancy will create a list of possible vacancy jump events to all nearest neighbors and an interstitial will create a list of all possible interstitial jumps. The rate of an event is calculated by the model as it may depend on additional external factors like the applied strain field. The list of events gets rebuilt only if the defect has moved in the previous step or another event has altered the neighborhood of the defect. This is a crucial feature for the simulations in Chapter 8 as hundreds or thousands of defects are

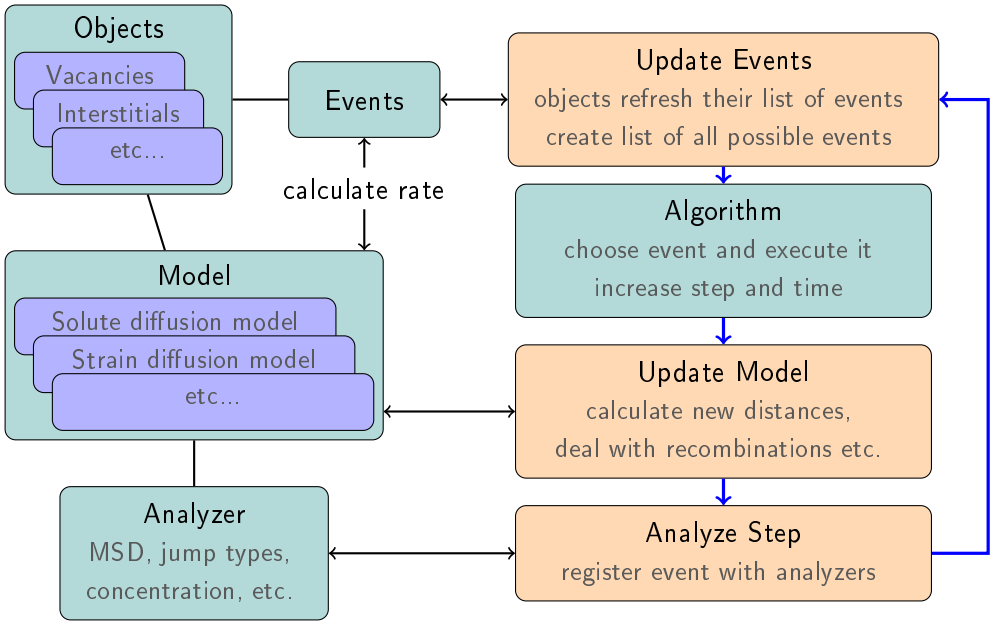

Figure 6.1: Structure and workflow of DISC.

present in this case and creating the complete list of events from scratch would be far to expensive.

Once the event list of every object is up to date, the model collects a list of all possible events and passes this list to the KMC algorithm, which was already introduced in Section 2.4. The algorithm chooses one of the events with a probability proportional to the rate of the event, executes the event and increases the time and the step counter accordingly. After the chosen event was executed, the state of the model is updated. This can include either the calculation of the new vacancy-solute distances or recombinations of interstitials and vacancies depending on the type of model. The last part of every step is the analysis of the situation. Every active analyzer registers the situation and stores the relevant properties. The available analyzers depend on the model and are explained in the Section 6.2. Once the analysis is completed the next step starts with updating the event lists of every object.

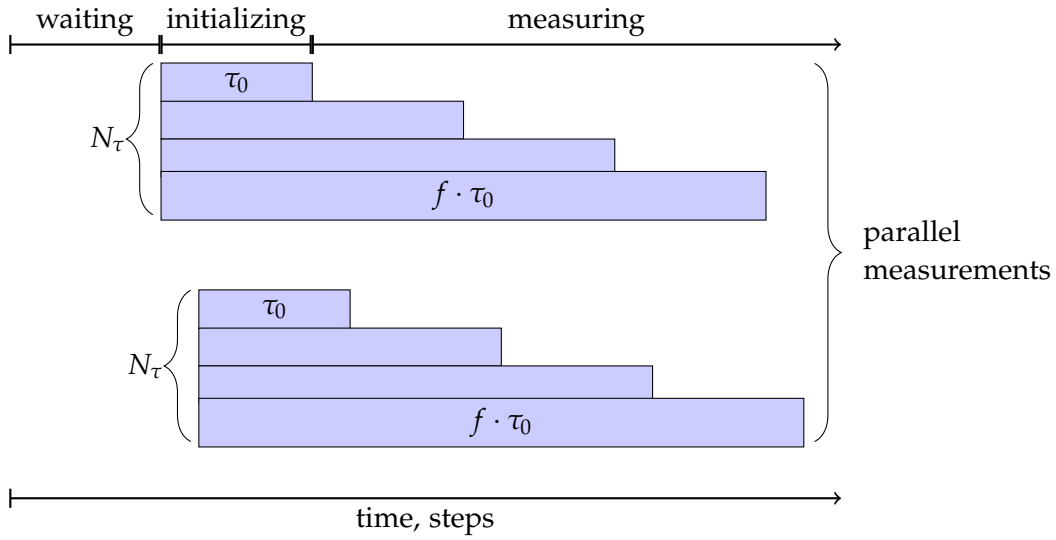

Figure 6.2: Schematic of the measurement scheme of the MSD analyzer of DISC.

6.2 ANALYZERS

6.2.1 *Mean-squared displacement*

This analyzer calculates the mean-squared displacement (MSD) from the movement of one or multiple defects or atoms. Every passage of the monitored particles through the periodic boundary is registered. This later allows the calculation of the unwrapped position of the particles which gets rid of the confinement to the size of the simulation box. The MSD is calculated from the initial unwrapped position $\vec{R}_n(0)$ and the unwrapped position after an interval τ according to:

$$\langle r^2(\tau) \rangle = \lim_{N \to \infty} \frac{1}{N} \cdot \sum_{n=1}^{N} \left(\vec{R}_n(\tau) - \vec{R}_n(0) \right)^2 \tag{6.1}$$

Simulations at different temperatures would lead to a significantly different numbers of steps in the same time interval τ, due to the exponential change of rates with temperature. Constant values of τ for wide temperature ranges would therefore lead to insufficient steps for proper statistics at high temperatures. This problem was solved by the scheme depicted in Figure 6.2. The analyzer starts with a waiting phase for a certain number of steps N_{steps}. Once this waiting phase is over the passed time is used as the smallest time interval τ_0. The longest time interval $f \cdot \tau_0$

is defined by scaling τ_0 with a factor f. At equal distances between these two values additional intervals are added until the total number of intervals N_τ is reached. To further improve the number of samples, multiple parallel measurements can be run on the same simulation. This is done by shifting the start of the measurement as shown in Figure 6.2.

During the initialization phase, the unwrapped initial positions of every interval are determined and stored. The initialization phase ends with the first time interval τ_0. During the measurement phase, the squared distance between initial and final position is calculated and the final position is stored as initial position for the next interval. The MSD analyzer is available in every model. It measures either the MSD of vacancies or lattice atoms in the lattice or strain models or of solute atoms or yttrium atoms in the yttrium and the solute diffusion models used in Chapter 7.1.

6.2.2 *Vacancy position*

This analyzer records the number of times a vacancy is in a certain neighbor shell of a solute atom and the total time it spends there. Figure 7.2 shows the different vacancy positions with respect to a substitutional solute atom. It is used to investigate the diffusion mechanism of yttrium in bcc Fe in Chapter 7.1.

6.2.3 *Jump count*

This analyzer records the number of times a certain jump occurs. Jumps are categorized by their initial and final distance to the solute atom as shown in Figure 7.2. It is also used to investigate the diffusion mechanism of yttrium in bcc Fe in Chapter 7.1.

6.2.4 *Point defect concentration*

The point defect concentration analyzer is used to calculate the average concentration of vacancies and interstitials in the system. It can be used to measure steady-state concentrations as well as concentration changes with time. Input parameters are the amount of steps skipped at the beginning of the simulations and the length of one measurement interval. The analyzer was used in Chapter 8 to determine point defect concentrations under irradiation.

6.2.5 *Spheric concentration*

The spheric concentration analyzer separates the simulation cell in subdomains and allows the calculation of concentration in these subdomains. Subdomains are defined by providing the coordinates of the center and the number of shells the simulation cell is divided in. In each subdomain, the analyzer works similar to the point defect concentration analyzer introduced in the previous section. It measures vacancy as well as interstitial concentrations and was used in Chapter 8 to determine point defect concentrations as a function of distance from the precipitate.

6.3 COUPLING TO EXTERNAL ELASTIC FIELDS

Using DISC it is possible to include the influence of external elastic fields on KMC diffusion simulations. Elastic fields can be calculated analytically in DISC or imported from separate finite element method (FEM) calculations. The physics behind the interaction between elastic strain fields and point defect migration are explained in Section 8.2.1. This section focuses on the implementation in DISC. For performance reasons, the interaction energies between point defects and the strain field at every possible point are calculated and stored prior to starting the KMC simulations.

The analytic calculation of the strain field is explained in Section 8.2.3. To determine the strain field at an arbitrary point, the coordinates of the point are transformed to spherical coordinates before the strain tensor is calculated. Afterwards the strain tensor is transformed from spherical back to cartesian coordinates.

Elastic strain fields can also be computed externally using Finite Element software as FEAP[162] and get imported in DISC using the *vtk* format. DISC expects 4-node or 10-node tetrahedrons in an unordered grid as elements of the FEM calculation. Support for other formats or grid types was not necessary yet, but should be trivial to implement. Calculating the elastic strain at an arbitrary point in space requires determining the element that contains this point. A brute-force search over potentially millions of elements is extremely time consuming, therefore DISC stores the elements in an octree.[163] An octree is a data structure that partitions the space by recursively dividing it into eight octants. This significantly reduces the number of expensive point-in-tetrahedron checks necessary to find the tetrahedron that contains the point of interest. After finding the element that contains the point, the solution between the nodes is interpolated using the shape function of the element.

7

YTTRIUM DIFFUSION

As detailed in Section 1.2.3 and Section 1.2.4, diffusion of yttrium is of crucial importance for the formation and growth of oxide precipitates. We investigated the bulk diffusion of yttrium in bcc-Iron in Section 7.1 by using DFT calculated migration barriers as input for the KMC code presented in the previous chapter. Some precipitation growth models indicated that pipe diffusion could be an important mechanism. The potential developed in Chapter 5 was used to calculate migration barriers of vacancy jumps inside of an edge dislocation core. These results are presented in Section 7.2.

7.1 BULK DIFFUSION

Results in this section were first published in Ref. [157].

There is an exceptionally high binding energy between a substitutional yttrium atom and a vacancy due to the considerably bigger size of the yttrium atom.[52] An yttrium atom with a vacancy in a nearest neighbor position relaxes from it's lattice position towards the vacancy.[39] The resulting configuration can be either considered as a yttrium-vacancy pair or as an interstitial yttrium atom in between two vacancies. Figure 1.3 illustrates this interesting feature. As a result of this, the barrier for the yttrium-vacancy exchange is negligible[51,52] or not present at all[53] and not relevant for the diffusion mechanism. This raises the question of how the yttrium diffusion actually happens. Does the diffusion of yttrium require the separation of the yttrium-vacancy pair, which consumes a considerable amount of energy, or is there an other mechanism?

Due to their influence on radiation resistance of steel and the growth of precipitates the diffusion of solutes in bcc-Fe has been the objective of several computational studies.[164,165] The diffusion of yttrium is the limiting factor for the formation and growth of yttrium containing oxide particles in ODS steel.[19,47] It has been investigated by Murali *et al.*[51] and Gao *et al.*[52] using DFT and Le Claire's nine frequency model, as well as by Bocquet*et al.*[53] who used an analytical model. Considering all these groups calculated a considerably lower activation energy for diffusion than Hin *et al.*, where a precipitation growth model was fitted to experimental data,[48]

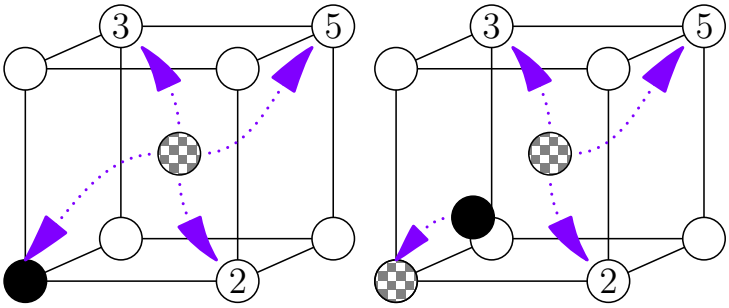

(a) (b)

Figure 7.1: Schematic of the diffusion mechanisms. In (a) the 'classical' vacancy mechanisms is shown with substitutional atom and vacancies on the lattice positions. The vacancy can either jump to a second, third or the fifth nearest neighbor position or it can change place with the solute atom. The 'interstitial' mechanism is shown in (b). Both of the vacancies can jump to second, third or fifth nearest neighbor positions which will push the solute atom to the position of the other vacancy.

possible explanations could be, that Le Claire's model breaks down for highly correlated jumps or the restriction of the yttrium-vacancy interaction to the second nearest neighbor shell is to narrow.

Thus, in this chapter, the diffusion of yttrium in iron was simulated using the KMC code presented in Chapter 6. This allows to investigate the diffusion without any assumptions as all correlation effects are automatically considered in KMC simulations. Both possible diffusion mechanisms were investigated: The 'classical' vacancy mechanism that is the basis of Le Claire's model and the 'interstitial' mechanism that considers jumps to and from the interstitial position between two vacancies as the relevant jumps. The 'interstitial' mechanism was also the basis for the analytic model by Bocquet *et al.*[53] Figure 7.1 shows the two mechanisms. The rates of possible diffusion events were determined from migration barriers calculated by DFT calculations as shown in 7.1.2. The KMC simulations presented in 7.1.3 and discussed in 7.1.5 shed light on the diffusion mechanism and allow to calculate the diffusivity of yttrium which can be compared to the value calculated using Le Claire's nine frequency model.

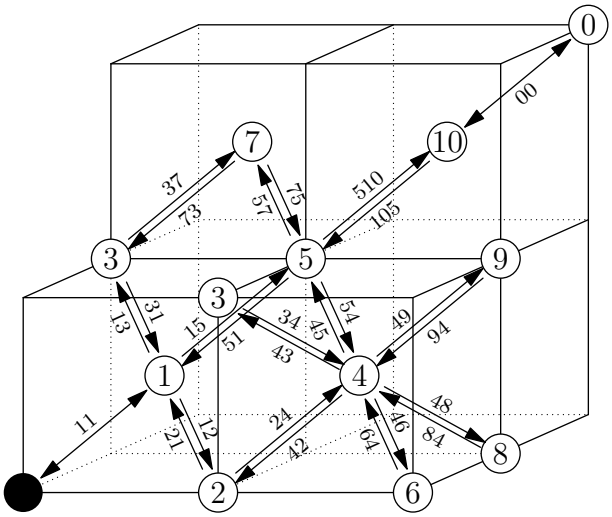

Figure 7.2: Positions and Fe-Vacancy jumps considered in the 5NN model used in this work. The location of the yttrium atom is represented by the black circle, the first nearest neighbor position is labeled position 1, second nearest neighbor position is labeled as position 2 and so on. A vacancy jumpy from position 1 to position 2 is called a 12 jump, a jump in the reversed direction is called a 21 jump. Positions farther away from the yttrium than tenth-nearest neighbor are labeled as 0 and jumps between these positions that are unaffected by the presence of the yttrium atom are labeled as 00 jumps.

7.1.1 *Methodology*

7.1.1.1 *Vacancy jump rates*

The Vienna Ab initio Simulation Package[71–74] (VASP) was used to determine the migration barriers. The calculations were performed in a plane wave basis set with pseudopotentials from the VASP library based on the projector augmented-wave (PAW) method[139,140] and within the generalized-gradient approximation (GGA) in the Perdew-Burke-Ernzerhof (PBE) parameterization.[70] The Brillouin zone sampling was done on a 3x3x3 k-point grid and the plane wave energy cut-off was set to 500 eV. The convergence criterion for the relaxations was achieved when all forces were less than 1 meV $Å^{-1}$. All 127 atom positions in the 4x4x4 supercell were fully relaxed. The climbing image nudged elastic band method[141] was employed to determine the minimum energy path from one vacancy position to the next.

The binding energy E_i^b between yttrium atom and vacancy in position i was calculated by

$$E_i^b = [E_v + E_{sub}] - [E_i + E_{super}], \tag{7.1}$$

where E_v is the energy of a supercell containing a vacancy, E_{sub} is the energy of a supercell containing a substitutional yttrium atom, E_i is the energy of the supercell with yttrium atom and vacancy in position i and E_{super} is the energy of a bcc-Fe supercell without defects.

Figure 7.2 shows the different vacancy jumps that were considered in this work. The rates of these jumps were calculated from the migration barriers E_{ij}^{mig} according to:

$$\omega_{ij} = \nu_{ij} \cdot \exp\left(-\frac{E_{ij}^{mig}}{k_B T}\right). \tag{7.2}$$

The attempt frequency ν_{ij} is assumed to be the same for all types of jumps and has a value of $\nu = 6\,\mathrm{THz}$ which is on the same order of magnitude as the Debye frequency of iron.[164] The diffusivity was calculated from these jump rates using two different methods. Le Claire's nine frequency model provides an analytic formula to calculate the correlation factor and the diffusivity and is introduced in Section 7.1.1.2. The yttrium-vacancy interaction in this model is, however, limited to the second nearest neighbor shell and it does not provide any information on the diffusion mechanism. Therefore, it was mainly used to confirm the results of the KMC simulations and compare to the results of Murali *et al.*.[51] The kinetic Monte Carlo simulation introduced in Section 7.1.1.3 allows an arbitrary cut-off for the yttrium-vacancy interaction and determination of the diffusion paths.

7.1.1.2 *Le Claire's model*

Le Claire's nine frequency model[166,167] is used to calculate the diffusivity of a solute atom including correlation effects. The solute diffusion coefficient D_s is given by

$$D_s = a^2 \omega_{11} f_2 \frac{\omega_{31}}{\omega_{13}} c_V^{eq}, \tag{7.3}$$

where a is the lattice constant, ω_{ij} the respective rate for a jump $i \rightarrow j$ and c_V^{eq} the equilibrium vacancy concentration obtained from the relation:

$$c_V^{eq} = \exp\left(-\frac{E_V^f}{kT}\right). \tag{7.4}$$

A vacancy formation energy E_V^f of 2.01 eV[51] was used in this work, which is in good agreement to experimental results.[58] The solute correlation factor f_2 is given by

$$f_2 = \frac{1 + t_1}{1 - t_1}, \tag{7.5}$$

with

$$t_1 = \frac{\omega_{11}}{\omega_{11} + 3\omega_{12} + 3\omega_{13} + \omega_{15} - \dfrac{\omega_{12}\omega_{21}}{\omega_{21} + F\omega_{24}} - \dfrac{\omega_{13}\omega_{31}}{\omega_{31} + 3F\omega_{00}} - \dfrac{\omega_{15}\omega_{51}}{\omega_{51} + 7F\omega_{00}}}, \tag{7.6}$$

where $F = 0.512$ is the fraction of vacancies dissociating from a neighbor site of the solute atom, that are permanently leaving the neighborhood of the solute atom.

7.1.1.3 *Kinetic Monte Carlo*

Kinetic Monte Carlo simulations[89] not only allow to determine the diffusivity of a solute atom but also to investigate the diffusion path. The simulations always contained one vacancy and one yttrium atom and were run with periodic boundary conditions. Therefore, there is no yttrium-yttrium or vacancy-vacancy interaction. The temperature was varied in 25 steps from 1000 to 10 000 K and 1×10^9 steps were simulated. The yttrium concentration can be controlled by changing the size of the simulation cell. This leads to an overestimation of the vacancy concentration, which was considered by rescaling the physical time according to,[168,169]

$$t = t^{MC} \cdot \frac{c_V^{MC}}{c_V^{real}}, \tag{7.7}$$

where c_V^{MC} is the vacancy concentration in the simulation (1/number of lattice sites) and c_V^{real} is the true equilibrium vacancy concentration.

As a first approximation one could assume, that the vacancy concentration is the same as the equilibrium vacancy concentration in pure iron calculated from equation (7.4). This would be a valid simplification for solutes with a low binding energy to vacancies or for high temperatures. Solutes with a non negligible binding energy to vacancies, however, provide additional sites, where the formation of a vacancy is much easier than in the perfect iron lattice. The resulting vacancy concentration is therefore higher and can be calculated from this relation:[170]

$$c_V^{real} = \left(1 - zc_s + zc_s \exp\left(-\frac{E_b}{kT}\right)\right) \exp\left(-\frac{E_V^f}{kT}\right). \tag{7.8}$$

Table 7.1: Yttrium-vacancy binding energies as a function of distance compared to results from literature.

position	E^b (eV)	Literature (eV)
1	1.26	1.45[a], 1.20[b], 1.27[c], 0.69[d]
2	0.27	0.26[a], 0.09[b], 0.20[c]
3	0.17	0.24[a], 0.14[b], 0.13[c]
4	0.08	0.15[a], 0.01[b], 0.04[c]
5	0.22	0.25[a], 0.23[b], 0.20[c]
6	0.09	
7	0.05	
8	0.06	
9	0.05	
10	0.04	

[a] Ref. [51] [b] Ref. [53] [c] Ref. [39]
[d] Ref. [52]

Here, z is the number of nearest neighbors (8 in bcc) and c_s is the solute concentration. This equation includes the nearest neighbor binding energy between vacancy and solute atom, but neglects the binding energies at higher distances. Yttrium has a considerable binding energy with vacancy atoms, therefore equation (7.8) was used to calculate the real vacancy concentration. The diffusivity of yttrium was calculated from the mean-squared displacement of the yttrium atom:

$$\langle r^2(\tau)\rangle = 6D\tau. \tag{7.9}$$

The mean-squared displacement was determined by monitoring the position of the yttrium atom as a function of time:

$$\langle r^2(\tau)\rangle = \lim_{T\to\infty} \frac{1}{T} \cdot \int_0^T \left(\vec{R}(t+\tau) - \vec{R}(t)\right)^2 \mathrm{d}t \tag{7.10}$$

7.1.2 *Ab initio calculations*

To limit the amount of barriers that have to be calculated the yttrium vacancy interaction needs to be cut-off at a certain distance. The *ab initio* calculations presented

Table 7.2: Diffusion barriers calculated with VASP compared to results from literature. Jumps are labeled according to the scheme shown in Figure 7.2.

jump	E^{mig} (eV)	Literature (eV)	jump	E^{mig} (eV)	Lit (eV)
00	0.68	0.65[a], 0.69[b]	11	0.01	0.03[a], 0.09[d]
12	1.94	2.05[a], 2.00[b], 1.81[d]	21	0.95	0.92[a], 0.89[b], 0.91[d]
13	1.24	1.33[a], 1.22[b], 0.93[d]	31	0.15 | 0.20[d]	0.18[a], 0.16[b], 0.04[d]
15	1.05	1.15[a], 1.02[b], 0.86[d]	51	0.01	0.02[a], 0.05[b], 0.12[d]
24	0.72	0.75[a], 0.69[b], 0.69[d]	42	0.53 | 0.67[d]	0.66[a], 0.61[b], 0.69[d]
34	0.78	0.79[b]	43	0.69	0.66[b]
37	0.69	0.83[b]	73	0.58 | 0.53[e]	0.69[b]
45	0.69	0.69[b]	54	0.83	0.91[b]
46	0.70	0.70[b]	64	0.71 | 0.62[e]	0.69[b]
48	0.68	0.70[b]	84	0.67 | 0.61[e]	0.69[b]
49	0.69	0.70[b]	94	0.66 | 0.61[e]	0.69[b]
57	0.72	0.91[b]	75	0.56 | 0.51[e]	0.69[b]
510	0.79	0.91[b]	105	0.61 | 0.57[e]	0.69[b]

[a] Ref. [51] [b] Ref. [53] [c] Ref. [52]
[d] Adjusted for 2NN model [e] Adjusted for 5NN model

in Table 7.1 show, that there is still a considerable binding even at fifth-nearest neighbor distance. This can be explained by the size difference between the iron and yttrium atoms. The bigger yttrium atom distorts the bcc-Fe lattice. This effect is most pronounced in the closed-packed $\langle 111 \rangle$ direction, which explains the high binding energy to a vacancy in that direction. We used two different models in this work. The fifth-nearest neighbor model (5NN) includes all jumps to and from positions up to the fifth-nearest neighbor distance. Figure 7.2 shows the jumps considered in the 5NN model and the calculated migration barriers are presented in Table 7.2. The second-nearest neighbor model only includes jumps to and from positions up to the second-nearest neighbor distance. This neglects the considerable interaction between yttrium atom and vacancy at third- and fifth-nearest neighbor distance. It is, however, the approximation made in the derivation of Le Claire's nine frequency model[166,167] and was used to compare the KMC results with Le Claire's model. One has to keep in mind, that the DFT calculations were done on a 4x4x4 supercell. Therefore, the binding energies and migration barriers concerning large distances may be influenced by interactions with images. The diffusion of yttrium in iron is, however, governed by the yttrium-vacancy interaction up to the fifth-nearest neighbor shell. Thus small errors in the distant binding energies and migration barriers will not influence the diffusion significantly.

In the 5NN model the yttrium-vacancy interaction is limited to the fifth-nearest neighbor shell, which means the binding energies $E_i^b = 0$ for $i > 5$. This requires a manipulation of the jump frequencies calculated via DFT in order to fulfill detailed balance. The ratio of the jump rates for forward jumps ω_{ij} and backward jumps ω_{ji} is connected to the difference in binding energy according to[164]

$$\frac{\omega_{ij}}{\omega_{ji}} = \exp\left(\frac{E_j^b - E_i^b}{k_B T}\right), \tag{7.11}$$

which is equivalent to

$$E_i^b - E_j^b = E_{ij}^{mig} - E_{ji}^{mig}. \tag{7.12}$$

The straightforward way is to keep the saddle-point and binding energies inside of the cutoff range constant and decrease the migration barrier E_{ji}^{mig} for jumps from outside of the cutoff j to the inside i by the binding energy E_j^b. Figure 7.3 (a) shows the DFT calculated and the resulting corrected energy landscape. The barrier for the jump from sixth- to fourth-nearest neighbor distance $E_{64}^{mig} = 0.71\,\text{eV}$ was reduced

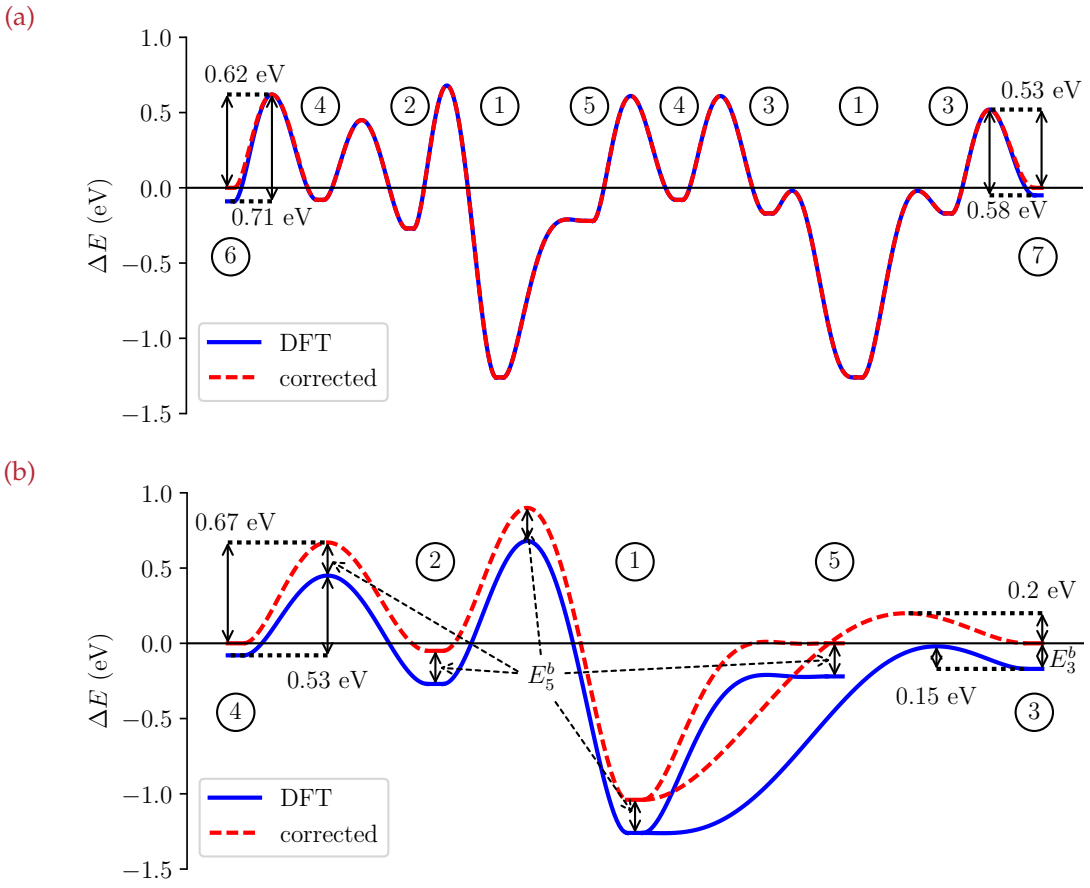

Figure 7.3: Energy barriers in 5NN model (a) and 2NN model (b). Circled numbers mark the neighbor shells of the yttrium atom. The curves drawn in blue show the original DFT values which include the binding energy outside of the respective cutoff range. The red curves show the energy landscape after removing the binding energy outside of the cutoff and adjusting the barriers to fulfill detailed balance. All barriers heights except of the marked ones are identical to the values in Table 7.2.

by the binding energy $E_6^b = 0.09\,\text{eV}$ to $E_{64}^{mig} = 0.62\,\text{eV}$. All other barriers for jumps from outside the cutoff to the inside were treated accordingly.

The straightforward way is not possible for the 2NN model. Here, all binding energies $E_i^b = 0$ for $i > 2$. The binding energies E_3^b and E_5^b are bigger than the respective migration barriers E_{31}^{mig} and E_{51}^{mig}, which would lead to negative migration energies E_{ji}^{mig}. Adjusting the saddle point energies to keep these migration energies positive would lead to changes in E_{15}^{mig} and E_{13}^{mig}. These barriers however, are critical for the diffusion mechanism and should not be changed. The best solution for this problem is to increase all binding energies and saddle point energies within the cutoff by E_5^b. This keeps all the migration barriers inside the cutoff constant and only leads to a small adjustment of E_{31}^{mig} and E_{42}^{mig}. This procedure should limit the influence of cutting the interaction between yttrium and vacancy at 2NN distance on the kinetics of the yttrium diffusion. Figure 7.3 shows the resulting energy landscape. The barriers obtained from DFT calculations as well as the adjusted values fulfilling detailed balance for both the 5NN as well as the 2NN model are presented in Table 7.2.

7.1.3 *Diffusion coefficient of Yttrium*

Using the migration barriers determined in the previous section in a KMC simulation allows the calculation of the diffusivity of yttrium. The two different diffusion mechanisms shown in Figure 7.1 were considered for the KMC calculations. For the 'classic' mechanism the extremely low barrier for the 11 jump was increased to 0.65 eV to increase the statistics for the other possible jumps. Calculations using Le Claire's Model as well as KMC simulations show no influence of the 11 barrier height on the diffusion as long as it is significantly lower than the barriers of the other possible jumps. The 'interstitial' mechanisms does not include 11 jumps, therefore no modification of E_{11}^{mig} is necessary. Figure 7.4 shows the diffusivity of yttrium using the 'classic' mechanism in the 5NN model as a function of temperature compared to the results of Bocquet *et al.*,[53] Murali *et al.*[51] and Hin *et al.*.[48] The diffusivity follows an Arrhenius equation with:

$$D = D_0 \exp\left(-\frac{Q}{k_B T}\right). \tag{7.13}$$

Table 7.3 summarizes the resulting activation energy Q and prefactor D_0. The 'classic' as well as the 'interstitial' mechanism show a nearly identical activation energy,

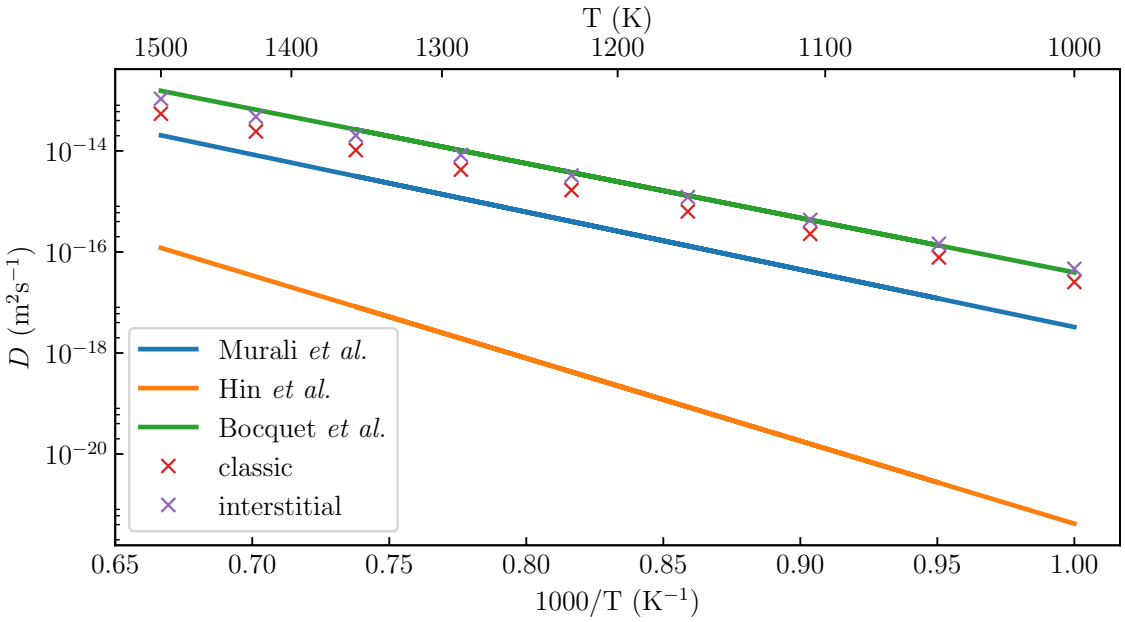

Figure 7.4: Diffusivity of yttrium as a function of temperature calculated with KMC in the 5NN model using the 'classic' mechanism compared to the results of Murali *et al.*[51] and Hin *et al.*[48]

Table 7.3: Activation energy Q and prefactor D_0 for the diffusion of yttrium in bcc-Fe calculated using different models.

	Q (eV)	D_0 ($m^2\,s^{-1}$)
Le Claire	2.24	3.7×10^{-7}
2NN 'classic'	2.23	3.5×10^{-7}
2NN 'interstitial'	2.24	6.9×10^{-7}
5NN 'classic '	1.98	2.5×10^{-7}
5NN 'interstitial'	2.00	5.7×10^{-7}
Murali[51]	2.26	8.0×10^{-7}
Bocquet[53]	2.14	2.4×10^{-6}
Hin[48]	3.25	1.0×10^{-5}

but the prefactor of the 'interstitial' mechanism is roughly twice the value of the 'classic' model. This is not related to the modification of E_{11}^{mig} as can be seen by the fact, that the 2NN 'classic' model with the modified E_{11}^{mig} and Le Claire's model with the original E_{11}^{mig} lead to virtually identical results. Also, a variation of E_{11}^{mig} from 0.6 to 1.0 eV shows no influence of the barrier height on the prefactor or the activation energy. Increasing the range of yttrium-vacancy interaction to the 5NN shell reduces the activation energy by 0.24 eV. This decrease is closely related to the yttrium-vacancy binding energy $E_5^b = 0.22\,\text{eV}$.

7.1.4 *Mechanism of Yttrium diffusion*

The kinetic Monte Carlo simulation not only allows to calculate the diffusivity but also allows monitoring the diffusion process and thereby investigating the diffusion path. Figure 7.5 shows how many jumps of a certain type occur per second for a simulation in the 5NN model at 1000 K. The simulation was done for cell sizes from 5x5x5 to 10x10x10, which leads to a variation in yttrium concentration. The most common jump is the 11 jump, which has by far the lowest migration barrier. The 11 jump, however, does not contribute to the diffusion of the yttrium atom.

Another frequently occurring jump is the unbound oo jump. These are all jumps that occur far away from the yttrium atom. The number of these jumps increases with decreasing yttrium concentration as this leads to a larger volume of undis-

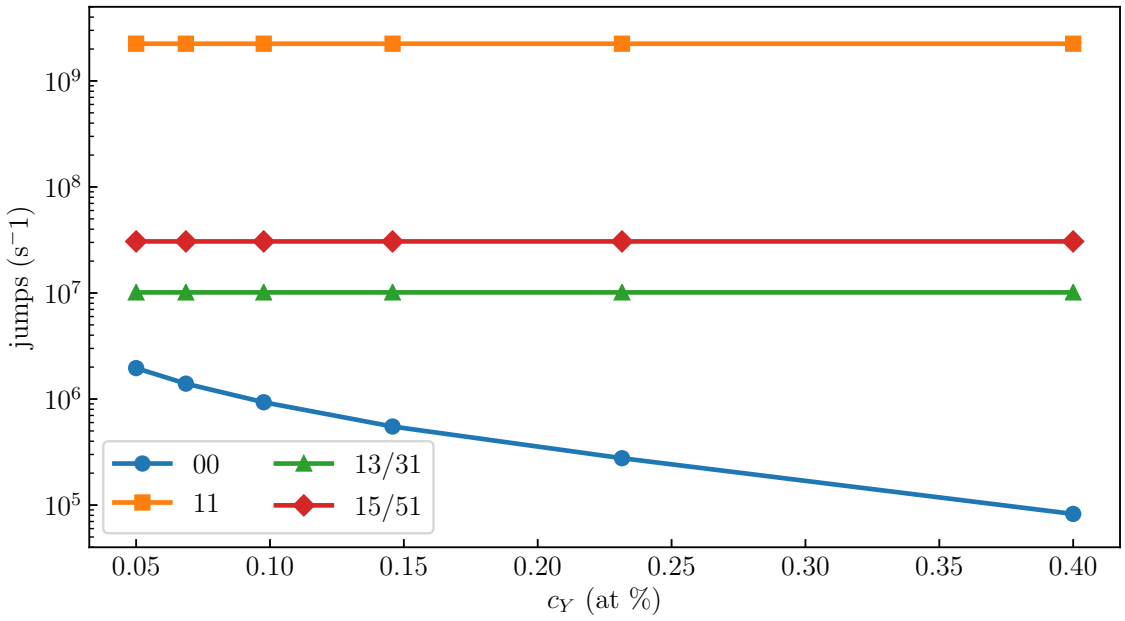

Figure 7.5: Jumps per second as a function of yttrium concentration at 1000 K. The simulation was in the 5NN model using the 'classic' mechanism. The number of 15 jumps is nearly identical to the number of 51 jumps. The same applies to 13 and 31 jumps.

turbed bcc-Fe lattice that needs to be traversed once the yttrium vacancy pair has been separated.

Other common kind of jumps are 15 and 13 jumps and their respective reverse jumps 51 and 31. The number of jumps and reverse jumps is nearly identical. This is caused by the very low barrier of the reverse jumps. Once the vacancy has been separated from the yttrium atom, it rapidly recombines in most of the cases. Separation to position 5 and the subsequent recombination does not contribute to the yttrium diffusion as there is only the one previous position to go back to. This means nearly all of the 15 jumps are neutralized by the following 51 jump with no change to the overall situation.

The situation is different for the 13 and 31 jumps. Once yttrium atom and vacancy have separated to the third nearest neighbor position, there are two different nearest neighbor positions to go back to. Recombination to the other than the previous position leads to an effective movement of the yttrium atom. The vacancy stays connected to the yttrium atom and drags it through the lattice. The sequence of jumps leading to yttrium diffusion is shown in Figure 7.6. It leads to a diffusion of yttrium through the bcc-Fe lattice without splitting the yttrium-vacancy pair. This way of moving the solute atom works in the 'interstitial' as well as in the 'classic' diffusion mechanism. It only requires a sufficiently fast solute-vacancy exchange in the 'classic' mechanism after every sequence of 13-31 jumps. This means it is not limited to the special case of yttrium with its massive relaxation to the interstitial position but can happen for other substitutional solutes as well.

7.1.5 *Discussion*

The diffusivity of yttrium in bcc-Fe was calculated using KMC simulations and Le Claire's nine frequency method using migration barriers obtained from DFT calculations. As shown in Table 7.3 the calculated activation energy for diffusion is similar using both methods. This shows that the nine frequency model is suitable for dealing even with highly correlated jumps like yttrium diffusion. It is, however, limited to the 2NN neighbor shell, which leads to differences in cases like yttrium in iron, where there is a considerable yttrium-vacancy interaction in more distant shells. This results in an overestimation of the activation energy of 0.24 eV.

KMC simulations were run using two different mechanisms. Both mechanisms show virtually identical activation energies. The activation energy only depends on

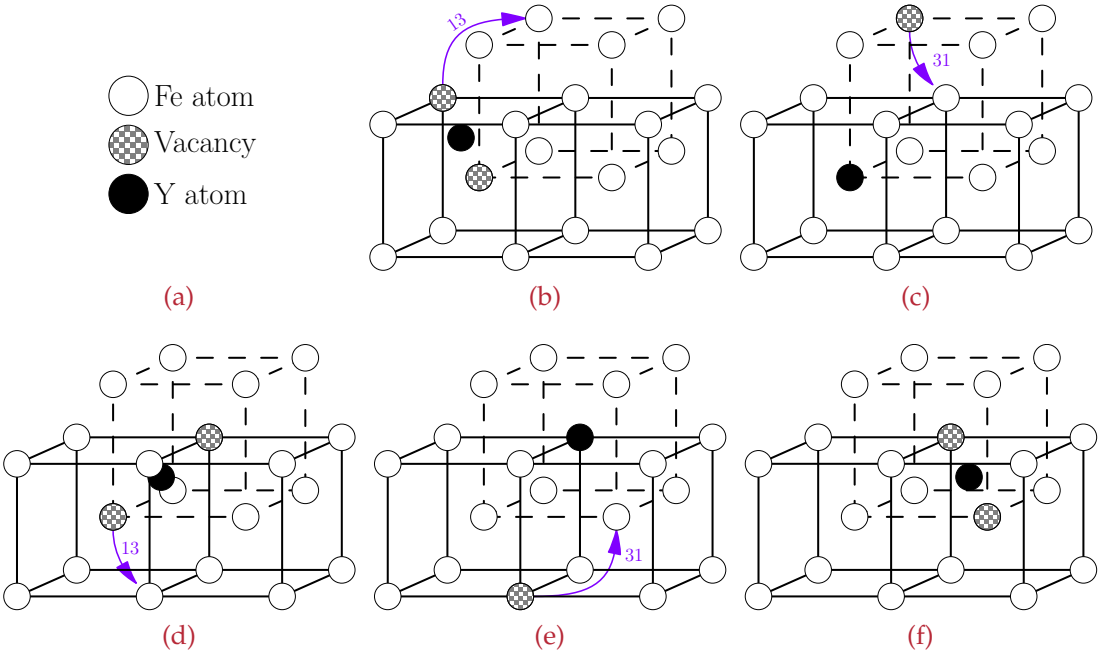

Figure 7.6: Yttrium diffusion in bcc-Iron using 13/31 jumps in the 'interstitial' mechanism. The 'classic' mechanism works in the same way but requires a rapid 11 jump between (c) and (d). (a) Yttrium atom in nearest neighbor position to vacancy. (b) After 13 jump the vacancy is in third nearest neighbor position to the yttrium atom. (c) After a 31 jump the vacancy is again in nearest neighbor position to the yttrium atom, but the position is different from (a). (d) The next 13 jump splits the yttrium-vacancy pair again. (e) Yttrium-vacancy pair recombines via 31 jump. Same situation as (a), only shifted by one lattice vector.

the vacancy formation energy, yttrium-vacancy binding energy and the migration barrier of the 13 jump:

$$Q \approx E_V^f + E_{13}^{mig} - E_1^b \tag{7.14}$$

This shows, that the 13 jump is the relevant jump regardless of the diffusion mechanism. The prefactor for the 'interstitial' mechanism however, is roughly twice the value of the 'classic' mechanism. A vacancy in the nearest neighbor position to a solute atom can jump to 8 different positions in the 'classic' mechanism (1×11 jump, 3×12 jump, 3×13 jump , 1×15 jump) while it has 14 possible jump targets (6×12 jump, 6×13 jump, 2×15 jump) in the 'interstitial' mechanism. This causes differences in the correlation factor and also the prefactor. Considering the fact, that the 11 jump only shows such a negligible barrier or, depending on the DFT code, no barrier at all[53] using the 'interstitial' model is the more realistic diffusion model for yttrium in bcc iron.

The diffusivity calculated by Murali[51] is virtually identical to our results using Le Claire's nine frequency model, which is not surprising considering the fact that they used the same model and calculated very similar migration barriers. Hin *et al.*[48] have calculated an activation energy that is significantly larger than our results or the results of Murali. Using the simple equation 7.4 to determine the vacancy concentration and rescale the Monte Carlo time leads an activation energy of 3.16 eV and a prefactor D_0 of $5.8 \times 10^{-6}\,\mathrm{m^2\,s^{-1}}$. This is very close to the results of Hin. Due to the high binding energy between substitutional yttrium atoms and vacancies equation 7.8 must be used instead of equation 7.4, so the good agreement may be only a coincidence.

One has to keep in mind, that the diffusivity calculated by Hin *et al.*[48] is only a byproduct of the creation of their precipitation growth model and was never intended as a way of calculating the diffusivity of yttrium. Also experimental samples have a severely damaged crystal structure full of grain boundaries, dislocations and solute atoms, therefore differences to the results based on DFT calculations, which were calculated on a perfect crystal lattice within the dilute limit should be expected. For a proper validation of the accuracy of our calculations a comparison to experimental results would be a necessary. However, to the best of our knowledge no measurements on the diffusivity of yttrium in iron have been published.

7.2 PIPE DIFFUSION

Results in this section were first published in Ref. [132].

The large binding energy of yttrium-vacancy pairs directly affects the diffusion mechanism of yttrium in bulk iron[157] and leads to a highly correlated diffusion mechanism of the yttrium-vacancy pair. The yttrium-vacancy binding energy within a dislocation is comparable to the bulk yttrium-vacancy binding energy. An yttrium atom at the most favorable position in the dislocation core (see Figure 5.4b) has a maximum binding energy of 1.19 eV to a nearest neighbor vacancy while the bulk value is 1.20 eV. This leads to the conclusion, that yttrium-vacancy pairs are as important for the pipe diffusion as they are for the bulk diffusion. The activation energy for yttrium diffusion in bulk bcc iron is governed by the expensive dissociative jumps that separate the vacancy from the yttrium atom. Due to the similar yttrium-vacancy binding energy inside of the dislocation, the same thing is expected for pipe diffusion.

CI-NEB calculations of vacancy jumps in the core of an edge dislocation were used to investigate the diffusion of yttrium. The dislocation setup was identical to the setup in Section 5.4.1. One iron atom in the dislocation core was replaced by an yttrium atom and CI-NEB calculations of dissociative vacancy jumps were performed. Due to the presence of the dislocation, the jumps can not be put in the simple categories used in Table 5.6 for the vacancy jumps in the bulk crystal, but depend on the position of the yttrium atom as well as on the initial and final position of the vacancy with respect to the dislocation. For a fixed position of the yttrium atom, all jumps of a vacancy from an atom position within 2.7 Å of the yttrium atom to a new position within 2.7 Å of the vacancy were investigated. Figure 7.7 illustrates this scheme of determining the dissociative vacancy jumps.

Figure 7.8 shows the resulting distribution of migration energies E^{mig} as a function of the yttrium-vacancy distance after the jump D_{final}. Due to the presence of the dislocation D_{final} is not limited to fixed values as it is the case in a bulk crystal, but rather spans a range of values. All of the migration energies in the dislocation core are lower than their respective equivalents in the bulk crystal if the yttrium atom is sitting in the tensile region below the inserted plane (Position B). In the case, that the yttrium atom is sitting in the inserted plane (Position A), the picture is less clear, as some migration energies are higher than in the bulk while other are lower.

Figure 7.9 helps in explaining this result. Here E^{mig} is plotted against the energy difference ΔE between the initial and final configuration. A significant number of

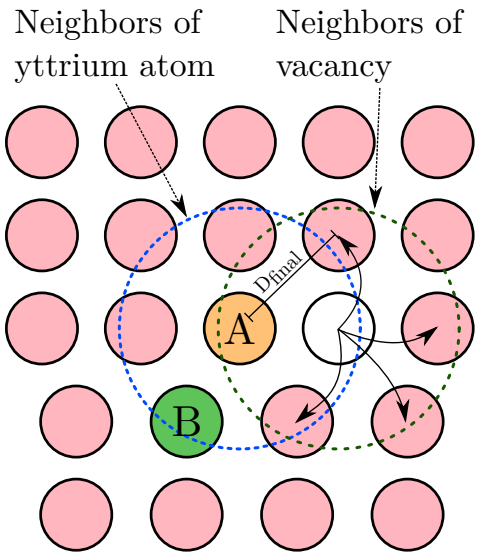

Figure 7.7: Scheme for the selection of relevant migration barriers. Nearest neighbors of the yttrium atom are starting points of vacancy jumps and nearest neighbors of these starting points are targets for the jumps. The distance between the target site and the site of the yttrium atom is called D_{final}.

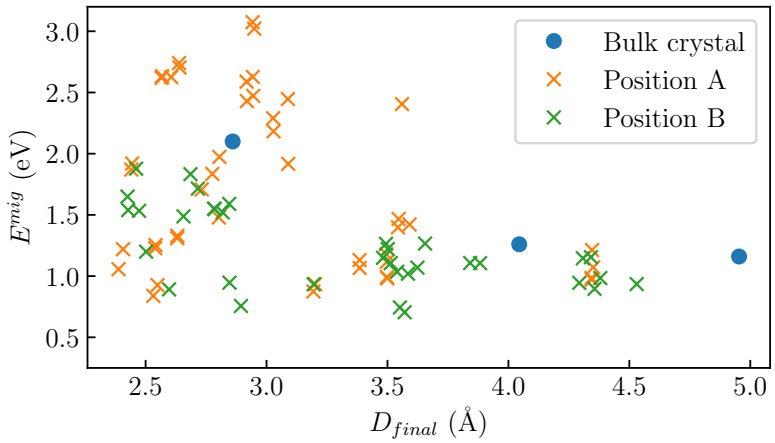

Figure 7.8: Migration barriers E^{mig} for dissociative jumps in the dislocation core plotted against D_{final}. Position A is in the inserted plane in a region under compression while Position B is directly below the inserted plane in a region under tension. As a comparison the values of E^{mig}_{12}, E^{mig}_{13} and E^{mig}_{15} in a bulk crystal are also shown.

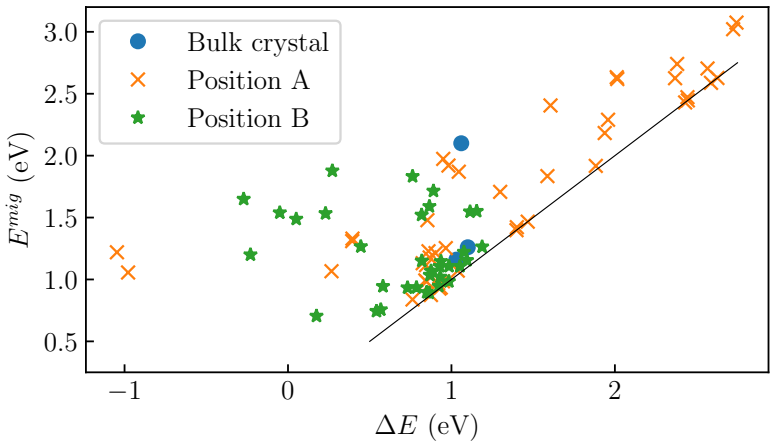

Figure 7.9: Migration barriers E^{mig} for dissociative jumps in the dislocation core plotted against the energy difference ΔE between initial and final position. Position A and position B refer to the same configurations as in Figure 7.8. The inserted black line shows the limit of the minimal migration barrier as it can not be lower than the energy difference between initial and final position.

jumps has basically no barrier additional to the energy difference. The spread in energy difference between initial and final configuration is far bigger, if the yttrium atom is sitting in position A. This is due to the fact that placing the oversized yttrium atom inside of the inserted plane leads to significant compressive strains in the system. The position of the vacancy, which is a point defect with a tensile strain field, with respect to the yttrium atom and the dislocation has a significant influence on the total energy of the configuration.

For some jumps shown in Figure 7.9 the energy difference even becomes significantly negative. This is surprising as there is an energy difference of more than 1 eV between the vacancy-yttrium atom binding energy and the subsequent binding energies. These jumps are not really dissociative jumps, as the vacancy is in a nearest-neighbor position of the yttrium atom prior as well as after the jump. In the bulk crystal such a jump would be a second-nearest neighbor exchange with a corresponding activation energy of more than 3.5 eV. Due to the presence of the dislocation these exchanges can become possible.

Figure 7.10 shows some examples of vacancy jumps with very high or very low migration barriers. In Figure 7.10a the vacancy and the yttrium atom are in the tensile region below the dislocation. The vacancy moves out of the tensile region into

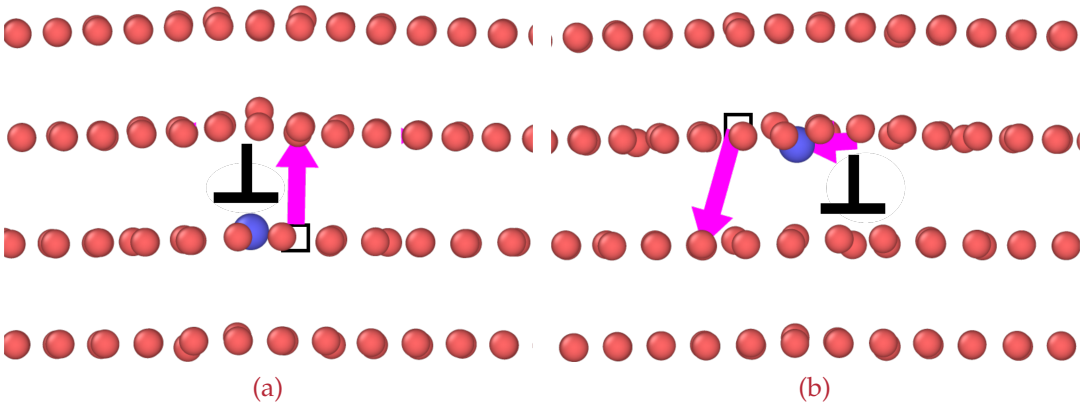

Figure 7.10: Examples of vacancy jumps with very low (a) or very high (b) migration barriers. The bcc-Fe lattice atoms are shown in red, the yttrium atom is depicted as blue and the vacancy is symbolized by a black square. In jump (a) the vacancy moves from the dilative region below the dislocation to the more favorable compressive region above the dislocation. In the jump shown in (b) the vacancy moves in the opposite direction.

the compressive region above the dislocation, which is a more favorable location for the vacancy. After the jump, the yttrium atom is in its most favorable location in the tensile region of the dislocation and the vacancy is also in its most favorable position in the compressive region above the dislocation. This results in a lowering of the migration barrier compared to the bulk case. The opposite case is shown in Figure 7.10b, where the vacancy moves from the compressive region to the tensile region while the yttrium atom is in the unfavorable compressive region. This leads to very high migration barriers. The diffusion mechanism of the yttrium diffusion will be dominated by the jumps with the lowest migration barriers.

Yttrium atoms are attracted to the tensile region of the dislocation stress field due to their size mismatch with respect to the lattice. If the yttrium atom resides in the tensile region, which is a lot more probable due to the high binding energy of up to 1.57 eV, all migration barriers of dissociative jumps are lower than their respective counterparts in the bulk. These jumps are the expensive jumps that determine the diffusion rate of the yttrium atoms. The associative jumps are cheap in the bulk crystal as well as in the vicinity of the dislocation and have no influence on the total activation energy for the diffusion. This shows, that yttrium diffusion in ODS steels will occur via pipe diffusion. Fitting of coarsening mechanisms have also

shown improved agreement to experimental data if pipe diffusion of yttrium was assumed.[49,50]

The observed reduction of the migration barriers serves only as qualitative evidence for the existence of pipe diffusion, quantitative results would require knowledge of the diffusion mechanism. Determination of the diffusion mechanism is not a trivial task, as the dislocation line is in $\langle 110 \rangle$ direction while nearest neighbor jumps are in $\langle 111 \rangle$ directions. Therefore a longer sequence of multiple vacancy jumps are necessary to move the yttrium atom along the dislocation line. This sequence could be determined by simulating the diffusion in a kinetic Monte Carlo code as it was done for bulk diffusion,[157] but would require the calculation of hundreds of migration barriers due to the symmetry breaking presence of the dislocation. Alternatively, MD calculations could be used to get quantitative results, but the duration of the simulations would be considerable due to the high activation energy. The required simulation times rules out the utilization of DFT, but classical MD using the potential developed in Chapter 5 could be possible.

7.3 CONCLUSION

The diffusivity of yttrium in bulk bcc-Fe was calculated using kinetic Monte Carlo simulations based on jump rates determined from NEB calculations and an interaction range up to the fifth neighbor shell. The activation energy for diffusion was determined to be 2.00 eV and the prefactor D_0 is $5.7 \times 10^{-7}\,\mathrm{m^2\,s^{-1}}$. It was shown, that Le Claire's nine frequency model is accurate even for diffusion processes with massively correlated jumps, but it's limitation to the second-nearest neighbor shell leads to errors in cases with a longer ranged yttrium-vacancy interaction as it is the case for yttrium in iron. The mechanism of yttrium diffusion was investigated and shown to be based on a sequence of 13-31 jumps. This allows diffusion of yttrium through the iron lattice without splitting up its bond to the vacancy using a drag mechanism.[165]

Pipe diffusion of yttrium was investigated using CI-NEB calculation of dissociative vacancy jumps inside of a dislocation. The migration barriers showed a considerable reduction in the dilative region of the elastic field of dislocations. This provides clear evidence for the existence of yttrium pipe diffusion. Quantitative results will require further MD or KMC calculations which are enabled by the potential presented in Chapter 5.

Part IV

DIFFUSION OF POINT DEFECTS

8

POINT DEFECT DIFFUSION IN STRAIN FIELDS

Results in this section are submitted to Acta Materialia.
FEM calculations in this section were carried out by Peter Stein.

Resistance to radiation damage is a crucial property for structural materials in fission or fusion reactors. The particle-matrix interface in oxide dispersion strengthened (ODS) steels is considered a sink for point defects created during irradiation. In this chapter we address the question, if elastic strain fields around oxide particles cause a long-range interaction between the precipitates and point defects. We use kinetic Monte Carlo simulations to simulate the diffusion of point defects under the influence of elastic strain fields caused by Y_2O_3 and $Y_2Ti_2O_7$ precipitates.

8.1 INTRODUCTION

The particle-matrix interfaces in ODS steels are considered as sinks for point defects created during irradiation, but their importance in comparison to other potential sinks like dislocations and grain boundaries is a matter of debate.[2–4,54] Measurements of mechanical properties show an increased resistance to radiation-induced changes for ODS steels compared to other ferritic alloys which has been attributed to the fine grain structure and high number density of oxide particles.[171] Radiation induced hardening and the corresponding creation of dislocation loops and voids have been observed in multiple studies.[56,172,173] A thorough investigation of microstructure and radiation induced hardening by Duan *et al.*[56] concluded that nanoparticles are in fact the most important sink present in ODS steels.

Due to the fabrication process via the powder processing route and the different thermal expansion coefficients of nanoparticles and matrix, there is significant internal strain within ODS steels. Thus, long-range interaction between the strain fields surrounding nanoparticles and the strain fields of point defects may significantly influence the sink strength of the particles. Gupta *et al.*[174] have shown that precipitates can influence the diffusion along grain boundaries in Al-based alloys. The elastic strain fields of dislocations can also affect precipitation formation as shown in the case of NbC in α-iron[175] and alter the sink efficiency of dislocations[64,65] as well as semicoherent interfaces.[63] This raises multiple questions that we answer

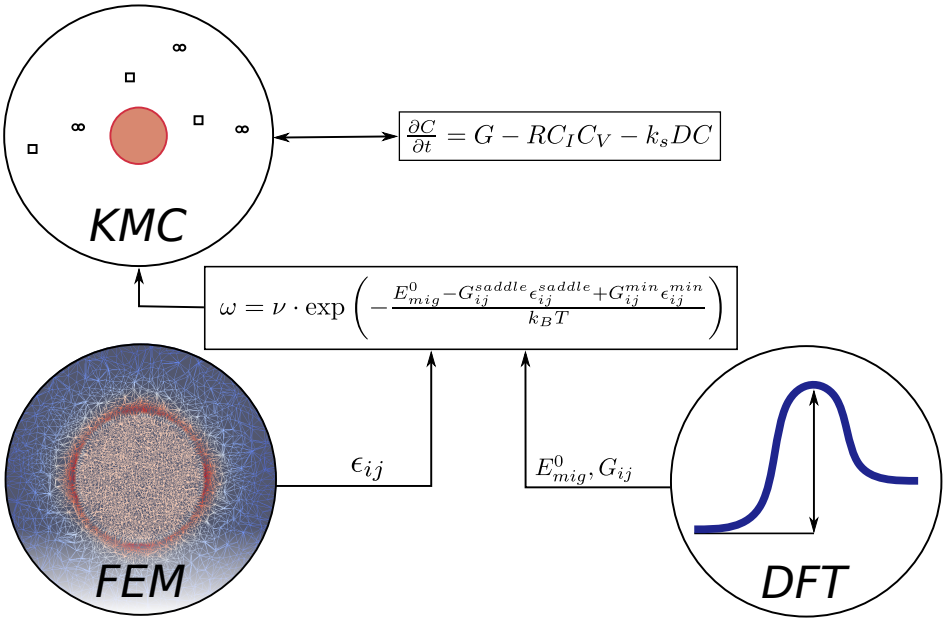

Figure 8.1: Overview of the interaction of modelling methods used in this work. Migration barriers E_{mig} and elastic dipole tensors G_{ij} at saddle point and ground state are calculated using DFT. Strain field ϵ_{ij} of the precipitates is calculated by FEM. These inputs are used in KMC simulations to investigate the diffusion of vacancies and interstitials in the strain fields of the precipitates. The results of the KMC simulations can be compared to results obtained from analytical rate theory calculations.

in this chapter: Is there a long-range interaction between precipitates and point defects in ODS steels? Does the sink strength of precipitates depend on the elastic strain field surrounding the particles and does this influence the concentration of vacancies and self-interstitial atoms (SIA) under irradiation? Does the type and shape of the precipitate influence their elastic strain field and consequently their sink strength?

In order to answer these questions, we investigated the influence of elastic strain fields on the migration of point defects using the multi-scale approach shown in Figure 8.1. Migration barriers and elastic dipole tensors were calculated by DFT and elastic strain fields around precipitates were determined with FEM calculations. These values were used as input for KMC simulations that describe the time evolution of the system.

8.2 METHODOLOGY

8.2.1 *Interaction between point defects and elastic strain*

The change in energy ΔE due to the interaction of a point defect with an elastic strain ϵ can be calculated to first order by[176]

$$\Delta E = -G_{ij}\epsilon_{ij}, \tag{8.1}$$

where G_{ij} is the elastic dipole tensor of the defect and where we employ the Einstein summation convention. The dipole tensor is a property of the defect and, in the linear elastic regime, it is independent of the externally applied strain. Different methods can be used to calculate the dipole tensor in atomistic simulations. It can be directly calculated from the stress existing in the simulation box,[177] from a fit of the atomic displacements[178] or from a summation of Kanzaki forces.[179,180] These three approaches result in the same values, if sufficiently large supercells are used, but for small simulation cells, the stress method is preferred.[177] The dipole tensor is connected to the residual stress in the simulation box by

$$G_{ij} = V(C_{ijkl}\epsilon_{kl} + \sigma_{ij}), \tag{8.2}$$

where V is the volume of the simulation cell containing the defect, C_{ijkl} is the tensor of elastic constants, ϵ_{kl} and σ_{ij} are the strain and stress tensor of the defect structure. If the cell is kept fixed between the defective and pristine supercell ($\epsilon = 0$), Equation 8.2 reduces to

$$G_{ij} = V_0\sigma_{ij}, \tag{8.3}$$

where V_0 is the volume of the simulation cell and σ_{ij} the resulting stress induced by the presence of the point defect. The elastic dipole tensor can be separated into its deviatoric and hydrostatic (isotropic) components with

$$G_{ij} = G^d_{ij} + G^h\delta_{ij}. \tag{8.4}$$

The deviatoric dipole tensor G^d_{ij} is associated with a pure shear, whereas the hydrostatic dipole tensor $G^h\delta_{ij}$ is related to a change in volume.[63] In some cases in the following sections only the hydrostatic components of the dipole tensor will be used. The defects will then be described as isotropic defects, while they will be labeled anisotropic defects if the complete dipole tensor is used. The interaction between external strain field and point defect will influence the diffusion of the point

defect by changing the migration energy. The migration energy under the influence of strain E^s_{mig} can be calculated by[181]

$$\begin{aligned} E^s_{mig} &= E^s_{saddle} - E^s_{min} && (8.5)\\ &= (E^0_{saddle} + \Delta E_{saddle}) - (E^0_{min} + \Delta E_{min}) && (8.6)\\ &= E^0_{mig} + \Delta E_{saddle} - \Delta E_{min} && (8.7)\\ &= E^0_{mig} - G^{saddle}_{ij}\epsilon^{saddle}_{ij} + G^{min}_{ij}\epsilon^{min}_{ij}, && (8.8) \end{aligned}$$

where the superscripts s and 0 denote energies affected by the strain field and energies in the pristine, strain free state. The energy of the defect at the equilibrium minimum site E^s_{min} and at the saddle point of the migration path E^s_{saddle} is changed by the presence of the strain field according to Equation 8.1. The resulting migration energy under the influence of strain can be calculated from the unstrained migration energy E^0_{mig} and the energy changes ΔE_{saddle} and ΔE_{min} according to Equation 8.8.[182]

8.2.2 *Total-energy calculations*

Elastic dipole tensors and defect migration barriers were calculated using the Vienna Ab initio Simulation Package[71–74] (VASP) using a plane wave basis set with pseudopotentials from the VASP library based on the projector augmented-wave (PAW) method[139,140] and within the generalized-gradient approximation (GGA) in the Perdew-Burke-Ernzerhof (PBE) parameterization.[70] The plane wave energy cutoff was set to 500 eV. The convergence criterion for the relaxations was achieved when all forces were less than 1 meV Å^{-1}. Point defects were introduced in a pristine, stress free crystal of bcc Fe and the atom positions were relaxed while the simulation cell was kept fixed. Supercell sizes were varied from 2x2x2 to 5x5x5 and the resulting stress was extrapolated to an infinite volume. The elastic dipole tensor was calculated from the size of the supercell and the resulting stress according to Equation 8.3. Migration barriers were determined using the climbing image nudged elastic band method.[141]

8.2.3 *Analytic strain calculation*

The elastic field of a misfitting inclusion in an infinite isotropic elastic continuum can be solved analytically using an Eshelby approach.[183] The inclusion is assumed

to be bigger than the hole in the matrix by a volume difference $\Delta v > 0$. Once the inclusion is inserted into the hole, the hole expands by the volume Δv_A. In the spherical coordinate system the resulting strain in the matrix outside of the inclusion can be calculated by:[184]

$$\varepsilon_{rr} = -\frac{\Delta v_A}{2\pi r^3}, \tag{8.9}$$

$$\varepsilon_{\theta\theta} = \varepsilon_{\phi\phi} = \frac{\Delta v_A}{4\pi r^3}, \tag{8.10}$$

$$\varepsilon_{r\phi} = \varepsilon_{r\theta} = \varepsilon_{\theta\phi} = 0. \tag{8.11}$$

The volume change of the hole Δv_A due to the insertion of the inclusion is connected to the volume difference Δv between hole and inclusion, the shear modulus of the matrix μ and the bulk modulus of the inclusion B by:

$$\Delta v = \Delta v_A \left(1 + \frac{4\mu}{3B}\right). \tag{8.12}$$

The elastic constants of Fe, Y_2O_3 and $Y_2Ti_2O_7$ are shown in Table 8.1. In addition to these experimental results, the mechanical properties of $Y_2Ti_2O_7$ have also been calculated using *ab inito* methods.[185] The analytic calculation of the strain field is based on an isotropic description of matrix and precipitate. Therefore, we calculated adjusted values of C_{44}, that result in isotropic material parameters, according to:

$$C_{44} = \frac{C_{11} - C_{12}}{2}. \tag{8.13}$$

The shear modulus $\mu = C_{44}^{iso}$ and the bulk modulus $B = C_{12} + \frac{2C_{44}^{iso}}{3}$ can be determined from the isotropic elastic constants.

8.2.4 *Strain Calculation using the Finite Element method*

In order to determine the strain fields around the precipitates in an anisotropic matrix, we resorted to static Finite Element simulations. Primary unknown is thereby the deformation of a sample's material points, given in terms of the displacement field with components u_i. The strains acting at a material point are described by the infinitesimal strain tensor

$$\varepsilon_{ij} = \frac{1}{2}\left(u_{i,j} + u_{j,i}\right), \tag{8.14}$$

Table 8.1: Elastic constants of bcc Fe[149] (Matrix), Y_2O_3 precipitate[186] and $Y_2Ti_2O_7$.[187]

Modulus (GPa)	bcc-Fe	Y_2O_3	$Y_2Ti_2O_7$
C_{11}	230	224	329
C_{12}	135	112	91
C_{44}	117	75	97
C_{44}^{iso}	47·5	56	119
B	167	149	170

where the notation $()_{,i}$ denotes a partial derivative with respect to the spatial coordinate x_i. The balance of internal and external forces in the material is governed by the equilibrium equations

$$\sigma_{ij,j} + b_i = 0, \tag{8.15}$$

where b_i denotes the body force vector resulting, for instance, from gravity, while σ_{ij} represents the components of the second-order symmetric Cauchy stress tensor,

$$\sigma_{ij} = \mathbb{C}_{ijkl} \left(\varepsilon_{kl} - \varepsilon_{kl}^0 \right). \tag{8.16}$$

The components $\mathbb{C}_{ijkl}$ thereby encode the (possibly anisotropic) elastic response of the considered material. In order to describe an elastic misfit, we prescribe the eigenstrain

$$\varepsilon_{ij}^0 = \frac{\varepsilon_V}{3} \delta_{ij} \tag{8.17}$$

within the precipitate, with δ_{ij} being the components of the symmetric second-order unit tensor and with ε_V being a dilatational strain. Within the matrix, $\varepsilon_V = 0$. Periodic boundary conditions were approximated by setting the displacements perpendicular to the border of the simulation box to zero.

These equations have been discretized by standard techniques, e.g., as in Ref.[188] and were implemented in the Finite Element software FEAP.[162] Using the resulting displacements, we computed the energy changes using the defect dipole tensor and Equation 8.1.[189]

8.2.5 *KMC simulations*

Kinetic Monte Carlo simulations were carried out using DISC,[161] a KMC model for diffusion simulations. It is based on a rigid lattice model built on a body-centered cubic lattice.[190] Elastic strain fields are included by changing the chemical potential of defects and the migration barrier as explained in Section 8.2.1. Mobile defects are vacancies and $\langle 110 \rangle$ SIA dumbbells, which are all modeled as objects on lattice sites. The lattice is a body centered cubic (bcc) lattice with a lattice constant a_0 of 2.86 Å. Spontaneous recombination of vacancies and interstitials occurs when the distance between the two defects becomes lower than the Frenkel pair radius of $d_{rec} = 2.26\,a_0$.[191] Clustering of point defects is not possible as the focus of the study was on the interaction of precipitates and isolated defects. For the same reason the irradiation is modeled more like electron irradiation than neutron radiation by creating individual interstitial-vacancy pairs at a rate of 10 dpa/s, instead of complete collision cascades. The point defects were created on random lattice sites with a separation bigger than the Frenkel pair radius.

The simulation box was a cube with an edge length of 11.44 nm and contained one precipitate with a radius of 1.28 nm. The precipitate is a perfect sink and annihilates every point defect that moves onto a site that belongs to the precipitate. When calculating the rate of jumps into the precipitate, only the strain at the starting lattice site is used, in contrast to regular jumps where both strain at lattice site and saddle point are used. Precipitates consisted of Y_2O_3 or $Y_2Ti_2O_7$ with the respective elastic constants shown in Table 8.1. The simulation temperature was set to 500 K and the migration of the point defects was simulated for 1×10^{10} steps using the residence-time algorithm.[89] The jump frequency ω was calculated by

$$\omega = \nu_0 \cdot \exp\left(-\frac{E^s_{mig}}{k_B T}\right). \tag{8.18}$$

where the attempt frequency ν is assumed to be unaffected by strain and has a value of $\nu = 6$ THz which is on the same order of magnitude as the Debye frequency of iron.[164] The migration energy E^s_{mig} depends on the strain field according to Equation 8.8. While vacancies migrate by simple nearest neighbor jumps, the mechanism looks more complicated for SIAs. The lowest-energy configuration for a SIA atom in bcc iron is the $\langle 110 \rangle$ dumbbell.[192–194] MD calculations with empirical potentials suggest a two step diffusion mechanism, where the $\langle 110 \rangle$ dumbbell rotates to a $\langle 111 \rangle$ crowdion and moves in a series of fast jumps in $\langle 111 \rangle$ direction.[195–197] This

mechanism was also observed by Gao *et al.*[198] using the dimer method, but leads to significantly lower activation energies than the 0.3 eV observed experimentally.[199]

DFT calculations predict a significantly higher energy for the ⟨111⟩ crowdion than the empirical potentials,[193,194,200] which makes the two step diffusion mechanism unfavorable. They identify nearest-neighbor translation rotation jumps as the relevant mechanism for SIA diffusion in agreement with the earliest work by Johnson *et al.*.[201] The activation energy for these translation rotation jumps is 0.34 to 0.37 eV[193,194,200] in good agreement with the 0.3 eV measured experimentally.[199] For this reason, SIA are assumed to have full 3D mobility at all temperatures in our KMC simulations, similarly to other published KMC studies.[168,202–204]

8.3 RESULTS

8.3.1 *Elastic dipole tensor and strain-free migration barriers*

DFT calculations were used to determine the migration barriers of vacancies and interstitials as well as the elastic dipole tensor at both the minimum equilibrium position and at the saddle point. The barrier for a nearest-neighbor vacancy jump in [111] direction is 0.67 eV. This result is in good agreement to the value of 0.65 eV published by Murali *et al.*[51] and the 0.69 eV of Bocquet *et al.*.[53] The dipole tensor at the ground state and the saddle point are shown in Table 8.2. The dipole tensor reflects the symmetry of the corresponding defect. Obviously the dipole tensor of the vacancy in the ground state is isotropic.

The lowest-energy configuration for a SIA atom in bcc iron is the ⟨110⟩ dumbbell.[192–194] Therefore our model is limited to this interstitial configuration. The most favorable migration mechanism for the SIA is the ⟨110⟩ - ⟨011⟩ nearest-neighbor translation-rotation jump.[201] The migration barrier of 0.33 eV is in close agreement with the results of Fu *et al.* (0.34 eV[193]) and Vincent *et al.* (0.37 eV[193]). The dipole tensor is again shown in Table 8.2. Unlike the vacancy, the dumbbell of the SIA shows off-diagonal elements even in the ground state.

8.3.2 *Strain fields around precipitates*

Strain fields were calculated analytically as shown in Section 8.2.3 and numerically by FEM calculations as introduced in Section 8.2.4. While the analytic strain fields were calculated for an isotropic matrix and precipitate, FEM calculations have been carried out for the isotropic and anisotropic case. The crystals of matrix and

Table 8.2: Elastic dipole tensor (in eV) for point defects at the ground state and at the saddle point. The vacancy saddle point is for migration in [111] direction. The interstitial is a [110] dumbbell on a [110] to [011] migration path.

Defect	Ground state	Saddle point
Vacancy	$\begin{bmatrix} -2.87 & 0 & 0 \\ 0 & -2.87 & 0 \\ 0 & 0 & -2.87 \end{bmatrix}$	$\begin{bmatrix} -2.78 & -1.31 & -1.31 \\ -1.31 & -2.78 & -1.31 \\ -1.31 & -1.31 & -2.78 \end{bmatrix}$
Interstitial	$\begin{bmatrix} 18.94 & 4.36 & 0 \\ 4.36 & 18.94 & 0 \\ 0 & 0 & 22.91 \end{bmatrix}$	$\begin{bmatrix} 21.44 & 3.07 & -0.13 \\ 3.07 & 19.64 & 3.07 \\ -0.13 & 3.07 & 21.44 \end{bmatrix}$

precipitate are coaligned in agreement to the cube-on-cube relationship observed experimentally[23,31,33–35] Figure 8.2 shows a comparison of the xx and the xy component of the resulting strain fields for Y_2O_3 and $Y_2Ti_2O_7$ precipitates with a radius of 1.43 nm and a misfit strain of 1 %. There are only minor differences between the xx, yy, and zz components of the analytic and isotropic FEM strain fields and the anisotropic FEM strain field also shows very similar values. The xy component of the analytic strain field in this direction is zero, while the FEM calculation shows some numeric artifacts caused by an insufficient FEM grid size. These fluctuations are an order of magnitude lower than the values on the diagonal of the strain tensor and cause no significant interaction with point defects. Differences between the analytical and the isotropic FEM calculations are mainly related to the difference in boundary conditions. In the FEM calculations displacements perpendicular to the border of the simulation box were set to zero, which leads to a small residual hydrostatic stress. The analytic solution on the other hand is for a defect in an infinite solid where no hydrostatic stress occurs. Strain fields scale linearly with misfit strain which allows extrapolation of FEM calculations to multiple misfit strains. Using the elastic constants of $Y_2Ti_2O_7$ instead of Y_2O_3 results in basically the same strain, as the difference of the bulk moduli shown in Table 8.1 between both crystals is not enormous.

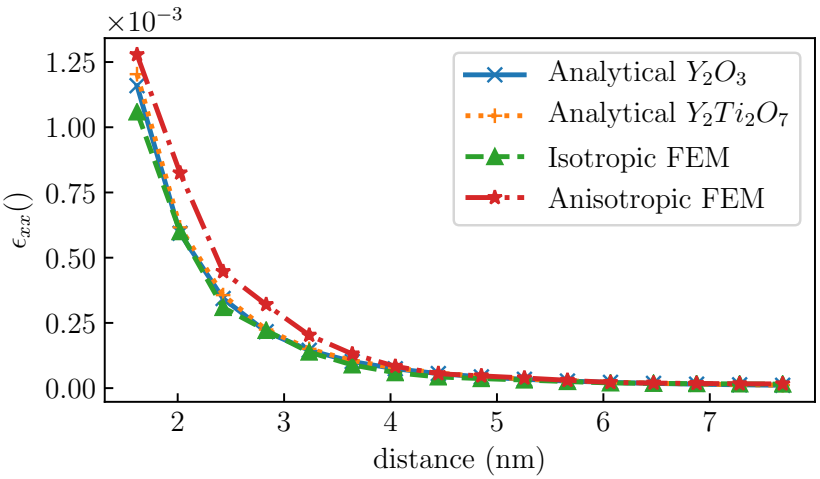

(a)

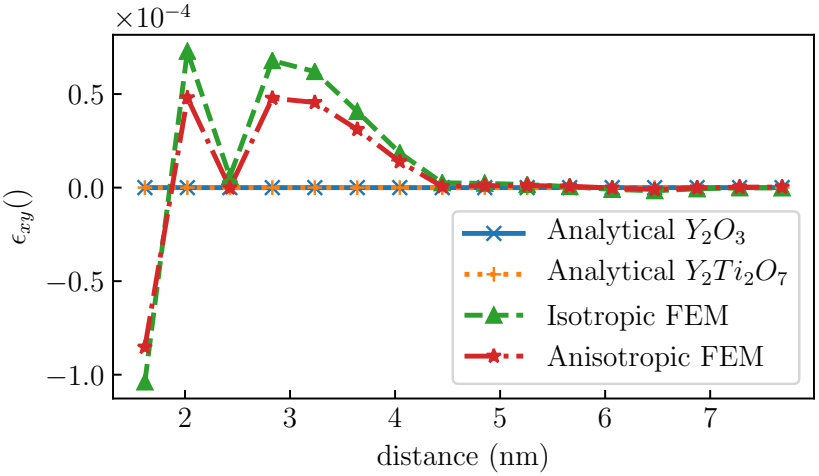

(b)

Figure 8.2: Comparison of the strain field caused by a misfitting precipitate calculated analytically and using FEM. The strain is plotted in $0\bar{1}1$ direction from the center of the precipitate. FEM calculation were done using an Y_2O_3 precipitate while analytical calculations used a Y_2O_3, as well as an $Y_2Ti_2O_7$ precipitate. The misfit strain was 1 vol% with respect to the Fe matrix.

8.3.3 *Interaction energies between point defects and precipitate strain fields*

The presence of a strain field changes the energy of a point defect at the ground state as well as at the saddle points of a jump. Figure 8.3 shows the change in energy at the equilibrium lattice sites and at the saddle points for vacancies and interstitials caused by interaction with the analytically calculated strain field. There is no interaction between vacancies in the ground state and the strain field due to the spherical symmetry of the defect and the fact that $\varepsilon_V = 0$. The saddle point energies show some change, which is caused by the off-diagonal elements of the dipole tensor. Interstitial energies at the ground state and at lattice points are changed considerably by the strain field due to the fact that the $\langle 110 \rangle$ dumbbell is not a spherically symmetric defect. These changes in ground state and saddle point energy lead to a change in migration barrier according to Equation 8.8. Therefore, external strain fields have a higher influence on the diffusion of interstitials than on vacancy diffusion.

8.3.4 *Point defect concentrations and sink stength*

The evolution of point defects under radiation was modeled using Kinetic Monte Carlo simulations. Point defects were created with a constant rate of 10 dpa/s and were mobile until they recombined with another point defect or got absorbed by the precipitate. The resulting point defect concentration in the absence of an elastic strain field as a function of time is shown in Figure 8.4. Initially, the concentration of interstitials and vacancies increases, but after some time the interstitial concentration decreases again and both concentrations reach different steady state values. The evolution of the point defect concentration can be calculated analytically by solving the following rate equations,[205,206]

$$\frac{\partial C_V}{\partial t} = G - R C_V C_I - k_s D_V C_V, \tag{8.19a}$$

$$\frac{\partial C_I}{\partial t} = G - R C_I C_V - k_s D_I C_I, \tag{8.19b}$$

where G is the irradiation flux in dpa/s and describes the point defect creation due to radiation. Interstitial-vacancy recombination is described by the second term which contains the interstitial and vacancy concentration C_V and C_I and the recombination term

$$R = 4\pi d_{rec} \frac{D_V + D_I}{V_{at}} \tag{8.20}$$

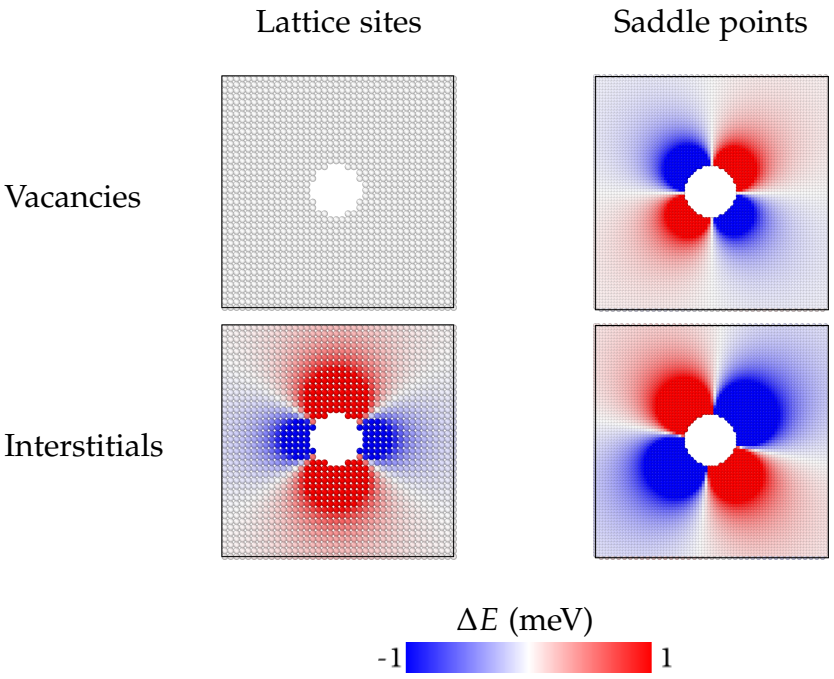

Figure 8.3: Energy change ΔE for vacancies (top row) and interstitials (bottom row) at lattice sites and at saddle points due to the strain field caused by the Y_2O_3 precipitate. The strain corresponds to a misfit strain of the precipitate of 1 %. The images show a slice through the middle of the precipitate in [100] direction.

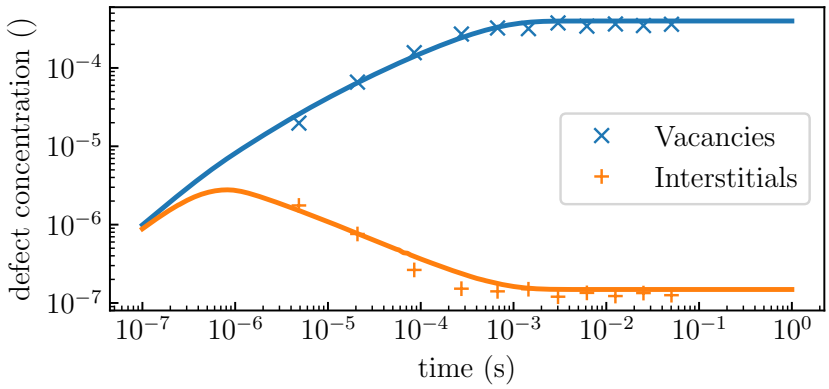

Figure 8.4: Point defect concentration under a constant irradiation of 10 dpa/s as a function of time. Markers are the result of KMC calculations while the solid lines are calculated by solving Equation 8.19.

where $d_{rec} = 2.26\,a_0$ is the Frenkel pair radius, D_V and D_I the diffusion coefficients of vacancies and interstitials and $V_{at} = a_0^3/2$ the atomic volume. The third term of Equation 8.19 describes the absorption of point defects at sinks. For spherical sinks

$$k_s = 4\pi R_s C_s, \tag{8.21}$$

where R_s is the capture radius and C_s is the concentration of sinks. The higher mobility of interstitials promotes their absorption at the precipitate-matrix interface which leads to a lower steady-state concentration. The steady state interstitial concentration is 1.30×10^{-7} and the vacancy concentration is 3.53×10^{-4}, which constitutes a difference of three orders of magnitude.

The presence of an external strain field can change the mobility of the point defects and hence the resulting steady state point defect concentrations. Figure 8.5a shows the steady-state concentration of interstitials and vacancies at different misfit strains between precipitate and matrix. The cases denoted as 'anisotropic' thereby make use of the full defect dipole tensor, whereas the cases labeled as 'isotropic' only consider the hydrostatic components as defined in Equation 8.4. The strain fields shown in Figure 8.5a have been calculated for an isotropic Y_2O_3 precipitate with a radius of 1.43 nm in an isotropic Fe matrix. There is no interaction between the strain field and defects with only a hydrostatic dipole tensor as the strain field has no dilatational components. Defects with the complete elastic dipole tensor interact with the strain field, which leads to an increase in vacancy concentration and a decline of the interstitial concentration.

There is, however, an offset between the analytical strain field and the strain field calculated from FEM calculations for the isotropic system. This is caused by a shell of lattice sites around the precipitate that experience volumetric strain when using FEM to calculate the strain field. This is a numeric artefact that is caused by the abrupt change in strain from inside of the precipitate to outside of the precipitate. By slightly increasing the radius of the precipitate to 1.36 nm while keeping the resulting strain field constant, the influence of these lattice sites can be removed which gives us Figure 8.5b. Now the analytical solution coincides with the isotropic FEM solution, which shows that the strain field in the direct neighborhood has a significant influence on the resulting defect concentrations. Additionally, the results when using an FEM-calculated strain field of an anisotropic precipitate in an anisotropic matrix are shown. As explained in Section 8.3.2, there are only minor differences between the isotropically and anisotropically calculated strain fields, which leads to basically identical point defect concentrations.

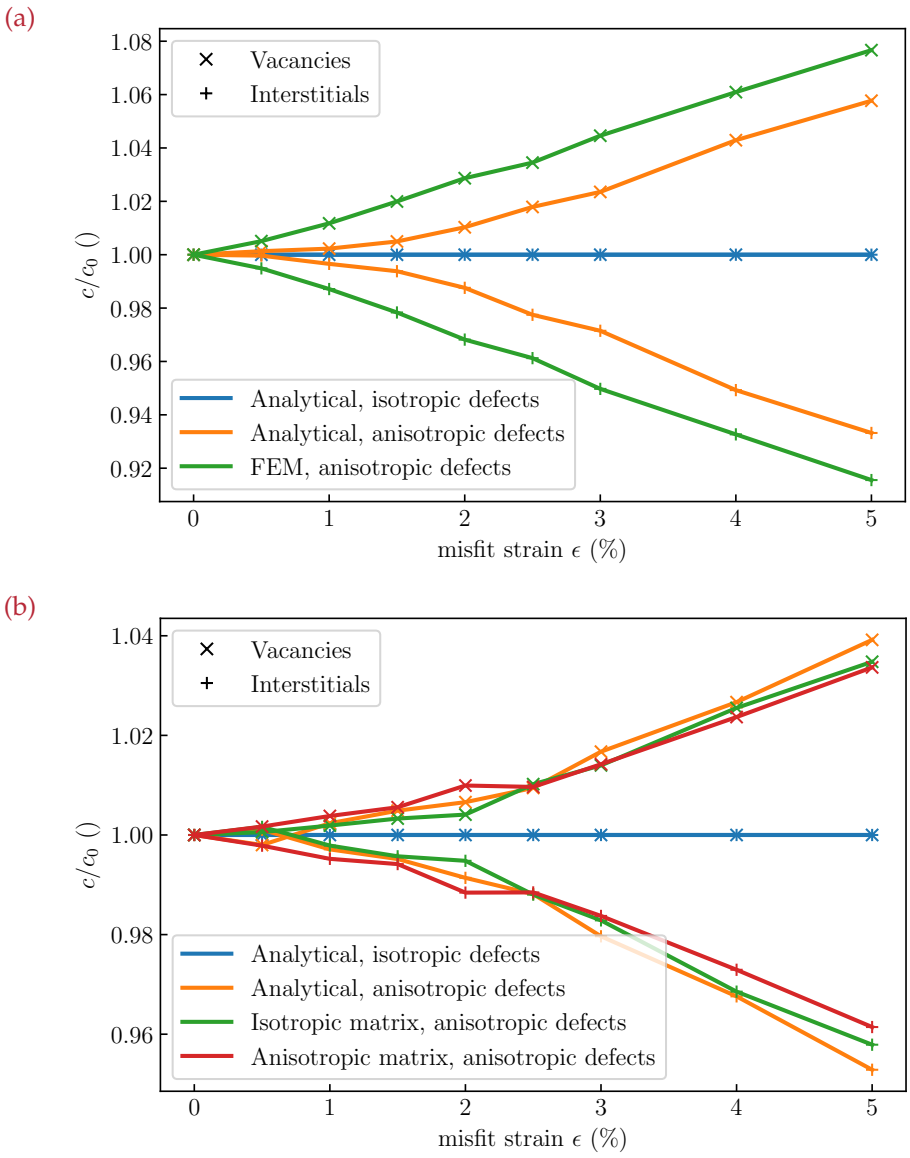

Figure 8.5: Change of interstitial and vacancy concentration with misfit strain calculated from KMC simulations with an irradiation dose of 10 dpa/s at 500 K. The radius of the precipitate is 1.28 nm in a) and has been increased to 1.36 nm in b) while keeping the resulting strain field constant. Concentrations have been normalized by the values in the absence of strain. The strain field has been calculated analytically and using FEM.

The increase of the vacancy concentration with misfit strain can be caused by two effects. Reduced absorption at precipitates due to the strain fields or an increased recombination due to the higher interstitial concentration. In order to separate these effects, KMC simulations were done using only one defect type at a time. In these cases the recombination term vanishes and the evolution equation for the average concentration simplifies to[63]

$$\frac{\partial C}{\partial t} = G - k_s D C. \tag{8.22}$$

At steady state $\frac{\partial C}{\partial t} = 0$ and the sink strength can be calculated from the resulting average concentration $\overline{C}$:

$$k_s = \frac{G}{D\overline{C}}. \tag{8.23}$$

The resulting sink strength for various misfit strains is shown in Figure 8.6. A growing misfit strain increases the sink strength for interstitials, while it only slightly influences the sink strength for vacancies. This is a counter-intuitive result as an oversized precipitate is introduced into a hole in the matrix, which, at first glance, should attract vacancies and repel interstitials. A spherical defect like an oversized precipitate, however, creates a state of pure shear in the surrounding lattice.[184] This means there is no hydrostatic pressure in the field surrounding the defect which prevents interaction with other spherical defects. This holds true for spherically symmetric defects in an infinitely large isotropic medium. However, the iron matrix is not an isotropic medium and only vacancies at the ground state have a completely spherical symmetric elastic dipole tensor. Accordingly, the influence of the strain field on vacancies is a lot weaker than on interstitials.

8.4 CONCLUSION

In this chapter we addressed the question, if strain fields cause a long-range interaction between precipitates and point defects, and thus alter the sink strength of the precipitates in ODS steels. Spherical precipitates generate a strain field of pure shear around them which only interacts with the deviatoric components of the elastic dipole tensor of point defects.[184] We have shown that this is not only true in an isotropic matrix, but that there is also effectively no interaction in the anisotropic Fe matrix. As a result, strain fields caused by the presence of precipitates have only a very limited influence on vacancies. Interstitials, on the other hand,

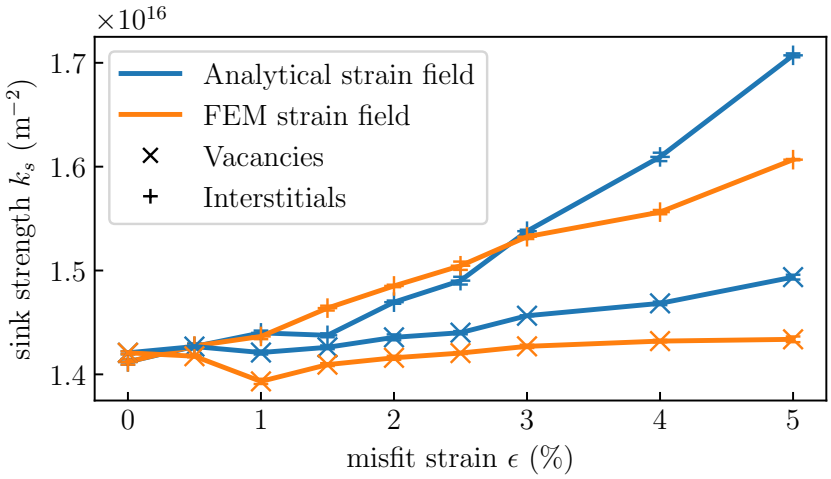

Figure 8.6: Sink strength of spherical Y_2O_3 precipitates for interstitials and vacancies as a function of misfit strain. The analytical strain field is based on an isotropic matrix while the strain field calculated by FEM is based on the anisotropic elastic constants of Fe.

form as ⟨110⟩ dumbbells and have notable deviatoric components in their elastic dipole tensors, which leads to some interaction with the elastic strain fields. This results in an increasing sink strength for interstitials with increasing misfit strain. Consequently, the interstitial concentration decreases with misfit strain and, due to reduced interstitial-vacancy recombination, the vacancy concentration increases with misfit strain. The total change of point defect concentration with misfit strain is, however, rather limited. Even at a misfit strain of 5 %, the change in defect concentration with respect to the strain free case is less than 10 %.

Due to their comparable bulk moduli, the sink strength of Y_2O_3 and $Y_2Ti_2O_7$ precipitates is essentially identical. However, what has not been considered in this work is the structure of the precipitate-matrix interface and the elastic fields created by this interface. Vattre *et al.*[63] have shown that interface elastic fields of semicoherent interfaces can have a significant influence on the sink strength of the these interfaces. A detailed investigation on the interface structure of Y_2O_3 and $Y_2Ti_2O_7$ precipitates and the resulting elastic fields would be necessary to simulate this influence, but is beyond the scope of this work. The accuracy of the KMC simulations could be further improved by the incorporation of the interaction of similar defects with each other in order to describe the formation of vacancy or interstitial

clusters.[2] Another possible improvement is in the modelling of the precipitate. At the moment, every defect that arrives at the precipitate is trapped, which corresponds to a sink efficiency of unity. Point defects caught in the precipitates might, however, be released again into the matrix,[55,207] an effect that is not considered in the current results. The loading of the precipitates with point defects might further change the elastic strain field which would lead to a changing sink strength of the precipitate. In the case of grain boundaries, the migration of point defects influences the distribution of solute atoms and can cause grain boundary segregation.[208] A similar effect could also happen with precipitates, but this work did not consider solute atoms or a coupling between the flux of solute atoms and point defects.

Part V

CONCLUSIONS

SUMMARY

In this dissertation, the diffusion of point defects in ODS steels was investigated using a multi-scale modeling approach that incorporated results of DFT, MD, KMC and FEM simulations. The key results are summarized below.

- **An interactomic potential for the Fe-Y system.** A bond-order potential has been fitted to experimental and calculated properties of pure yttrium phases, iron-yttrium mixed phases and point defects and makes large scale simulations in the Fe-Y system possible. The yttrium-yttrium parameterization of the developed potential provides an accurate description of the elastic and thermal properties of yttrium and the correct vacancy formation energy in hcp yttrium. Two different version of the iron-yttrium parameterization were created in order to provide a satisfying representation of the iron-yttrium mixed phases as well as of the yttrium point defects in iron. One shows a complete representation of the point defect energies and interactions, including migration barriers, in the bcc-Fe matrix, while the other parameterization provides an accurate representation of iron-yttrium mixed phases.

- **atomicrex, a flexible and efficient open-source code for the construction of interatomic potentials.** ATOMICREX was improved with a focus on simplifying the fitting of point defects. The concept of derived properties was added to ATOMICREX, relaxation of structures was improved and additional optimization algorithms were added.

- **Substitutional yttrium atoms cause pinning of edge dislocations.** There is a significant binding energy between substitutional yttrium atoms and the tensile stress region of the dislocation. This leads to a segregation of yttrium atoms at the dislocation and impedes the movement of the dislocation.

- **Development of Disc, a KMC code for simulating point defect diffusion with an explicit focus on performance.** Analysis of simulations is done using an easily extensible list of built-in analyzers that calculate properties like the MSD while the simulation is running. DISC also allows adding external elastic fields - either as results of FEM calculations or from analytic equations - to

KMC simulations in order to investigate the influence of these fields on point defect migration.

- **The diffusion mechanism of substitutional yttrium atoms in bulk Fe.** Migration barriers of all vacancy jumps within the fifth nearest neighbor shell of a substitutional yttrium atoms were determined using DFT CI-NEB calculations. Jump rates were calculated from these barriers and used as input values for the KMC simulations. We showed that the diffusion mechanism of yttrium is based on a sequence of vacancy jumps from the nearest neighbor position to the third nearest neighbor position and back.

- **The activation energy for yttrium diffusion in bulk Fe.** It only depends on the vacancy formation energy, the binding energy between yttrium atom and vacancy and the migration barrier when moving the vacancy from the nearest neighbor position to the third nearest neighbor position of the yttrium atom.

- **Le Claire's nine frequency model is accurate even for highly correlated events.** A comparison of the KMC based results with Le Claire's nine frequency model showed that the analytic model is accurate even for diffusion processes with massively correlated jumps, but it's limitation to the second-nearest neighbor shell leads to errors in situations with longer ranged interactions as it is the case for the yttrium-vacancy interaction in iron.

- **Reduced migration barriers in dislocation cores provide evidence for pipe diffusion of yttrium atoms.** A dipole consisting of two [111](110) edge dislocations in bcc-Fe was constructed and CI-NEB calculations of dissociative vacancy jumps inside of the dislocation core were used to determine the migration barriers. The migration barriers showed a considerable reduction in the dilative region of the elastic field of dislocations. This provides clear evidence for the existence of yttrium pipe diffusion.

- **Elastic strain fields around misfitting precipitates have only a limited influence on point defect migration.** Spherical precipitates generate a strain field of pure shear around them which only interacts with the deviatoric components of the elastic dipole tensor of point defects.[184] We have shown that this is not only true in an isotropic matrix, but that there is also effectively no interaction in the anisotropic Fe matrix. Even at a misfit strain of 5 %, the change in defect concentration with respect to the strain free case is less than 10 %.

- **The composition of the precipitate has no influence on its sink strength.** The elastic strain field created by misfitting Y_2O_3 and $Y_2Ti_2O_7$ precipitates is very similar due to their comparable bulk moduli. As a result their sink for point defects is also practically identical.

OUTLOOK

While the results presented in this thesis have answered several questions, they also opened up new ones and provide the infrastructure for follow-up research. The iron-yttrium potential developed in this thesis models only a part of the elemental interactions present in the ODS system. Extending it to include oxygen interactions would enable simulating Y_2O_3 precipitates and their interaction with dislocations or radiation. Present studies in this direction had to use severely simplified pair potentials,[91,92] that were unable to reproduce the precipitate-matrix interfaces and point-defect energies. The oxygen-oxygen interaction has already been developed for a zinc oxide potential[81] and could also be applicable to the ODS system. In an ideal case, this would limit the missing interactions to the Fe-O and the Y-O interaction.

In the context of yttrium diffusion, we have investigated the diffusion of yttrium in bulk Fe. The microstructure of ODS steels on the other hand is dominated by a high concentration of one, two and three dimensional defects which could affect the yttrium diffusion. One dimensional defects like substitutional atoms or vacancies could cluster with yttrium atoms and change the diffusion mechanism while higher dimensional defects like dislocations or grain boundaries could open up alternative, possibly faster diffusion paths. Investigating the influence of defects on the yttrium migration might help painting a more accurate picture of the yttrium diffusion which would improve our understanding of the precipitate formation process.

We have shown that migration barriers of vacancy jumps around yttrium atoms in the core of an edge dislocation are significantly lower than in bulk bcc-Fe. The diffusion mechanism of yttrium pipe diffusion and the resulting diffusion coefficient however are still unknown. Several precipitation and growth models concluded that pipe diffusion is the relevant diffusion mechanism in ODS steels, but had to use a rough approximation of the diffusion coefficient for their model.[49,50] The developed potential could allow to estimate the diffusion coefficient using long time scale MD calculations. An other options would be a coupling of molecular statics calculations and a KMC model. Migration barriers could be calculated - either on-the-fly or beforehand - based on the Fe-Y potential and be used to determine the rates of migration events in a KMC code like DISC.

Further, we have investigated the influence of strain fields around precipitate on point defect migration under irradiation. However, what has not been considered in this context is the structure of the precipitate-matrix interface and the elastic fields created by this interface. Smaller precipitates in ODS steels are often semicoherent, which can significantly change the strain fields around these precipitates.[209] Vattre *et al.*[63] have shown that interface elastic fields of semicoherent interfaces can have a significant influence on the sink strength of Cu/Ag interfaces. This raises the questions if the interface structure of Y_2O_3 and $Y_2Ti_2O_7$ precipitates in ODS steels also changes the sink strength of these precipitates.

Besides simulating the migration of vacancies and interstitials, another type of point defect that attracts considerable attention in the context of ODS steels are interstitial He atoms. They are created by transmutation reactions that result from neutron activation of atoms and can lead to significant embrittlement and swelling of the material.[10] Yang *et al.*[60,61] investigated the trapping of helium and vacancies in $Y_2Ti_2O_7$, in the Fe matrix and in the $Y_2Ti_2O_7$/Fe interface and the structure of the interface using DFT calculations, but to the best of our knowledge, no studies on the long-ranged interaction between helium and precipitates have been published.

ERKLÄRUNG – DISCLAIMER

Hiermit versichere ich an Eides statt, dass ich die vorliegende Arbeit selbstständig und nur unter Verwendung der angegebenen Hilfsmittel angefertigt habe. Diese Arbeit hat in gleicher oder ähnlicher Form noch keiner Prüfungsbehörde vorgelegen, ein Promotionsversuch wurde von mir bisher nicht unternommen.

Darmstadt, den 19. Dezember 2018

Markus Mock

DANKSAGUNG - ACKNOWLEDGMENTS

Während der Erstellung dieser Arbeit wurde ich von einer ganzen Reihe Menschen unterstützt. Als erstes möchte ich Prof. Karsten Albe für das mir entgegen gebrachte Vertrauen, seine Unterstützung und die guten Rahmenbedingungen in seiner Arbeitsgruppe danken. Desweiteren gilt mein Dank Prof. Kai Nordlund für die Begutachtung dieser Arbeit sowie Prof. Martin Heilmeier und Prof. Karsten Durst, die sich als Mitglieder meiner Prüfungskommission zur Verfügung gestellt haben.

I would like to thank Prof. Celine Hin for hosting me at Virgina Tech for three months and for the interesting discussions and insights. Also I am grateful to Prof. Kai Nordlund and Morten Nagel for the interesting discussions during my visit in Helsinki and their trip to Darmstadt.

Bei meinen Kollegen aus dem Fachgebiet Materialmodellierung möchte ich mich ganz herzlich für die angenehme Zeit und die Hilfsbereitschaft bei allen Fragen bedanken. Ein großer Dank gilt hier insbesondere unserer Sekretärin Gabi, die bei allen organisatorischen Fragen immer ein offenes Ohr hatte. Danke auch an Alex, der immer ein offenes Ohr für mich hatte und zuverlässig die Bugs in meinen Programmen gefunden hat und an Conny, die die ganze Zeit mit mir zusammen geflucht und gelacht hat. Besonderer Dank gilt auch meinen Eltern, die mich immer unterstützt und an mich geglaubt haben.

Die vorliegende Arbeit wurde finanziert von der Helmholtz Joint Research Group 411 (ODS-HiTs). Die Zusammenarbeit mit Prof. Nordlund und seiner Arbeitsgruppe wurde durch das PPP Finland Programm des Deutscher Akademischer Austauschdienst (DAAD) ermöglicht. Rechenzeit wurde gewährt von der Technische Universität Darmstadt auf dem Lichtenberg Cluster.

CURRICULUM VITAE

RESEARCH EXPERIENCE

09/2014-03/2018	**Research Associate** (Wissenschaftlicher Mitarbeiter) Materials Modelling group (Prof. Albe), Institute of Materials Science, Technische Universität Darmstadt, Germany
10/2016-12/2016	**Visiting scientist** Group of Prof. Hin, Virginia Polytechnic Institute and State University, USA

EDUCATION

10/2011-04/2014	**Master of Materials Science** Technische Universität Darmstadt, Germany
10/2008-10/2011	**Bachelor of Materials Science** Universität Stuttgart, Germany
09/1998-06/2007	**Abitur** Remstal Gymnasium Weinstadt, Germany

PUBLICATIONS RELATED TO THIS THESIS

M. Mock, P. Stein, C. Hin and K. Albe, *Modeling the influence of strain fields around precipitates on defect equilibria and kinetics under irradiation in ODS steels: A multi scale approach*, in preparation.

M. Mock and K. Albe, *Modelling of Dislocation-Solute Interaction in ODS Steels: Analytic Bond-Order Potential for the Iron-Yttrium System*, Journal of Nuclear Materials 509, pp. 102-113 (2018).

M. Mock and K. Albe, *Diffusion of Yttrium in bcc-Iron studied by Kinetic Monte Carlo Simulations*, Journal of Nuclear Materials 494, pp. 157-164 (2017).

A. Stukowski, E. Fransson, M. Mock, and P. Erhart, *Atomicrex — a general purpose tool for the construction of atomic interaction models*, Modelling and Simulation in Materials Science and Engineering 25, Nr. 5 (2017).

OTHER PUBLICATIONS

B. J. Müller, M. Mock, V. Haug, F. Hergert, T. Koehler, S. Zweigart, und U. Herr, *Ex- and in-situ investigations of sulfur diffusion into Cu(In, Ga)Se_2 thin films*, Thin Solid Films 582, pp. 284-289 (2015).

PRESENTATIONS AT INTERNATIONAL CONFERENCES

Point defect diffusion in oxide dispersion strengthened steels
Markus Mock and Karsten Albe
TMS 2017, San Diego, USA

Ordering effects and dislocation structures in high entropy alloys: A computational approach, Leonie Koch, Alexander Stukowski, Karsten Albe, Markus Mock
TMS 2017, San Diego, USA

Modelling yttrium diffusion in oxide dispersion strengthened steels
Markus Mock and Karsten Albe
ODISSEUS 2016, Dresden, Germany

Modelling yttrium diffusion in oxide dispersion strengthened steels
Markus Mock and Karsten Albe
DPG Frühjahrstagung 2016, Regensburg, Germany

BIBLIOGRAPHY

[1] Steven J. Zinkle and Jeremy T. Busby. "Structural Materials for Fission & Fusion Energy." In: *Materials Today* 12.11 (Nov. 2009), pp. 12–19. ISSN: 1369-7021. DOI: 10.1016/S1369-7021(09)70294-9.

[2] Gary S. Was. *Fundamentals of Radiation Materials Science - Metals and Alloys*. Springer Berlin Heidelberg, 2007.

[3] G.R. Odette, M.J. Alinger, and B.D. Wirth. "Recent Developments in Irradiation-Resistant Steels." In: *Annual Review of Materials Research* 38.1 (2008), pp. 471–503. DOI: 10.1146/annurev.matsci.38.060407.130315.

[4] S.j. Zinkle and L.l. Snead. "Designing Radiation Resistance in Materials for Fusion Energy." In: *Annual Review of Materials Research* 44.1 (July 2014), pp. 241–267. ISSN: 1531-7331. DOI: 10.1146/annurev-matsci-070813-113627.

[5] D. Stork, P. Agostini, J. L. Boutard, D. Buckthorpe, E. Diegele, S. L. Dudarev, C. English, G. Federici, M. R. Gilbert, S. Gonzalez, A. Ibarra, Ch Linsmeier, A. Li Puma, G. Marbach, P. F. Morris, L. W. Packer, B. Raj, M. Rieth, M. Q. Tran, D. J. Ward, and S. J. Zinkle. "Developing Structural, High-Heat Flux and Plasma Facing Materials for a near-Term DEMO Fusion Power Plant: The EU Assessment." In: *Journal of Nuclear Materials* 455.1-3 (2014). Proceedings of the 16th International Conference on Fusion Reactor Materials (ICFRM-16), pp. 277 –291. ISSN: 0022-3115. DOI: http://dx.doi.org/10.1016/j.jnucmat.2014.06.014.

[6] Shigeharu Ukai and Masayuki Fujiwara. "Perspective of ODS Alloys Application in Nuclear Environments." In: *Journal of Nuclear Materials* 307-311, Part 1.0 (2002), pp. 749 –757. ISSN: 0022-3115. DOI: http://dx.doi.org/10.1016/S0022-3115(02)01043-7.

[7] R. Lindau, A. Möslang, M. Rieth, M. Klimiankou, E. Materna-Morris, A. Alamo, A. A. F. Tavassoli, C. Cayron, A. M. Lancha, P. Fernandez, N. Baluc, R. Schäublin, E. Diegele, G. Filacchioni, J. W. Rensman, B. v. d. Schaaf, E. Lucon, and W. Dietz. "Present Development Status of EUROFER and ODS-EUROFER for Application in Blanket Concepts." In: *Fusion Engineering and Design*. Proceedings of the 23rd Symposium of Fusion TechnologySOFT 23

75–79 (Nov. 2005), pp. 989–996. ISSN: 0920-3796. DOI: 10.1016/j.fusengdes.2005.06.186.

[8] R. L. Klueh, J. P. Shingledecker, R. W. Swindeman, and D. T. Hoelzer. "Oxide Dispersion-Strengthened Steels: A Comparison of Some Commercial and Experimental Alloys." In: *Journal of Nuclear Materials* 341.2-3 (2005), pp. 103–114. ISSN: 0022-3115. DOI: doix:10.1016/j.jnucmat.2005.01.017.

[9] G.R. Odette. "Recent Progress in Developing and Qualifying Nanostructured Ferritic Alloys for Advanced Fission and Fusion Applications." English. In: *JOM* 1 (2014), pp. 1–15. ISSN: 1047-4838. DOI: 10.1007/s11837-014-1207-5.

[10] G. Robert Odette. "On the Status and Prospects for Nanostructured Ferritic Alloys for Nuclear Fission and Fusion Application with Emphasis on the Underlying Science." In: *Scripta Materialia* (2017). ISSN: 1359-6462. DOI: 10.1016/j.scriptamat.2017.06.021.

[11] Qian Zhao, Liming Yu, Yongchang Liu, and Huijun Li. "Morphology and Structure Evolution of Y2O3 Nanoparticles in ODS Steel Powders during Mechanical Alloying and Annealing." In: *Advanced Powder Technology* (2015). ISSN: 0921-8831. DOI: 10.1016/j.apt.2015.08.017.

[12] Lei Dai, Yongchang Liu, and Zhizhong Dong. "Size and Structure Evolution of Yttria in ODS Ferritic Alloy Powder during Mechanical Milling and Subsequent Annealing." In: *Powder Technology* 217.0 (2012), pp. 281 –287. ISSN: 0032-5910. DOI: http://dx.doi.org/10.1016/j.powtec.2011.10.039.

[13] Mathieu Couvrat, Laurent Chaffron, Daniel Nunes, Patrick Bonnaillie, Marie Hélène Mathon, and Mikael Perrut. "Microstructure Evolution of Mechanically Alloyed ODS Ferritic Steels during Hot Extrusion." In: *Solid State Phenomena* 172-174 (June 2011), pp. 721–726. ISSN: 1662-9779. DOI: 10.4028/www.scientific.net/SSP.172-174.721.

[14] M. Laurent-Brocq, F. Legendre, M. H. Mathon, A. Mascaro, S. Poissonnet, B. Radiguet, P. Pareige, M. Loyer, and O. Leseigneur. "Influence of Ball-Milling and Annealing Conditions on Nanocluster Characteristics in Oxide Dispersion Strengthened Steels." In: *Acta Materialia* 60.20 (Dec. 2012), pp. 7150–7159. ISSN: 1359-6454. DOI: 10.1016/j.actamat.2012.09.024.

[15] M. J. Alinger, G. R. Odette, and D. T. Hoelzer. "On the Role of Alloy Composition and Processing Parameters in Nanocluster Formation and Dispersion Strengthening in Nanostuctured Ferritic Alloys." In: *Acta Materialia* 57.2 (Jan. 2009), pp. 392–406. ISSN: 1359-6454. DOI: 10.1016/j.actamat.2008.09.025.

[16] Matthew J. Alinger. "On the Formation and Stability of Nanometer Scale Precipitates in Ferritic Alloys during Processing and High Temperature Service." In: *Ph.D. Thesis* (2004). ISSN: 9780496034932.

[17] N. Cunningham, Y. Wu, D. Klingensmith, and G. R. Odette. "On the Remarkable Thermal Stability of Nanostructured Ferritic Alloys." In: *Materials Science and Engineering: A* 613 (Sept. 2014), pp. 296–305. ISSN: 0921-5093. DOI: 10.1016/j.msea.2014.06.097.

[18] X. Boulnat, N. Sallez, M. Dade, A. Borbely, J.-L. Bechade, Y. de Carlan, J. Malaplate, Y. Brechet, F. de Geuser, A. Deschamps, P. Donnadieu, D. Fabregue, and M. Perez. "Influence of Oxide Volume Fraction on Abnormal Growth of Nanostructured Ferritic Steels during Non-Isothermal Treatments: An in Situ Study." In: *Acta Materialia* 97 (2015), pp. 124 –130. ISSN: 1359-6454. DOI: http://dx.doi.org/10.1016/j.actamat.2015.07.005.

[19] X. Boulnat, M. Perez, D. Fabrègue, S. Cazottes, and Y. de Carlan. "Characterization and Modeling of Oxides Precipitation in Ferritic Steels during Fast Non-Isothermal Consolidation." In: *Acta Materialia* 107 (Apr. 2016), pp. 390–403. ISSN: 1359-6454. DOI: 10.1016/j.actamat.2016.01.034.

[20] P. Miao, G. R. Odette, T. Yamamoto, M. Alinger, D. Hoelzer, and D. Gragg. "Effects of Consolidation Temperature, Strength and Microstructure on Fracture Toughness of Nanostructured Ferritic Alloys." In: *Journal of Nuclear Materials*. Proceedings of the Twelfth International Conference on Fusion Reactor Materials (ICFRM-12) 367-370 (Aug. 2007), pp. 208–212. ISSN: 0022-3115. DOI: 10.1016/j.jnucmat.2007.03.144.

[21] M. J. Alinger, G. R. Odette, and G. E. Lucas. "Tensile and Fracture Toughness Properties of MA957: Implications to the Development of Nanocomposited Ferritic Alloys." In: *Journal of Nuclear Materials* 307-311 (Dec. 2002), pp. 484–489. ISSN: 0022-3115. DOI: 10.1016/S0022-3115(02)01220-5.

[22] M. Klimiankou, R. Lindau, and A. Möslang. "HRTEM Study of Yttrium Oxide Particles in ODS Steels for Fusion Reactor Application." In: *Journal of Crystal Growth* 249.1–2 (Feb. 2003), pp. 381–387. ISSN: 0022-0248. DOI: 10.1016/S0022-0248(02)02134-6.

[23] M Klimiankou, R Lindau, and A Möslang. "TEM Characterization of Structure and Composition of Nanosized ODS Particles in Reduced Activation Ferritic–Martensitic Steels." In: *Journal of Nuclear Materials*. Proceedings of the 11th International Conference on Fusion Reactor Materials (ICFRM-11) 329–333, Part A (Aug. 2004), pp. 347–351. ISSN: 0022-3115. DOI: 10.1016/j.jnucmat.2004.04.083.

[24] S. Ukai, M. Harada, H. Okada, M. Inoue, S. Nomura, S. Shikakura, K. Asabe, T. Nishida, and M. Fujiwara. "Alloying Design of Oxide Dispersion Strengthened Ferritic Steel for Long Life FBRs Core Materials." In: *Journal of Nuclear Materials* 204.Supplement C (Sept. 1993), pp. 65–73. ISSN: 0022-3115. DOI: 10.1016/0022-3115(93)90200-I.

[25] M. K. Miller, E. A. Kenik, K. F. Russell, L. Heatherly, D. T. Hoelzer, and P. J. Maziasz. "Atom Probe Tomography of Nanoscale Particles in ODS Ferritic Alloys." In: *Materials Science and Engineering: A*. 47 th International Field Emission Symposium 353.1 (July 2003), pp. 140–145. ISSN: 0921-5093. DOI: 10.1016/S0921-5093(02)00680-9.

[26] Ceri A. Williams, Daniel Haley, Emmanuelle A. Marquis, George D. W. Smith, and Michael P. Moody. "Defining Clusters in APT Reconstructions of ODS Steels." In: *Ultramicroscopy*. IFES 2012 132 (Sept. 2013), pp. 271–278. ISSN: 0304-3991. DOI: 10.1016/j.ultramic.2012.12.011.

[27] A. Hirata, T. Fujita, Y. R. Wen, J. H. Schneibel, C. T. Liu, and M. W. Chen. "Atomic Structure of Nanoclusters in Oxide-Dispersion-Strengthened Steels." en. In: *Nature Materials* 10.12 (Dec. 2011), pp. 922–926. ISSN: 1476-1122. DOI: 10.1038/nmat3150.

[28] A. Hirata, T. Fujita, C. T. Liu, and M. W. Chen. "Characterization of Oxide Nanoprecipitates in an Oxide Dispersion Strengthened 14YWT Steel Using Aberration-Corrected STEM." In: *Acta Materialia* 60.16 (Sept. 2012), pp. 5686–5696. ISSN: 1359-6454. DOI: 10.1016/j.actamat.2012.06.042.

[29] M. C. Brandes, L. Kovarik, M. K. Miller, and M. J. Mills. "Morphology, Structure, and Chemistry of Nanoclusters in a Mechanically Alloyed Nanostructured Ferritic Steel." en. In: *Journal of Materials Science* 47.8 (Apr. 2012), pp. 3913–3923. ISSN: 0022-2461, 1573-4803. DOI: 10.1007/s10853-012-6249-x.

[30] S. Ukai, R. Miyata, S. Kasai, N. Oono, S. Hayashi, T. Azuma, R. Kayano, E. Maeda, and S. Ohtsuka. "Super High-Temperature Strength in Hot Rolled Steels Dispersing Nanosized Oxide Particles." In: *Materials Letters* 209.Supplement C (Dec. 2017), pp. 581–584. ISSN: 0167-577X. DOI: 10.1016/j.matlet.2017.08.101.

[31] Y. Wu, E. M. Haney, N. J. Cunningham, and G. R. Odette. "Transmission Electron Microscopy Characterization of the Nanofeatures in Nanostructured Ferritic Alloy MA957." In: *Acta Materialia* 60.8 (May 2012), pp. 3456–3468. ISSN: 1359-6454. DOI: 10.1016/j.actamat.2012.03.012.

[32] A. J. London, B. K. Panigrahi, C. C. Tang, C. Murray, and C. R. M. Grovenor. "Glancing Angle {XRD} Analysis of Particle Stability under Self-Ion Irradiation in Oxide Dispersion Strengthened Alloys." In: *Scripta Materialia* (2015), pp. –. ISSN: 1359-6462. DOI: http://dx.doi.org/10.1016/j.scriptamat.2015.07.037.

[33] Yuan Wu, Jim Ciston, Stephan Kräemer, Nathan Bailey, G. Robert Odette, and Peter Hosemann. "The Crystal Structure, Orientation Relationships and Interfaces of the Nanoscale Oxides in Nanostructured Ferritic Alloys." In: *Acta Materialia* 111 (June 2016), pp. 108–115. ISSN: 1359-6454. DOI: 10.1016/j.actamat.2016.03.031.

[34] J. Ribis and Y. de Carlan. "Interfacial Strained Structure and Orientation Relationships of the Nanosized Oxide Particles Deduced from Elasticity-Driven Morphology in Oxide Dispersion Strengthened Materials." In: *Acta Materialia* 60.1 (Jan. 2012), pp. 238–252. ISSN: 1359-6454. DOI: 10.1016/j.actamat.2011.09.042.

[35] Karl Dawson and Gordon J. Tatlock. "Characterisation of Nanosized Oxides in ODM401 Oxide Dispersion Strengthened Steel." In: *Journal of Nuclear Materials* 444.1 (Jan. 2014), pp. 252–260. ISSN: 0022-3115. DOI: 10.1016/j.jnucmat.2013.10.003.

[36] Tiberiu Stan, David J. Sprouster, Avishai Ofan, G. Robert Odette, Lynne E. Ecker, and Indrajit Charit. "X-Ray Absorption Spectroscopy Characterization of Embedded and Extracted Nano-Oxides." In: *Journal of Alloys and Compounds* 699.Supplement C (Mar. 2017), pp. 1030–1035. ISSN: 0925-8388. DOI: 10.1016/j.jallcom.2016.12.350.

[37] M. Posselt, D. Murali, and B. K. Panigrahi. "Energetics, Structure and Composition of Nanoclusters in Oxide Dispersion Strengthened Fe-Cr Alloys." In: *Modelling and Simulation in Materials Science and Engineering* 22.8 (2014), p. 085003.

[38] L. Barnard, G. R. Odette, I. Szlufarska, and D. Morgan. "An Ab Initio Study of Ti-Y-O Nanocluster Energetics in Nanostructured Ferritic Alloys." In: *Acta Materialia* 60.3 (2012), pp. 935 –947. ISSN: 1359-6454. DOI: http://dx.doi.org/10.1016/j.actamat.2011.11.011.

[39] Antoine Claisse and Pär Olsson. "First-Principles Calculations of (Y, Ti, O) Cluster Formation in Body Centred Cubic Iron-Chromium." In: *Nuclear Instruments and Methods in Physics Research Section B: Beam Interactions with Materials and Atoms* 303.0 (2013). Proceedings of the 11th Computer Simulation of Radiation Effects in Solids (COSIRES) Conference Santa Fe, New Mexico, USA, July 24-29, 2012, pp. 18 –22. ISSN: 0168-583X. DOI: http://dx.doi.org/10.1016/j.nimb.2013.01.016.

[40] Aleksejs Gopejenko, Yuri F. Zhukovskii, Pavel V. Vladimirov, Eugene A. Kotomin, and Anton Möslang. "Ab Initio Simulation of Yttrium Oxide Nanocluster Formation on Fcc Fe Lattice." en. In: *Journal of Nuclear Materials* 406.3 (Nov. 2010), pp. 345–350. ISSN: 00223115. DOI: 10.1016/j.jnucmat.2010.09.005.

[41] Aleksejs Gopejenko, Yuri F. Zhukovskii, Pavel V. Vladimirov, Eugene A. Kotomin, and Anton Möslang. "Modeling of Yttrium, Oxygen Atoms and Vacancies in γ-Iron Lattice." In: *Journal of Nuclear Materials* 416.1-2 (2011). Nuclear Materials {IV}, pp. 40 –44. ISSN: 0022-3115. DOI: http://dx.doi.org/10.1016/j.jnucmat.2010.11.088.

[42] D. Murali, B. K. Panigrahi, M. C. Valsakumar, Sharat Chandra, C. S. Sundar, and Baldev Raj. "The Role of Minor Alloying Elements on the Stability and Dispersion of Yttria Nanoclusters in Nanostructured Ferritic Alloys: An Ab Initio Study." In: *Journal of Nuclear Materials* 403.1-3 (2010), pp. 113 –116. ISSN: 0022-3115. DOI: http://dx.doi.org/10.1016/j.jnucmat.2010.06.008.

[43] Yong Jiang, John R. Smith, and G. R. Odette. "Formation of Y-Ti-O Nanoclusters in Nanostructured Ferritic Alloys: A First-Principles Study." In: *Phys. Rev. B* 79.6 (Feb. 2009), p. 064103. DOI: 10.1103/PhysRevB.79.064103.

[44] C. Hin, B. D. Wirth, and J. B. Neaton. "Formation of Y2O3 Nanoclusters in Nanostructured Ferritic Alloys during Isothermal and Anisothermal Heat Treatment: A Kinetic Monte Carlo Study." In: *Physical Review B* 80.13 (Oct. 2009), p. 134118. DOI: 10.1103/PhysRevB.80.134118.

[45] C. W. He, M. F. Barthe, P. Desgardin, S. Akhmadaliev, M. Behar, and F. Jomard. "Positron Studies of Interaction between Yttrium Atoms and Vacancies in Bcc Iron with Relevance for {ODS} Nanoparticles Formation." In: *Journal of Nuclear Materials* 455.1-3 (2014). Proceedings of the 16th International Conference on Fusion Reactor Materials (ICFRM-16)Proceedings of the 16th International Conference on Fusion Reactor Materials (ICFRM-16), Beijing, China, 20th - 26th October, 2013, pp. 398 –401. ISSN: 0022-3115. DOI: http://dx.doi.org/10.1016/j.jnucmat.2014.07.027.

[46] M. Ratti, D. Leuvrey, M. H. Mathon, and Y. de Carlan. "Influence of Titanium on Nano-Cluster (Y, Ti, O) Stability in ODS Ferritic Materials." In: *Journal of Nuclear Materials* 386 - 388.0 (2009). Fusion Reactor Materials Proceedings of the Thirteenth International Conference on Fusion Reactor Materials, pp. 540 –543. ISSN: 0022-3115. DOI: http://dx.doi.org/10.1016/j.jnucmat.2008.12.171.

[47] H. Sakasegawa, F. Legendre, L. Boulanger, M. Brocq, L. Chaffron, T. Cozzika, J. Malaplate, J. Henry, and Y. de Carlan. "Stability of Non-Stoichiometric Clusters in the MA957 ODS Ferrtic Alloy." In: *Journal of Nuclear Materials*. Proceedings of ICFRM-14 417.1–3 (Oct. 2011), pp. 229–232. ISSN: 0022-3115. DOI: 10.1016/j.jnucmat.2010.12.056.

[48] Céline Hin and Brian D. Wirth. "Formation of Y2O3 Nanoclusters in Nano-Structured Ferritic Alloys: Modeling of Precipitation Kinetics and Yield Strength." en. In: *Journal of Nuclear Materials* 402.1 (July 2010), pp. 30–37. ISSN: 00223115. DOI: 10.1016/j.jnucmat.2010.04.020.

[49] N. J. Cunningham, M. J. Alinger, D. Klingensmith, Y. Wu, and G. R. Odette. "On Nano-Oxide Coarsening Kinetics in the Nanostructured Ferritic Alloy MA957: A Mechanism Based Predictive Model." In: *Materials Science and Engineering: A* 655 (Feb. 2016), pp. 355–362. ISSN: 0921-5093. DOI: 10.1016/j.msea.2015.12.074.

[50] L. Barnard, N. Cunningham, G.R. Odette, I. Szlufarska, and D. Morgan. "Thermodynamic and Kinetic Modeling of Oxide Precipitation in Nanostructured Ferritic Alloys." en. In: *Acta Materialia* 91 (June 2015), pp. 340–354. ISSN: 13596454. DOI: 10.1016/j.actamat.2015.03.014.

[51] D. Murali, B. K. Panigrahi, M. C. Valsakumar, and C. S. Sundar. "Diffusion of Y and Ti/Zr in Bcc Iron: A First Principles Study." In: *Journal of Nuclear Materials* 419 (2011), pp. 208 –212. ISSN: 0022-3115. DOI: http://dx.doi.org/10.1016/j.jnucmat.2011.05.018.

[52] Xueyun Gao, Huiping Ren, Chunlong Li, Haiyan Wang, Yunping Ji, and Huijie Tan. "First-Principles Calculations of Rare Earth (Y, La and Ce) Diffusivities in Bcc Fe." In: *Journal of Alloys and Compounds* 663 (Apr. 2016), pp. 316–320. ISSN: 0925-8388. DOI: 10.1016/j.jallcom.2015.12.129.

[53] Jean-Louis Bocquet, Caroline Barouh, and Chu-Chun Fu. "Migration Mechanism for Oversized Solutes in Cubic Lattices: The Case of Yttrium in Iron." en. In: *Physical Review B* 95.21 (June 2017). ISSN: 2469-9950, 2469-9969. DOI: 10.1103/PhysRevB.95.214108.

[54] Graeme Ackland. "Controlling Radiation Damage." en. In: *Science* 327.5973 (Mar. 2010), pp. 1587–1588. ISSN: 0036-8075, 1095-9203. DOI: 10.1126/science.1188088.

[55] Xian-Ming Bai, Arthur F. Voter, Richard G. Hoagland, Michael Nastasi, and Blas P. Uberuaga. "Efficient Annealing of Radiation Damage Near Grain Boundaries via Interstitial Emission." en. In: *Science* 327.5973 (Mar. 2010), pp. 1631–1634. ISSN: 0036-8075, 1095-9203. DOI: 10.1126/science.1183723.

[56] Binghuang Duan, Cornelia Heintze, Frank Bergner, Andreas Ulbricht, Shavkat Akhmadaliev, Elvira Oñorbe, Yann de Carlan, and Tieshan Wang. "The Effect of the Initial Microstructure in Terms of Sink Strength on the Ion-Irradiation-Induced Hardening of ODS Alloys Studied by Nanoindentation." In: *Journal of Nuclear Materials* 495 (Nov. 2017), pp. 118–127. ISSN: 0022-3115. DOI: 10.1016/j.jnucmat.2017.08.014.

[57] A. Certain, S. Kuchibhatla, V. Shutthanandan, D. T. Hoelzer, and T. R. Allen. "Radiation Stability of Nanoclusters in Nano-Structured Oxide Dispersion Strengthened (ODS) Steels." In: *Journal of Nuclear Materials*. Special Section on Spent Nuclear Fuel 434.1–3 (Mar. 2013), pp. 311–321. ISSN: 0022-3115. DOI: 10.1016/j.jnucmat.2012.11.021.

[58] H. Ullmaier, ed. *Atomic Defects in Metals*. en. Vol. 25. Landolt-Börnstein - Group III Condensed Matter. Berlin/Heidelberg: Springer-Verlag, 1991. ISBN: 978-3-540-51435-0. DOI: 10.1007/b37800.

[59] C. M. Parish, K. A. Unocic, L. Tan, S. J. Zinkle, S. Kondo, L. L. Snead, D. T. Hoelzer, and Y. Katoh. "Helium Sequestration at Nanoparticle-Matrix Interfaces in Helium + Heavy Ion Irradiated Nanostructured Ferritic Alloys." In: *Journal of Nuclear Materials* 483.Supplement C (Jan. 2017), pp. 21–34. ISSN: 0022-3115. DOI: 10.1016/j.jnucmat.2016.10.038.

[60] Litong Yang, Yong Jiang, G. Robert Odette, Takuya Yamamoto, Zuming Liu, and Yong Liu. "Trapping Helium in Y2Ti2O7 Compared to in Matrix Iron: A First Principles Study." en. In: *Journal of Applied Physics* 115.14 (Apr. 2014), p. 143508. ISSN: 0021-8979, 1089-7550. DOI: 10.1063/1.4871282.

[61] Litong Yang, Yong Jiang, Yuan Wu, G. Robert Odette, Zhangjian Zhou, and Zheng Lu. "The Ferrite/Oxide Interface and Helium Management in Nano-Structured Ferritic Alloys from the First Principles." In: *Acta Materialia* 103 (Jan. 2016), pp. 474–482. ISSN: 1359-6454. DOI: 10.1016/j.actamat.2015.10.031.

[62] G.R. Odette and D.T. Hoelzer. "Irradiation-Tolerant Nanostructured Ferritic Alloys: Transforming Helium from a Liability to an Asset." English. In: *JOM* 62.9 (2010), pp. 84–92. ISSN: 1047-4838. DOI: 10.1007/s11837-010-0144-1.

[63] A. Vattre, T. Jourdan, H. Ding, M.-C. Marinica, and M. J. Demkowicz. "Non-Random Walk Diffusion Enhances the Sink Strength of Semicoherent Interfaces." In: *Nature Communications* 7 (Jan. 2016), p. 10424. ISSN: 2041-1723. DOI: 10.1038/ncomms10424.

[64] A. B. Sivak, V. M. Chernov, V. A. Romanov, and P. A. Sivak. "Kinetic Monte-Carlo Simulation of Self-Point Defect Diffusion in Dislocation Elastic Fields in Bcc Iron and Vanadium." In: *Journal of Nuclear Materials*. Proceedings of ICFRM-14 417.1–3 (Oct. 2011), pp. 1067–1070. ISSN: 0022-3115. DOI: 10.1016/j.jnucmat.2010.12.176.

[65] A. B. Sivak and P. A. Sivak. "Efficiency of Dislocations as Sinks of Radiation Defects in Fcc Copper Crystal." en. In: *Crystallography Reports* 59.3 (May 2014), pp. 407–414. ISSN: 1063-7745, 1562-689X. DOI: 10.1134/S1063774514030183.

[66] P. Hohenberg and W. Kohn. "Inhomogeneous Electron Gas." In: *Phys. Rev.* 136.3B (Nov. 1964), B864–B871. DOI: 10.1103/PhysRev.136.B864.

[67] W. Kohn and L. J. Sham. "Self-Consistent Equations Including Exchange and Correlation Effects." In: *Phys. Rev.* 140.4A (Nov. 1965), A1133–A1138. DOI: 10.1103/PhysRev.140.A1133.

[68] J. P. Perdew and Alex Zunger. "Self-Interaction Correction to Density-Functional Approximations for Many-Electron Systems." In: *Phys. Rev. B* 23.10 (May 1981), pp. 5048–5079. DOI: 10.1103/PhysRevB.23.5048.

[69] D. M. Ceperley and B. J. Alder. "Ground State of the Electron Gas by a Stochastic Method." In: *Phys. Rev. Lett.* 45.7 (Aug. 1980), pp. 566–569. DOI: 10.1103/PhysRevLett.45.566.

[70] John P. Perdew, Kieron Burke, and Matthias Ernzerhof. "Generalized Gradient Approximation Made Simple." In: *Phys. Rev. Lett.* 77.18 (Oct. 1996), pp. 3865–3868. DOI: 10.1103/PhysRevLett.77.3865.

[71] G. Kresse and J. Hafner. "Ab Inito Molecular Dynamics for Liquid Metals." In: *Phys. Rev. B* 47.1 (Jan. 1993), pp. 558–561. DOI: 10.1103/PhysRevB.47.558.

[72] G. Kresse and J. Furthmüller. "Efficiency of Ab Initio Total Energy Calculations for Metals and Semiconductors Using a Plane-Wave Basis Set." In: *Computational Materials Science* 6.1 (1996), pp. 15 –50. ISSN: 0927-0256. DOI: http://dx.doi.org/10.1016/0927-0256(96)00008-0.

[73] G. Kresse and J. Furthmüller. "Efficient Iterative Schemes for Ab Initio Total-Energy Calculations Using a Plane-Wave Basis Set." In: *Phys. Rev. B* 54.16 (Oct. 1996), pp. 11169–11186. DOI: 10.1103/PhysRevB.54.11169.

[74] G. Kresse and J. Hafner. "Ab Initio Molecular-Dynamics Simulation of the Liquid-Metal–Amorphous-Semiconductor Transition in Germanium." In: *Phys. Rev. B* 49.20 (May 1994), pp. 14251–14269. DOI: 10.1103/PhysRevB.49.14251.

[75] J. E. Jones. "On the Determination of Molecular Fields. —II. From the Equation of State of a Gas." en. In: *Proc. R. Soc. Lond. A* 106.738 (Oct. 1924), pp. 463–477. ISSN: 0950-1207, 2053-9150. DOI: 10.1098/rspa.1924.0082.

[76] Murray S. Daw and M. I. Baskes. "Embedded-Atom Method: Derivation and Application to Impurities, Surfaces, and Other Defects in Metals." In: *Physical Review B* 29.12 (June 1984), pp. 6443–6453. DOI: 10.1103/PhysRevB.29.6443.

[77] J. Tersoff. "New Empirical Approach for the Structure and Energy of Covalent Systems." In: *Phys. Rev. B* 37.12 (Apr. 1988), pp. 6991–7000. DOI: 10.1103/PhysRevB.37.6991.

[78] Karsten Albe, Kai Nordlund, and Robert S. Averback. "Modeling the Metal-Semiconductor Interaction: Analytical Bond-Order Potential for Platinum-Carbon." In: *Phys. Rev. B* 65.19 (May 2002), p. 195124. DOI: 10.1103/PhysRevB.65.195124.

[79] Karsten Albe, Kai Nordlund, Janne Nord, and Antti Kuronen. "Modeling of Compound Semiconductors: Analytical Bond-Order Potential for Ga, As, and GaAs." In: *Phys. Rev. B* 66.3 (July 2002), p. 035205. DOI: 10.1103/PhysRevB.66.035205.

[80] Paul Erhart and Karsten Albe. "Analytical Potential for Atomistic Simulations of Silicon, Carbon, and Silicon Carbide." In: *Phys. Rev. B* 71.3 (Jan. 2005), p. 035211. DOI: 10.1103/PhysRevB.71.035211.

[81] Paul Erhart, Niklas Juslin, Oliver Goy, Kai Nordlund, Ralf Müller, and Karsten Albe. "Analytic Bond-Order Potential for Atomistic Simulations of Zinc Oxide." In: *Journal of Physics: Condensed Matter* 18.29 (2006), p. 6585.

[82] K. O. E. Henriksson, C. Björkas, and K. Nordlund. "Atomistic Simulations of Stainless Steels: A Many-Body Potential for the Fe-Cr-C System." In: *Journal of Physics: Condensed Matter* 25.44 (2013), p. 445401.

[83] P. Allen and D.J. Tildesley. *Computer Simulation of Liquids*. Oxford science publications. Clarendon Press, 1987. ISBN: 978-0-19-855375-5.

[84] Steve Plimpton. "Fast Parallel Algorithms for Short-Range Molecular Dynamics." In: *Journal of Computational Physics* 117.1 (1995), pp. 1 –19. ISSN: 0021-9991. DOI: http://dx.doi.org/10.1006/jcph.1995.1039.

[85] Loup Verlet. "Computer "Experiments" on Classical Fluids. I. Thermodynamical Properties of Lennard-Jones Molecules." en. In: *Physical Review* 159.1 (July 1967), pp. 98–103. ISSN: 0031-899X. DOI: 10.1103/PhysRev.159.98.

[86] Shuichi Nosé. "A Unified Formulation of the Constant Temperature Molecular Dynamics Methods." In: *The Journal of Chemical Physics* 81.1 (1984), pp. 511–519. DOI: http://dx.doi.org/10.1063/1.447334.

[87] William G. Hoover. "Canonical Dynamics: Equilibrium Phase-Space Distributions." In: *Phys. Rev. A* 31.3 (Mar. 1985), pp. 1695–1697. DOI: 10.1103/PhysRevA.31.1695.

[88] M. Parrinello and A. Rahman. "Polymorphic Transitions in Single Crystals: A New Molecular Dynamics Method." In: *Journal of Applied Physics* 52.12 (1981), pp. 7182–7190. DOI: http://dx.doi.org/10.1063/1.328693.

[89] A. B. Bortz, M. H. Kalos, and J. L. Lebowitz. "A New Algorithm for Monte Carlo Simulation of Ising Spin Systems." In: *Journal of Computational Physics* 17.1 (Jan. 1975), pp. 10–18. ISSN: 0021-9991. DOI: 10.1016/0021-9991(75)90060-1.

[90] Arthur F. Voter. "Introduction to the Kinetic Monte Carlo Method." en. In: *Radiation Effects in Solids*. NATO Science Series. Springer, Dordrecht, 2007, pp. 1–23. ISBN: 978-1-4020-5293-4 978-1-4020-5295-8. DOI: 10.1007/978-1-4020-5295-8_1.

[91] Karl D. Hammond, Hyon-Jee Lee Voigt, Lauren A. Marus, Niklas Juslin, and Brian D. Wirth. "Simple Pair-Wise Interactions for Hybrid Monte Carlo Molecular Dynamics Simulations of Titania/Yttria-Doped Iron." In: *Journal of Physics: Condensed Matter* 25.5 (2013), p. 055402.

[92] K. Yashiro, A. Yamaguchi, M. Tanaka, T. Okuda, K. Koga, and T. Segi. "Molecular Dynamics Simulation on Interaction between Screw Dislocation and Pseudo Yttrium Oxide in Bcc-Fe." English. In: *Materials Transactions* 53.2 (Feb. 2012). WOS:000302194100030, pp. 401–406. ISSN: 1345-9678. DOI: 10.2320/matertrans.M2011276.

[93] G. Simonelli, R. Pasianot, and E. J. Savino. "Embedded - Atom - Method Interatomic Potentials for BCC - Iron." In: *MRS Online Proceedings Library Archive* 291 (Jan. 1992). ISSN: 1946-4274, 0272-9172. DOI: 10.1557/PROC-291-567.

[94] G. J. Ackland, D. J. Bacon, A. F. Calder, and T. Harry. "Computer Simulation of Point Defect Properties in Dilute Fe-Cu Alloy Using a Many-Body Interatomic Potential." In: *Philosophical Magazine A* 75.3 (1997), pp. 713–732. DOI: 10.1080/01418619708207198.

[95] M. I. Mendelev, S. Han, D. J. Srolovitz, G. J. Ackland, D. Y. Sun, and M. Asta. "Development of New Interatomic Potentials Appropriate for Crystalline and Liquid Iron." In: *Philosophical Magazine* 83.35 (2003), pp. 3977–3994. DOI: 10.1080/14786430310001613264.

[96] S. L. Dudarev and P. M. Derlet. "A 'magnetic' Interatomic Potential for Molecular Dynamics Simulations." en. In: *Journal of Physics: Condensed Matter* 17.44 (2005), p. 7097. ISSN: 0953-8984. DOI: 10.1088/0953-8984/17/44/003.

[97] Michael Müller, Paul Erhart, and Karsten Albe. "Analytic Bond-Order Potential for Bcc and Fcc Iron - Comparison with Established Embedded-Atom Method Potentials." In: *Journal of Physics: Condensed Matter* 19.32 (2007), p. 326220.

[98] Kai-min Fan, Li Yang, Jing Tang, Qing-qiang Sun, Yun-ya Dai, Shu-ming Peng, Xiao-song Zhou, and Xiao-tao Zu. "Analytical Bond-Order Potential for Hcp-Y." en. In: *Chinese Journal of Chemical Physics* 26.5 (Oct. 2013),

pp. 526–532. ISSN: 1674-0068, 2327-2244. DOI: 10.1063/1674-0068/26/05/526-532.

[99] M. I. Baskes and R. A. Johnson. "Modified Embedded Atom Potentials for HCP Metals." en. In: *Modelling and Simulation in Materials Science and Engineering* 2.1 (1994), p. 147. ISSN: 0965-0393. DOI: 10.1088/0965-0393/2/1/011.

[100] Wangyu Hu, Bangwei Zhang, Baiyun Huang, Fei Gao, and David J. Bacon. "Analytic Modified Embedded Atom Potentials for HCP Metals." en. In: *Journal of Physics: Condensed Matter* 13.6 (2001), p. 1193. ISSN: 0953-8984. DOI: 10.1088/0953-8984/13/6/302.

[101] Won-Seok Ko and Byeong-Joo Lee. "Modified Embedded-Atom Method Interatomic Potentials for Pure Y and the V–Pd–Y Ternary System." en. In: *Modelling and Simulation in Materials Science and Engineering* 21.8 (2013), p. 085008. ISSN: 0965-0393. DOI: 10.1088/0965-0393/21/8/085008.

[102] Alexander Stukowski, Erik Fransson, Markus Mock, and Paul Erhart. "Atomicrex—a General Purpose Tool for the Construction of Atomic Interaction Models." In: *Modelling and Simulation in Materials Science and Engineering* 25.5 (July 2017), p. 055003. ISSN: 0965-0393, 1361-651X. DOI: 10.1088/1361-651X/aa6ecf.

[103] Peter Brommer and Franz Gähler. "Potfit: Effective Potentials from *Ab Initio* Data." In: *Modelling and Simulation in Materials Science and Engineering* 15.3 (Apr. 2007), pp. 295–304. ISSN: 0965-0393, 1361-651X. DOI: 10.1088/0965-0393/15/3/008.

[104] Andres Jaramillo-Botero, Saber Naserifar, and William A. Goddard. "General Multiobjective Force Field Optimization Framework, with Application to Reactive Force Fields for Silicon Carbide." en. In: *Journal of Chemical Theory and Computation* 10.4 (Apr. 2014), pp. 1426–1439. ISSN: 1549-9618, 1549-9626. DOI: 10.1021/ct5001044.

[105] Andrew Ian Duff, M.W. Finnis, Philippe Maugis, Barend J. Thijsse, and Marcel H.F. Sluiter. "MEAMfit: A Reference-Free Modified Embedded Atom Method (RF-MEAM) Energy and Force-Fitting Code." en. In: *Computer Physics Communications* 196 (Nov. 2015), pp. 439–445. ISSN: 00104655. DOI: 10.1016/j.cpc.2015.05.016.

[106] Logan Ward, Anupriya Agrawal, Katharine M. Flores, and Wolfgang Windl. "Rapid Production of Accurate Embedded-Atom Method Potentials for Metal Alloys." In: *arXiv:1209.0619 [cond-mat, physics:physics]* (Sept. 2012). arXiv: 1209.0619 [cond-mat, physics:physics].

[107] Nongnuch Artrith and Alexander Urban. "An Implementation of Artificial Neural-Network Potentials for Atomistic Materials Simulations: Performance for TiO 2." en. In: *Computational Materials Science* 114 (Mar. 2016), pp. 135–150. ISSN: 09270256. DOI: 10.1016/j.commatsci.2015.11.047.

[108] In: (). atomistica.

[109] E. B. Tadmor, R. S. Elliott, J. P. Sethna, R. E. Miller, and C. A. Becker. "Knowledgebase of Interatomic Models (KIM)." In: (2011).

[110] E. B. Tadmor, R. S. Elliott, J. P. Sethna, R. E. Miller, and C. A. Becker. "The Potential of Atomistic Simulations and the Knowledgebase of Interatomic Models." In: *JOM* 63 (2011), p. 17.

[111] M. I. Baskes. "Application of the Embedded-Atom Method to Covalent Materials: A Semiempirical Potential for Silicon." en. In: *Physical Review Letters* 59.23 (Dec. 1987), pp. 2666–2669. ISSN: 0031-9007. DOI: 10.1103/PhysRevLett.59.2666.

[112] G. C. Abell. "Empirical Chemical Pseudopotential Theory of Molecular and Metallic Bonding." en. In: *Physical Review B* 31.10 (May 1985), pp. 6184–6196. ISSN: 0163-1829. DOI: 10.1103/PhysRevB.31.6184.

[113] J. Tersoff. "New Empirical Model for the Structural Properties of Silicon." en. In: *Physical Review Letters* 56.6 (Feb. 1986), pp. 632–635. ISSN: 0031-9007. DOI: 10.1103/PhysRevLett.56.632.

[114] Donald W. Brenner. "Empirical Potential for Hydrocarbons for Use in Simulating the Chemical Vapor Deposition of Diamond Films." en. In: *Physical Review B* 42.15 (Nov. 1990), pp. 9458–9471. ISSN: 0163-1829, 1095-3795. DOI: 10.1103/PhysRevB.42.9458.

[115] N. Juslin, P. Erhart, P. Träskelin, J. Nord, K. O. E. Henriksson, K. Nordlund, E. Salonen, and K. Albe. "Analytical Interatomic Potential for Modeling Nonequilibrium Processes in the W-C-H System." In: *Journal of Applied Physics* 98.12 (2005), pp. –. DOI: http://dx.doi.org/10.1063/1.2149492.

[116] A. Caro, D. A. Crowson, and M. Caro. "Classical Many-Body Potential for Concentrated Alloys and the Inversion of Order in Iron-Chromium Alloys." In: *Physical Review Letters* 95.7 (2005), p. 075702.

[117] A. Stukowski, B. Sadigh, P. Erhart, and A. Caro. "Efficient Implementation of the Concentration-Dependent Embedded Atom Method for Molecular Dynamics and Monte-Carlo Simulations." In: *Modelling and Simulation in Materials Science and Engineering* 17.7 (2009), p. 075005. DOI: 10.1088/0965-0393/17/7/075005.

[118] B Sadigh, P Erhart, A Stukowski, and A Caro. "Composition-Dependent Interatomic Potentials: A Systematic Approach to Modelling Multicomponent Alloys." In: *Philosophical Magazine* 89 (2009), pp. 3371–3391. DOI: 10.1080/14786430903292373.

[119] Y. Mishin, M. J. Mehl, and D. A. Papaconstantopoulos. "Phase Stability in the Fe–Ni System: Investigation by First-Principles Calculations and Atomistic Simulations." In: *Acta Materialia* 53.15 (Sept. 2005), pp. 4029–4041. ISSN: 1359-6454. DOI: 10.1016/j.actamat.2005.05.001.

[120] Frank H. Stillinger and Thomas A. Weber. "Computer Simulation of Local Order in Condensed Phases of Silicon." In: *Physical Review B* 31.8 (Apr. 1985), pp. 5262–5271. DOI: 10.1103/PhysRevB.31.5262.

[121] "MUPARSER: Fast Math Parser Library." In: ().

[122] "NLOPT: A Free/Open-Source Library for Nonlinear Optimization." In: ().

[123] "SCIPY: A Python-Based Ecosystem of Open-Source Software for Mathematics, Science, and Engineering." In: ().

[124] "SCIKIT-LEARN: Machine Learning in Python." In: ().

[125] Jörg Behler and Michele Parrinello. "Generalized Neural-Network Representation of High-Dimensional Potential-Energy Surfaces." en. In: *Physical Review Letters* 98.14 (Apr. 2007). ISSN: 0031-9007, 1079-7114. DOI: 10.1103/PhysRevLett.98.146401.

[126] Jörg Behler. "Perspective: Machine Learning Potentials for Atomistic Simulations." en. In: *The Journal of Chemical Physics* 145.17 (Nov. 2016), p. 170901. ISSN: 0021-9606, 1089-7690. DOI: 10.1063/1.4966192.

[127] Thomas J. Lenosky, Joel D. Kress, Inhee Kwon, Arthur F. Voter, Byard Edwards, David F. Richards, Sang Yang, and James B. Adams. "Highly Optimized Tight-Binding Model of Silicon." en. In: *Physical Review B* 55.3 (Jan. 1997), pp. 1528–1544. ISSN: 0163-1829, 1095-3795. DOI: 10.1103/PhysRevB.55.1528.

[128] Albert P. Bartók, Mike C. Payne, Risi Kondor, and Gábor Csányi. "Gaussian Approximation Potentials: The Accuracy of Quantum Mechanics, without the Electrons." en. In: *Physical Review Letters* 104.13 (Apr. 2010). ISSN: 0031-9007, 1079-7114. DOI: 10.1103/PhysRevLett.104.136403.

[129] "TensorFlow: An Open Source Software Library for Machine Intelligence." In: ().

[130] Søren L. Frederiksen, Karsten W. Jacobsen, Kevin S. Brown, and James P. Sethna. "Bayesian Ensemble Approach to Error Estimation of Interatomic Potentials." en. In: *Physical Review Letters* 93.16 (Oct. 2004). ISSN: 0031-9007, 1079-7114. DOI: 10.1103/PhysRevLett.93.165501.

[131] G. Csanyi, T. Albaret, M. C. Payne, and A. De Vita. ""Learn on the Fly": A Hybrid Classical and Quantum Mechanical Molecular Dynamics Simulation." In: *Physical Review Letters* 93.17 (2004), p. 175503.

[132] Markus Mock and Karsten Albe. "Modelling of Dislocation-Solute Interaction in ODS Steels: Analytic Bond-Order Potential for the Iron-Yttrium System." In: *Journal of Nuclear Materials* 509 (Oct. 2018), pp. 102–113. ISSN: 0022-3115. DOI: 10.1016/j.jnucmat.2018.06.026.

[133] Jingjie Shen, Yanfen Li, Feng Li, Huilong Yang, Zishou Zhao, Sho Kano, Yoshitaka Matsukawa, Yuhki Satoh, and Hiroaki Abe. "Microstructural Characterization and Strengthening Mechanisms of a 12Cr-ODS Steel." In: *Materials Science and Engineering: A* 673 (Sept. 2016), pp. 624–632. ISSN: 0921-5093. DOI: 10.1016/j.msea.2016.07.030.

[134] A. Chauhan, F. Bergner, A. Etienne, J. Aktaa, Y. de Carlan, C. Heintze, D. Litvinov, M. Hernandez-Mayoral, E. Oñorbe, B. Radiguet, and A. Ulbricht. "Microstructure Characterization and Strengthening Mechanisms of Oxide Dispersion Strengthened (ODS) Fe-9%Cr and Fe-14%Cr Extruded Bars." In: *Journal of Nuclear Materials* 495.Supplement C (Nov. 2017), pp. 6–19. ISSN: 0022-3115. DOI: 10.1016/j.jnucmat.2017.07.060.

[135] V. Vítek, R. C. Perrin, and D. K. Bowen. "The Core Structure of 1/2(111) Screw Dislocations in b.c.c. Crystals." en. In: *Philosophical Magazine* 21.173 (May 1970), pp. 1049–1073. ISSN: 0031-8086. DOI: 10.1080/14786437008238490.

[136] Christophe Domain and Ghiath Monnet. "Simulation of Screw Dislocation Motion in Iron by Molecular Dynamics Simulations." In: *Phys. Rev. Lett.* 95.21 (Nov. 2005), p. 215506. DOI: 10.1103/PhysRevLett.95.215506.

[137] Hideo Kaburaki, Futoshi Shimizu, Shigenobu Ogata, Masatake Yamaguchi, Takuma Kano, Hajime Kimizuka, and Mitsuhiro Itakura. "First-Principles Calculation on Core Structures and Peierls Stress of a Screw Dislocation in BCC Iron." In: *Annual Report of the Earth Simulator Center April* 2007 (2006).

[138] Derek Hull and D. J Bacon. *Introduction to Dislocations*. English. OCLC: 690385760. Oxford; Auckland (Nouvelle Zélande); Boston (Mass.): Butterworth Heinemann, 2009. ISBN: 978-0-08-052490-0.

[139] P. E. Blöchl. "Projector Augmented-Wave Method." In: *Phys. Rev. B* 50.24 (Dec. 1994), pp. 17953–17979. DOI: 10.1103/PhysRevB.50.17953.

[140] G. Kresse and D. Joubert. "From Ultrasoft Pseudopotentials to the Projector Augmented-Wave Method." In: *Phys. Rev. B* 59.3 (Jan. 1999), pp. 1758–1775. DOI: 10.1103/PhysRevB.59.1758.

[141] Graeme Henkelman, Blas P. Uberuaga, and Hannes Jónsson. "A Climbing Image Nudged Elastic Band Method for Finding Saddle Points and Minimum Energy Paths." In: *The Journal of Chemical Physics* 113.22 (Dec. 2000), pp. 9901–9904. ISSN: 0021-9606, 1089-7690. DOI: 10.1063/1.1329672.

[142] ByW. Zhang, G. Liu, and K. Han. "The Fe-Y (Iron-Yttrium) System." English. In: *Journal of Phase Equilibria* 13.3 (1992), pp. 304–308. ISSN: 1054-9714. DOI: 10.1007/BF02667560.

[143] K. P. Huber and G. Herzberg. *Molecular Spectra and Molecular Structure IV. Constants of Diatomic Molecules*. New York : Van Nostrand Reinhold, 1979.

[144] Dingguo Dai and K. Balasubramanian. "Electronic States of Yn (N=2-4)." In: *The Journal of Chemical Physics* 98.9 (1993), pp. 7098–7106. DOI: http://dx.doi.org/10.1063/1.464753.

[145] S. P. Walch and C. W. Bauschlicher. "Comparison of Ab Initio Quantum Chemistry with Experiment for Small Molecules." In: (1985).

[146] C.S. Barrett and T.B. Massalski. *Structure of Metals: Crystallographic Methods, Principles, and Data*. McGraw-Hill series in materials science and engineering. McGraw-Hill, 1966.

[147] D.R. Lide. *CRC Handbook of Chemistry and Physics, 84th Edition*. CRC HANDBOOK OF CHEMISTRY AND PHYSICS. Taylor & Francis, 2003. ISBN: 978-1-4200-7483-3.

[148] C. Kittel. *Introduction to Solid State Physics*. Wiley, 2005. ISBN: 978-0-471-49024-1.

[149] W.F. Gale and T.C. Totemeier. *Smithells Metals Reference Book*. Elsevier Science, 2003. ISBN: 978-0-08-048096-1.

[150] Frank R. de Boer, ed. *Cohesion in Metals: Transition Metal Alloys*. 2., corr. print. Cohesion and structure 1. Amsterdam: North Holland, 1988. ISBN: 978-0-444-87098-8.

[151] V. V. Ogorodnikov, A. N. Rakitskii, and Yu I. Rogovoi. "Calculation of the Vacancy Formation Energy of Metals." en. In: *Soviet Powder Metallurgy and Metal Ceramics* 27.1 (Jan. 1988), pp. 55–60. ISSN: 0038-5735, 1573-9066. DOI: 10.1007/BF00799739.

[152] R. Coehoorn. "Calculated Electronic Structure and Magnetic Properties of Y-Fe Compounds." In: *Physical Review B* 39.18 (June 1989), pp. 13072–13085. DOI: 10.1103/PhysRevB.39.13072.

[153] S. Kardellass, C. Servant, N. Selhaoui, A. Iddaoudi, M. Ait Amar, and L. Bouirden. "A Thermodynamic Assessment of the Iron–Yttrium System." In: *Journal of Alloys and Compounds* 583 (Jan. 2014), pp. 598–606. ISSN: 0925-8388. DOI: 10.1016/j.jallcom.2013.07.010.

[154] D. Murali, M. Posselt, and M. Schiwarth. "First-Principles Calculation of Defect Free Energies: General Aspects Illustrated in the Case of Bcc-Fe." In: *arxiv* (2015).

[155] D. J. Hepburn, E. MacLeod, and G. J. Ackland. "Transition Metal Solute Interactions with Point Defects in Fcc Iron from First Principles." In: *Physical Review B* 92.1 (July 2015), p. 014110. DOI: 10.1103/PhysRevB.92.014110.

[156] H. C. Herper, E. Hoffmann, and P. Entel. "Ab Initio Full-Potential Study of the Structural and Magnetic Phase Stability of Iron." In: *Physical Review B* 60.6 (Aug. 1999), pp. 3839–3848. DOI: 10.1103/PhysRevB.60.3839.

[157] Markus Mock and Karsten Albe. "Diffusion of Yttrium in Bcc-Iron Studied by Kinetic Monte Carlo Simulations." In: *Journal of Nuclear Materials* 494 (Oct. 2017), pp. 157–164. ISSN: 0022-3115. DOI: 10.1016/j.jnucmat.2017.07.021.

[158] *Asap - Atomic Simulation Environment*. https://wiki.fysik.dtu.dk/asap/asap.

[159] Ask Hjorth Larsen, Jens Jørgen Mortensen, Jakob Blomqvist, Ivano E. Castelli, Rune Christensen, Marcin Dułak, Jesper Friis, Michael N. Groves, Bjørk Hammer, Cory Hargus, Eric D. Hermes, Paul C. Jennings, Peter Bjerre Jensen, James Kermode, John R. Kitchin, Esben Leonhard Kolsbjerg, Joseph Kubal, Kristen Kaasbjerg, Steen Lysgaard, Jón Bergmann Maronsson, Tristan Maxson, Thomas Olsen, Lars Pastewka, Andrew Peterson, Carsten Rostgaard,

Jakob Schiøtz, Ole Schütt, Mikkel Strange, Kristian S. Thygesen, Tejs Vegge, Lasse Vilhelmsen, Michael Walter, Zhenhua Zeng, and Karsten W. Jacobsen. "The Atomic Simulation Environment—a Python Library for Working with Atoms." en. In: *Journal of Physics: Condensed Matter* 29.27 (2017), p. 273002. ISSN: 0953-8984. DOI: 10.1088/1361-648X/aa680e.

[160] G. Gottstein. *Physikalische Grundlagen Der Materialkunde*. Springer-Lehrbuch. Springer, 2001. ISBN: 978-3-540-41961-7.

[161] Markus Mock. *Disc - the Diffusion Simulation Code*. https://gitlab.com/mmock/disc. June 2017.

[162] *FEAP*. http://projects.ce.berkeley.edu/feap/.

[163] Donald JR Meagher. *Octree Encoding: A New Technique for the Representation, Manipulation and Display of Arbitrary 3-d Objects by Computer*. Electrical and Systems Engineering Department Rensseiaer Polytechnic Institute Image Processing Laboratory, 1980.

[164] Luca Messina, Maylise Nastar, Thomas Garnier, Christophe Domain, and Pär Olsson. "Exact Ab Initio Transport Coefficients in Bcc Fe-X Dilute Alloys." In: *Physical Review B* 90.10 (Sept. 2014), p. 104203. DOI: 10.1103/PhysRevB.90.104203.

[165] Thomas Garnier, Maylise Nastar, Pascal Bellon, and Dallas R. Trinkle. "Solute Drag by Vacancies in Body-Centered Cubic Alloys." en. In: *Phys. Rev. B* 88.13 (Oct. 2013), p. 134201. ISSN: 1098-0121, 1550-235X. DOI: 10.1103/PhysRevB.88.134201.

[166] Wilhelm Jost. *Solid State*. Physical chemistry, an advanced treatise, v. 10. New York: Academic Press, 1970. ISBN: 978-0-12-245610-7.

[167] J. Philibert. *Atom Movements: Diffusion and Mass Transport in Solids*. eng. Monographies de physique. Les Ulis, France: Editions de Physique, 1991. ISBN: 978-2-86883-161-3.

[168] J. Marian, B. D. Wirth, G. R. Odette, and J. M. Perlado. "Cu Diffusion in α-Fe: Determination of Solute Diffusivities Using Atomic-Scale Simulations." In: *Computational Materials Science* 31.3–4 (Nov. 2004), pp. 347–367. ISSN: 0927-0256. DOI: 10.1016/j.commatsci.2004.03.023.

[169] Frederic Soisson and Chu-Chun Fu. "Cu-Precipitation Kinetics in α-Fe from Atomistic Simulations: Vacancy-Trapping Effects and Cu-Cluster Mobility." en. In: *Physical Review B* 76.21 (Dec. 2007). ISSN: 1098-0121, 1550-235X. DOI: 10.1103/PhysRevB.76.214102.

[170] WM Lomer. "Vacancies and Other Point Defects in Metals and Alloys." In: *Institute of Metals, London* 79 (1958).

[171] D. A. McClintock, M. A. Sokolov, D. T. Hoelzer, and R. K. Nanstad. "Mechanical Properties of Irradiated ODS-EUROFER and Nanocluster Strengthened 14YWT." In: *Journal of Nuclear Materials*. Nuclear Fuels and Structural Materials 2Proceedings of the Second Symposium on Nuclear Fuels and Structural Materials for Next Generation Nuclear Reactors 392.2 (July 2009), pp. 353–359. ISSN: 0022-3115. DOI: 10.1016/j.jnucmat.2009.03.024.

[172] C. Heintze, F. Bergner, M. Hernández-Mayoral, R. Kögler, G. Müller, and A. Ulbricht. "Irradiation Hardening of Fe–9Cr-Based Alloys and ODS Eurofer: Effect of Helium Implantation and Iron-Ion Irradiation at 300 °C Including Sequence Effects." In: *Journal of Nuclear Materials* 470 (Mar. 2016), pp. 258–267. ISSN: 0022-3115. DOI: 10.1016/j.jnucmat.2015.12.041.

[173] M. J. Swenson and J. P. Wharry. "TEM Characterization of Irradiated Microstructure of Fe-9%Cr ODS and Ferritic-Martensitic Alloys." In: *Journal of Nuclear Materials* 502 (Apr. 2018), pp. 30–41. ISSN: 0022-3115. DOI: 10.1016/j.jnucmat.2018.01.062.

[174] Ankit Gupta, Vladislav Kulitcki, Bengü Tas Kavakbasi, Yulia Buranova, Jörg Neugebauer, Gerhard Wilde, Tilmann Hickel, and Sergiy V. Divinski. "Precipitate-Induced Nonlinearities of Diffusion along Grain Boundaries in Al-Based Alloys." en. In: *Physical Review Materials* 2.7 (July 2018). ISSN: 2475-9953. DOI: 10.1103/PhysRevMaterials.2.073801.

[175] C. Hin, Y. Bréchet, P. Maugis, and F. Soisson. "Kinetics of Heterogeneous Dislocation Precipitation of NbC in Alpha-Iron." In: *Acta Materialia* 56.19 (Nov. 2008), pp. 5535–5543. ISSN: 1359-6454. DOI: 10.1016/j.actamat.2008.07.044.

[176] G. Leibfried and N. Breuer. *Point Defects in Metals I: Introduction to the Theory*. en. Springer Tracts in Modern Physics. Berlin Heidelberg: Springer-Verlag, 1978. ISBN: 978-3-662-15448-9.

[177] Emmanuel Clouet, Céline Varvenne, and Thomas Jourdan. "Elastic Modeling of Point-Defects and Their Interaction." In: *Computational Materials Science* 147 (May 2018), pp. 49–63. ISSN: 0927-0256. DOI: 10.1016/j.commatsci.2018.01.053.

[178] Zhengzheng Chen, Nicholas Kioussis, Nasr Ghoniem, and Dariush Seif. "Strain-Field Effects on the Formation and Migration Energies of Self Interstitials in $\ensuremath{\alpha}\text{-Fe}$ from First Principles." In: *Physical Review B* 81.9 (Mar. 2010), p. 094102. DOI: 10.1103/PhysRevB.81.094102.

[179] H. Kanzaki. "Point Defects in Face-Centred Cubic Lattice—I Distortion around Defects." In: *Journal of Physics and Chemistry of Solids* 2.1 (Mar. 1957), pp. 24–36. ISSN: 0022-3697. DOI: 10.1016/0022-3697(57)90003-3.

[180] J. R. Hardy and A. B. Lidiard. "The Displacements and Polarization Caused by Point Defects in Ionic Crystals." In: *Philosophical Magazine* 15.136 (Apr. 1967), pp. 825–843. ISSN: 0031-8086. DOI: 10.1080/14786436708220930.

[181] Ashkan Moradabadi, Payam Kaghazchi, Jochen Rohrer, and Karsten Albe. "Influence of Elastic Strain on the Thermodynamics and Kinetics of Lithium Vacancy in Bulk ${\mathrm{LiCoO}}_{2}$." In: *Physical Review Materials* 2.1 (Jan. 2018), p. 015402. DOI: 10.1103/PhysRevMaterials.2.015402.

[182] Gopinath Subramanian, Danny Perez, Blas P. Uberuaga, Carlos N. Tomé, and Arthur F. Voter. "Method to Account for Arbitrary Strains in Kinetic Monte Carlo Simulations." In: *Physical Review B* 87.14 (Apr. 2013), p. 144107. DOI: 10.1103/PhysRevB.87.144107.

[183] John Douglas Eshelby. "The Determination of the Elastic Field of an Ellipsoidal Inclusion, and Related Problems." en. In: *Proc. R. Soc. Lond. A* 241.1226 (Aug. 1957), pp. 376–396. ISSN: 0080-4630, 2053-9169. DOI: 10.1098/rspa.1957.0133.

[184] W. Cai and W.D. Nix. *Imperfections in Crystalline Solids*. Cambridge University Press, 2016. ISBN: 978-1-316-38950-8.

[185] T. Danielson, E. Tea, and C. Hin. "Ab Initio Investigation of Helium in Y2Ti2O7: Mobility and Effects on Mechanical Properties." In: *Journal of Nuclear Materials* 477 (Aug. 2016), pp. 215–221. ISSN: 0022-3115. DOI: 10.1016/j.jnucmat.2016.05.024.

[186] James W. Palko, Waltraud M. Kriven, Stanislav V. Sinogeikin, Jay D. Bass, and Ali Sayir. "Elastic Constants of Yttria (Y_2O_3) Monocrystals to High Temperatures." In: *Journal of Applied Physics* 89.12 (June 2001), pp. 7791–7796. ISSN: 0021-8979. DOI: 10.1063/1.1369395.

[187] Yanbing Luan. "Elastic Properties of Complex Transition Metal Oxides Studied by Resonant Ultrasound Spectroscopy." In: *Doctoral Dissertations* (May 2011).

[188] Thomas JR Hughes. *The Finite Element Method: Linear Static and Dynamic Finite Element Analysis*. Courier Corporation, 2012.

[189] Peter Stein, Ashkan Moradabadi, Manuel Diehm, Bai-Xiang Xu, and Karsten Albe. "The Influence of Anisotropic Surface Stresses and Bulk Stresses on Defect Thermodynamics in LiCoO2 Nanoparticles." In: *Acta Materialia* 159 (Oct. 2018), pp. 225–240. ISSN: 1359-6454. DOI: 10.1016/j.actamat.2018.07.046.

[190] Pascal Bellon and G. Martin. *Lattice Kinetic Descriptions for Bulk Reaction-Diffusion Processes: Application to Alloys under Irradiation*. en. https://www.scientific.net/M 156.209. 1994. DOI: 10.4028/www.scientific.net/MSF.155-156.209.

[191] Kenichi Nakashima, Roger E Stoller, and Haixuan Xu. "Recombination Radius of a Frenkel Pair and Capture Radius of a Self-Interstitial Atom by Vacancy Clusters in Bcc Fe." In: *Journal of Physics: Condensed Matter* 27.33 (Aug. 2015), p. 335401. ISSN: 0953-8984, 1361-648X. DOI: 10.1088/0953-8984/27/33/335401.

[192] W. Schilling. "Self-Interstitial Atoms in Metals." In: *Journal of Nuclear Materials* 69-70 (Feb. 1978), pp. 465–489. ISSN: 0022-3115. DOI: 10.1016/0022-3115(78)90261-1.

[193] Chu-Chun Fu, F. Willaime, and P. Ordejón. "Stability and Mobility of Mono- and Di-Interstitials in $\ensuremath{\alpha}$-Fe." In: *Physical Review Letters* 92.17 (Apr. 2004), p. 175503. DOI: 10.1103/PhysRevLett.92.175503.

[194] E. Vincent, C. S. Becquart, and C. Domain. "Ab Initio Calculations of Self-Interstitial Interaction and Migration with Solute Atoms in Bcc Fe." In: *Journal of Nuclear Materials* 359.3 (Dec. 2006), pp. 227–237. ISSN: 0022-3115. DOI: 10.1016/j.jnucmat.2006.08.022.

[195] B. D. Wirth, G. R. Odette, D. Maroudas, and G. E. Lucas. "Energetics of Formation and Migration of Self-Interstitials and Self-Interstitial Clusters in α-Iron." In: *Journal of Nuclear Materials*. Radiation Materials Science in Technology Applications 244.3 (Apr. 1997), pp. 185–194. ISSN: 0022-3115. DOI: 10.1016/S0022-3115(96)00736-2.

[196] R.C Pasianot, A.M Monti, G Simonelli, and E.J Savino. "Computer Simulation of SIA Migration in Bcc and Hcp Metals." en. In: *Journal of Nuclear Materials* 276.1-3 (Jan. 2000), pp. 230–234. ISSN: 00223115. DOI: 10.1016/S0022-3115(99)00182-8.

[197] Yu.N. Osetsky. "Atomistic Study of Diffusional Mass Transport in Metals." en. In: *Defect and Diffusion Forum* 188-190 (Jan. 2001), pp. 71–92. ISSN: 1662-9507. DOI: 10.4028/www.scientific.net/DDF.188-190.71.

[198] Fei Gao, Graeme Henkelman, William J. Weber, L. Rene Corrales, and Hannes Jónsson. "Finding Possible Transition States of Defects in Silicon-Carbide and Alpha-Iron Using the Dimer Method." In: *Nuclear Instruments and Methods in Physics Research Section B: Beam Interactions with Materials and Atoms*. 6th International Conference on Computer Simulation of Radiation Effects in Solids 202 (Apr. 2003), pp. 1–7. ISSN: 0168-583X. DOI: 10.1016/S0168-583X(02)01822-0.

[199] S. Takaki, J. Fuss, H. Kugler, U. Dedek, and H. Schultz. "Resistivity Recovery of High Purity and Carbon Doped Iron Following Low Temperature Electron Irradiation." In: *Radiation effects* 79.1-4 (1983), pp. 87–122. DOI: 10.1080/00337578308207398.

[200] P. Olsson. "Ab Initio Study of Interstitial Migration in Fe–Cr Alloys." In: *Journal of Nuclear Materials*. Fusion Reactor MaterialsProceedings of the Thirteenth International Conference on Fusion Reactor Materials 386–388 (Apr. 2009), pp. 86–89. ISSN: 0022-3115. DOI: 10.1016/j.jnucmat.2008.12.065.

[201] R. A. Johnson. "Interstitials and Vacancies in α Iron." In: *Physical Review* 134.5A (1964), A1329.

[202] N. Soneda and T. Diaz de la Rubia. "Defect Production, Annealing Kinetics and Damage Evolution in α-Fe: An Atomic-Scale Computer Simulation." en. In: *Philosophical Magazine A* 78.5 (Nov. 1998), pp. 995–1019. ISSN: 0141-8610, 1460-6992. DOI: 10.1080/01418619808239970.

[203] N. Soneda, S. Ishino, A. Takahashi, and K. Dohi. "Modeling the Microstructural Evolution in Bcc-Fe during Irradiation Using Kinetic Monte Carlo Computer Simulation." In: *Journal of Nuclear Materials*. Proceedings of the Second IEA Fusion Materials Agreement Workshop on Modeling and Experimental Validation 323.2 (Dec. 2003), pp. 169–180. ISSN: 0022-3115. DOI: 10.1016/j.jnucmat.2003.08.021.

[204] C. Domain, C.S. Becquart, and L. Malerba. "Simulation of Radiation Damage in Fe Alloys: An Object Kinetic Monte Carlo Approach." en. In: *Journal of Nuclear Materials* 335.1 (Oct. 2004), pp. 121–145. ISSN: 00223115. DOI: 10.1016/j.jnucmat.2004.07.037.

[205] Frédéric Soisson. "Kinetic Monte Carlo Simulations of Radiation Induced Segregation and Precipitation." en. In: *Journal of Nuclear Materials* 349.3 (Mar. 2006), pp. 235–250. ISSN: 00223115. DOI: 10.1016/j.jnucmat.2005.11.003.

[206] F. A. Nichols. "On the Estimation of Sink-Absorption Terms in Reaction-Rate-Theory Analysis of Radiation Damage." In: *Journal of Nuclear Materials* 75.1 (July 1978), pp. 32–41. ISSN: 0022-3115. DOI: 10.1016/0022-3115(78)90026-0.

[207] I. J. Beyerlein, M. J. Demkowicz, A. Misra, and B. P. Uberuaga. "Defect-Interface Interactions." In: *Progress in Materials Science* 74.Supplement C (Oct. 2015), pp. 125–210. ISSN: 0079-6425. DOI: 10.1016/j.pmatsci.2015.02.001.

[208] Chris Nellis and Céline Hin. "Radiation Induced Segregation in Quaternary Fe-Ti-Y-O Alloys." In: *Journal of Alloys and Compounds* 701 (Apr. 2017), pp. 82–93. ISSN: 0925-8388. DOI: 10.1016/j.jallcom.2017.01.017.

[209] Liang Liang Song, Shaojun Liu, and Xiaodong Mao. "A New Method for Fast Statistical Measurement of Interfacial Misfit Strain around Nano-Scale Semi-Coherent Particles." en. In: *RSC Advances* 7.45 (2017), pp. 28506–28512. DOI: 10.1039/C7RA05079H.